Cnoidal and Sinusoidal Wave Reflection from a Laboratory Sand Beach

A Thesis

Submitted to the Faculty

of

Drexel University

by

Mehmet Ali Hinis

in partial fulfillment of the

requirements for the degree

of

Doctor of Philosophy

February 2003

Dedications

To my Father and Mother, without them, I would not be.

To my family; Melek and Elif Berru, without their love and patience, this research would not be finished.

Acknowledgments

I have many people to tank to. First, my special thanks go to Dr. J.R. Weggel, my advisor, for introducing the world of coastal engineering and waves to me. Without his endless patience and knowledge and answers to my everlasting questions, this research would not be complete.

Thank you Dr. J.P. Martin, a problem solving mind, with your support and encouragements throughout this research.

Dr. R.M. Sorensen, Dr. J. Feir, and Dr. M. Piasecki, Dr. J. Cheng for kindly serving on my Ph.D. committee. I appreciate the time and helpful suggestions given to my investigation.

I thank Dr. R. M. Koerner who supplied geotextiles used in this study and Dr. R. Carr for his help and discussions in designing the wave gages. Dr. M.S. Khan: his friendship and efforts in the laboratory parts of this research.

I greatly appreciate the Ministry of National Education of Republic of Turkey and Civil and Architectural Engineering Department of Drexel University for financial supports.

Table of Contents

List of Tables

List of Figures

Abstract

Cnoidal and Sinusoidal Wave Reflection from a Laboratory Sand Beach
Mehmet Ali Hinis
J.R. Weggel, Ph.D.

This study focuses on the evolution of accretional beach profiles under cnoidal and sinusoidal waves and on the reflection of those waves from the sand beach. The SUPERTANK test, STi0, conducted at Oregon State University in 1991 was reproduced at three different scales, 1:10, 1:8.5 and 1:11. Two tests were run at each scale by using sinusoidal and cnoidal waves. The results are compared and differences discussed for: energy spectra, reflection coefficients, phase angles between incident and reflected waves, reflection points and calculated bottom velocities. Beach profiles evolved differently under sinusoidal and cnoidal waves. Sinusoidal waves changed the beach profile part by part sequentially. Changes were first observed nearshore as berm building. After the berm was established, the offshore profile changed. Offshore bars grew under the sinusoidal waves. Cnoidal waves affected the whole profile and changes were observed over the entire "body of the beach" simultaneously. Changes were similar at the beginning of the profile for both kinds of waves, however. The initial profile for all tests was a barred profile. Sinusoidal and cnoidal waves both flattened the beach profile by removing the initial bar.

The variation in reflection coefficient with time during the evolution of the beach profile shows that equilibrium was attained differently for the two types of waves. The reflection coefficient reached a constant value when the berm face slopes was established. The berm slope developed early in the sinusoidal tests but developed later in the cnoidal tests.

Reflected wave spectra showed an energy shift between the fundamental and the first harmonic for both sinusoidal and cnoidal waves. This energy shift from the fundamental to the first harmonic was more pronounced in cnoidal waves, causing deeper bar-troughs on the beach profile. Frequency shifting is observed as beach profile changes. As profile changes, multiple harmonics are affected. First harmonic increases as berm crest builds up. After beach face slope is established, fundamental frequency is observed being sensitive to the slope changes.

CHAPTER 1. INTRODUCTION

This dissertation describes the rationale, methodology, findings and conclusions of a laboratory sand beach study under sinusoidal and cnoidal waves. Cnoidal waves are recognized to be a more realistic representation of waves as they approach shore. However, cnoidal waves have not been used routinely for this type of study. Experiments were done with both cnoidal and sinusoidal waves to improve understanding of beach accretion processes. Cnoidal waves were used to "calibrate" results to the work of others who used monochromatic waves. A 96 ft. long wave tank with a sand beach was used. The tank was equipped with a computer-controlled wave generator. The sand was 0.22 mm diameter, in the middle of the typical range of North Atlantic beaches. Focus was on the process of beach accretion by the onshore movement of an offshore bar. Waveforms (including reflections) and the pattern and time frame for the sand profile to evolve to equilibrium were measured.

The evolution of beach profiles by wave action is of fundamental interest to coastal engineers. It is difficult to study quantitatively, in part due to the complexity of the waves themselves. Studies, primarily of eroding beaches, have been done through:

- theoretical analyses using basic physical principles in concert with assumptions about the lower boundary layer and initial conditions,
- field observations that are "reality" but in which the investigator has no control over the physical conditions of the experiment,
- laboratory tests.

In terms of controlled conditions, laboratory tests are favored, using both small scale and "near-prototype" scale tanks. The prototype experiments against which the tests conducted here were compared were the SUPERTANK tests conducted at Oregon State University in 1991. The reference test series for the present project was Series STiO, which studied accretion toward equilibrium. In the present study, the wave heights and periods of STiO were reproduced at three scales, 1:10, 1:8.5 and 1:11 with both sinusoidal and cnoidal waves. Only sinusoidal waves were used in the prototype SUPERTANK test.

Most past studies have focused on eroding beaches since they are of primary concern from an engineering viewpoint. Except in dramatically retreating or advancing coastlines, beach morphology is generally seasonal, so that the erosion that removes sand from the beach face and stores it offshore is eventually reversed. Accretion follows. An understanding of the accretion portion of the cycle is important for several reasons:

- it provides a description of the entire cyclic cross-shore sediment transport process,
- estimating the extent and rate of post-storm beach recovery are important, and
- the process is applicable to the design of shore protection works.

"Sinusoidal waves" were produced by moving a wave paddle sinusoidally. The generated waves are not really sinusoidal but are referred to as sinusoidal waves here. Sinusoidal paddle movement introduces "free secondary waves". Small amplitude theory (linear theory) has been used in studies of beach evolution. Its validity, however, is questionable in shallow water because of the assumption of infinitesimal wave height. When an oscillatory wave moves from deep water into shallow water, the crest becomes higher, the curvature of wave profile increases and the trough becomes flatter. Cnoidal wave theory offers a better solution for finite amplitude waves in shallow water. Waves in shallow water can be represented by the cnoidal theory whose crests are peaked and narrow and troughs are flat.

Finite amplitude, long-period waves of permanent form propagating in shallow water are described well by the cnoidal wave theory developed by Korteweg and de Vries (1895). Cnoidal waves can be generated in the laboratory by moving the wave generator paddle according to an appropriate zeta function as determined by the desired Ursell number. The Ursell number is given by,

$$U = \frac{HL^2}{h^3} \tag{1.1}$$

where h = water depth, L = wave length and H = wave height.

Characteristics of cnoidal waves are described by elliptic integrals. Cnoidal theory is valid for $h/L<1/8$ when the Ursell number, $U>20$.

Cnoidal waves differ from sinusoidal waves in terms of profile shape and water particle velocities. The vertical pressure distribution is assumed hydrostatic in linear theory, but it is not hydrostatic for finite amplitude waves of permanent form in uniform depth of water. In section 2.2.a.1, Korteweg and de Vries equation is derived from Airy equations by adjusting the hydrostatic pressure distribution made in the linear theory by considering the vertical acceleration. The horizontal velocity distribution is constant from the water surface to the bottom. Near–bottom water particle velocities play a crucial role in sediment transport; therefore, it is important to simulate realistic beach conditions using cnoidal-like waves in shallow water. As the wave length approaches infinity, the cnoidal wave theory reduces to the solitary wave theory. Also, as the wave height to water depth ratio becomes small

(infinitesimally small wave height), the wave profile approaches a sinusoidal profile. Cnoidal wave theory is discussed in more detail in Chapter 2.

The following parameters and phenomena were investigated in the present study: incident and reflected wave energy spectra, reflection coefficients, phase angles between incident and reflected waves, apparent reflection points on the beach profile, and calculated bottom velocities calculated by shoaling the individual frequencies with the appropriate phase angles. A key finding was that the pattern of beach evolution, as well as the final profile, differed between cnoidal and sinusoidal of waves. The initial profile was always an offshore bar. As observed in the SUPERTANK tests, sinusoidal waves changed the beach profile incrementally, first building the berm and later changing the profile offshore. Cnoidal waves affected the whole profile as the beach moved toward a final equilibrium. The whole "body of the beach" was affected at once.

Evolution of the beach profile is related to changes in reflection coefficient with time for both types of wave. Sinusoidal wave reflection coefficients reached their highest value after 100 to 120 minutes and remained constant until the end of a test (500 to 550 minutes). Cnoidal wave reflection coefficients increased steadily throughout a test and only reached a constant value near beach equilibrium.

Phase angles between incident and reflected waves for each frequency were calculated and used to calculate apparent reflection points on the profile. In some cases the reflection point moved as the beach profile evolved and jumped one-half wave length seaward as the beach accreted. These jumps in reflection points may be linked to episodic events of profile adjustment. Rather than evolve toward equilibrium smoothly, profiles respond in discrete

jumps toward equilibrium. This may explain why differences in equilibrium profile depend on initial profile condition.

1.1. SCOPE OF THIS STUDY

The objective of the present study is to investigate the beach profile evolution under cnoidal waves since cnoidal theory offers a solution for finite height, periodic waves in shallow water. Sinusoidal waves with the same height and period were also run with the same initial profiles until equilibrium was attained. Results from the two series of tests were compared to improve understanding of beach profile evolution. To the writer's knowledge, no studies using cnoidal waves have been conducted with a movable bed.

A review of previous studies is presented in Chapter 2. Cnoidal wave theory and the generation of cnoidal waves is addressed. Chapter 2 also includes wave measurements and explains the Goda and Suzuki (1976) method for separating incident and reflected waves.

Experimental equipment and procedures are described in Chapter 3 including the wave tank, wave generation system and wave gages.

Data analysis methods are presented in Chapter 4. Fourier series, spectral analysis and examples of calculated and measured cnoidal waves are given. The procedure used to calculate phase angles between incident and reflected waves for each harmonic is discussed and an example presented. Apparent reflection point calculations are discussed.

Results are presented in Chapter 5. Discussion of the beach profile vis a vis incident and reflected wave conditions is included. The results of the numerical calculations and evolution

of the beach are presented in Chapter 6. Chapter 7 presents a summary and recommendations for further study.

CHAPTER 2. LITERATURE REVIEW

2.1. BEACH PROFILE STUDIES

Saville (1957) studied beach profile evolution in a large wave flume capable of producing near-prototype scale waves and beach conditions. The wave tank was 635 ft long, 20 ft deep and 15 ft wide. His experiments are referred to as Large Wave Tank (LWT) experiments. Sand with a median diameter of 0.22 mm was used on an initially plane 1:15 sloping beach. His data has been used extensively because of its near-prototype scale.

Kraus and Larson (1988) describe Saville's LWT experiments. Larson (1988) and Larson and Kraus (1989) investigated beach profile change by using the LWT data. The relationship between cross-shore transport and equilibrium was investigated. Four different regions for cross-shore sediment transport were identified and a numerical model, SBEACH, developed based on the different transport zones. Regression relationships between geometric characteristics of the profile such as bar volume, bar height, depth to bar crest and wave and sand properties were conducted. A criterion was developed to establish when bars and berms would form. Their relation is given by,

$$\frac{H_0}{L_0} = M\left(\frac{H_0}{wT}\right)^3 \tag{2.1}$$

in which, *Ho* = deepwater wave height*, *Lo* = deepwater wave length, *T* = wave period, *M* = 0.00070 and *w* = sediment fall velocity. Moving from offshore toward the beach, the profile was divided in four zones; (I) pre-breaking, (II) breaker transition, (III) broken wave, and (IV) swash zone. For zone (I) a net transport rate was estimated by an exponential decay with distance from the breaking point with an average decay coefficient of 0.18 m^{-1}. Zone (II)

* Notation is defined where it first appears and in Appendix A, Notation.

extends from break point to plunge point with an exponential decay transport rate of similar to that of Zone (I) but with a 0.20 m^{-1} decay coefficient. A modified transport rate was applied to Zone III given by,

$$q = K(D - D_{eq} + \frac{\varepsilon}{K}\frac{dh}{dx}) \ldots if \ldots D > D_{eq} - \frac{\varepsilon}{K}\frac{dh}{dx} \tag{2.2.a}$$

$$q = 0 \ldots if \ldots D < D_{eq} - \frac{\varepsilon}{K}\frac{dh}{dx} \tag{2.2.b}$$

in which, q = sediment transport rate, h = still water depth, x = horizontal distance, K = an empirical transport rate coefficient, D = wave energy dissipation per unit volume, D_{eq} = equilibrium energy dissipation per unit volume, and ε = transport rate coefficient for the slope-dependent term. A linear transport rate is assumed above the still water line in Zone (IV), the swash zone. Changes in the beach profile were calculated at each time step from the distribution of the onshore-offshore transport rate and the conservation of sand given by,

$$\frac{\partial q}{\partial x} = \frac{\partial h}{\partial t} \tag{2.3}$$

The model was numerically stable and simulated profiles as they approached equilibrium under constant wave conditions and water level.

Dean (1977) analyzed numerous beach profiles and suggested a power law to describe the profile shape similar to that originally proposed by Bruun (1954). The profile is given by,

$$h = Ax^{2/3} \tag{2.4}$$

where, A = a dimensional shape parameter. A is a function of wave energy dissipation and sediment size and is given by,

$$A = \left(\frac{24 D_*}{5 \rho g \sqrt{g} \kappa^2} \right)^{2/3} \tag{2.5}$$

in which, ρ = density of the water, g = acceleration of gravity, κ = breaking index equal to 0.78 and D_* = Uniform energy dissipation per unit volume for a given grain size. A and D are functions of the sand grain diameter, d. D_* is given by,

$$D_* = \frac{1}{h}\frac{dF}{dy} \tag{2.6}$$

in which, F = energy flux toward shore and y = shore normal coordinate. Energy flux is the product of wave energy per unit surface area (energy density) and group velocity.

$$F = \frac{\gamma H^2}{8} C_g \tag{2.7}$$

in which, γ = specific weight of water, H = wave height and C_g = group velocity.

The power law profile of Equation 2.4 states that for a given sediment size, the water depth is proportional to the two thirds power of the distance from the shoreline. It also indicates that beaches with coarser sand will have steeper slopes, an observation borne out by observation (Dean and Dalrymple, 2002).

Kriebel, Dally, and Dean (1986) conducted small scale wave tank experiments of beach profile recovery under beach-building wave conditions. Wave reflection was found to have a major effect on profile recovery. Reflection caused outer bars at the antinodes of partial standing waves due to reflection from the beach. These outer bars limited onshore sediment transport. The initial profile configuration was also important and had a major effect on the final equilibrium shape.

Carter, Liu and Mei (1973) studied the relationship between the development of offshore bars and wave reflection. They described the formation of multiple bars based on the presence of standing waves and a reversal of mass transport. The magnitude and direction of the mass

transport depended on the reflection coefficient. A critical reflection coefficient was found to be $Cr = 0.414$. For higher reflection coefficients the direction of net sediment movement was offshore and resulted in larger bedforms. Mass transport was in the direction of wave propagation for small reflection coefficients. For $Cr > 0.4$ sediment accumulated under the nodes of the partially standing waves.

The SUPERTANK Laboratory Data Collection Project (Kraus & Smith 1994) was conducted in 1991 as a large-scale experimental study. It was a near-prototype size beach profile evolution study.

A 76 m-long beach was constructed in a channel 104 m long, 3.7 m wide and 4.6 m deep. Broad and narrow band random waves and monochromatic waves were run with wave heights ranging from 0.2 m to 1 m and wave periods ranging from 3 to 10 seconds. The water depth was 3.05 m. Random wave tests used a TMA spectrum (developed from Texel, Marsen and Arsloe data) applicable to shallow depths. Waves were initially run in short bursts of 10 to 20 minutes and subsequently at 70 minutes. Sand used in the tests was well graded quartz with a median diameter of 0.22 mm and a fall velocity of 3.3 cm/sec. Profile surveys were measured along the channel center line and along two lines, 3 ft from each channel wall. Approximately 350 surveys were performed.

20 major tests were conducted during SUPERTANK. Each was started using the final profile of the previous test. From the 20 SUPERTANK tests, two tests were selected for study in the present work. These tests are described in Table 2.1.

Table 2.1 SUPERTANK tests replicated in present study

Test Number	Description	Wave height (meters)	Wave period (seconds)
ST10	Erosion toward equilibrium, random waves	0.8	3.0
STi0	Accretion toward equilibrium, monochromatic waves	0.5	8.0

ST10 was the first and longest duration SUPERTANK test. A TMA spectrum was used. Spectral width was changed during the test to observe changes in bar morphology. Wave period was increased from 3 seconds to 4.5 seconds. Some monochromatic waves were run in the same test to obtain data to improve beach profile numerical models.

STi0 was a test during which 0.5-meter-high, 8 second monochromatic accretionary waves were run. An equilibrium profile was achieved after about 570 minutes. During the experiment, in situ sediment density measurements were made and porosity calculated. Porosities ranged from 0.28 to 0.47. The starting profile for the test ST_I0 was the final profile of the previous test, ST_H0 (an erosion test conducted with monochromatic waves). The starting profile for ST_I0 had an offshore bar from the previous test. This bar moved toward shore during the test and was closer to shore at equilibrium.

2.2. CNOIDAL WAVES

Cnoidal theory, generation of cnoidal waves and shoaling of cnoidal waves are presented here.

2.2.a CNOIDAL WAVE THEORY

Korteweg and deVries (1895) developed the theory for a periodic long wave of permanent form in shallow water. It is described in terms of Jacobian elliptic functions, hence the name cnoidal due to the elliptic cosine function, cn. The crest of the cnoidal wave is more peaked and the trough is longer and flatter than a sinusoidal profile. Cnoidal wave theory describes shallow water, nearshore waves better than does small amplitude (sinusoidal) theory. The dimensional form of a cnoidal wave profile is given by,

$$\eta(x,t) = y_t - h + Hcn^2\left\{2K\left(\frac{x}{L} - \frac{t}{T}\right)\middle| m\right\} \tag{2.8}$$

in which, $\eta(x,t)$ = surface profile, y_t = height of the trough above the horizontal bottom, h = water depth, H = wave height, L = wave length, T = wave period, $K(m)$, the first complete elliptic integral, cn = Jacobian elliptic cosine function, and m = the elliptic modulus which defines the shape of wave. The Ursell number, U, used to define the applicable range and form of a cnoidal wave, is given by,

$$U = \frac{HL^2}{h^3} \tag{2.9}$$

The relationship between Ursell number U, and elliptic modulus m is given by,

$$U = \frac{16}{3}mK^2 \tag{2.10}$$

Laitone (1960) studied higher-order cnoidal waves and derived equations for engineering applications. Ippen (1966) gives the range of validity for cnoidal theory as 1/50<*h/L*<1/10. Hardy and Kraus (1987) cited Svendsen (1974) who provided tabulated values of the parameters necessary to calculate cnoidal waves and derived a deepwater limit for them. Wiegel (1964) gave the validity of cnoidal theory when h/L<1/8 to 1/10. Isobe et al. (1982), gave the deepwater limit as *h/L* = 0.2 indicating that Stokes and cnoidal wave theories have an overlapping range of Ursell numbers. Finite amplitude waves in deep and intermediate depth water are best described by the Stokes wave theory. When 25>*U*>10, both cnoidal and stokes theories are valid. Cnoidal theory is valid for Ursell numbers *U > 25*; Stokes theory is valid for Ursell numbers *U < 10.* The suggested range of validity of different wave theories is given in Figure 2.1 from the *Shore Protection Manual* (1984).

The elliptic modulus *m* can take values between 0 and 1. These two extreme values of *m* specify upper and lower boundaries for cnoidal theory. The value of *m* specifies the shape of the cnoidal wave.

a) For m→0, K(0) = $\frac{\pi}{2}$,U→0, and the Jacobian elliptic function cn(θ) becomes cos(θ). The cnoidal wave reduces to a sinusoidal wave;

$$\eta(x,t) = H\cos(\frac{2\pi x}{L} - \frac{2\pi t}{T}) \tag{2.11}$$

b) For m→1, *K(1)* = ∞, U→ ∞, and cn(θ) becomes sech(θ). The cnoidal wave reduces to the solitary wave,

$$\eta(x,t) = H\ \sec h^2\sqrt{\frac{3}{4}\frac{H}{h^3}}(x - ct) \tag{2.12}$$

Thus the limiting cases for cnoidal theory are sinusoidal and solitary waves. The solitary wave is totally above the still water surface and is specified only by its height, *H,* in water of depth, *h.* It travels without changing shape and is often used in laboratory experiments to represent shallow water waves. Different cnoidal wave shapes with their corresponding elliptic parameters and Ursell numbers calculated using the program developed for the present research, are given in Figure 2.2.

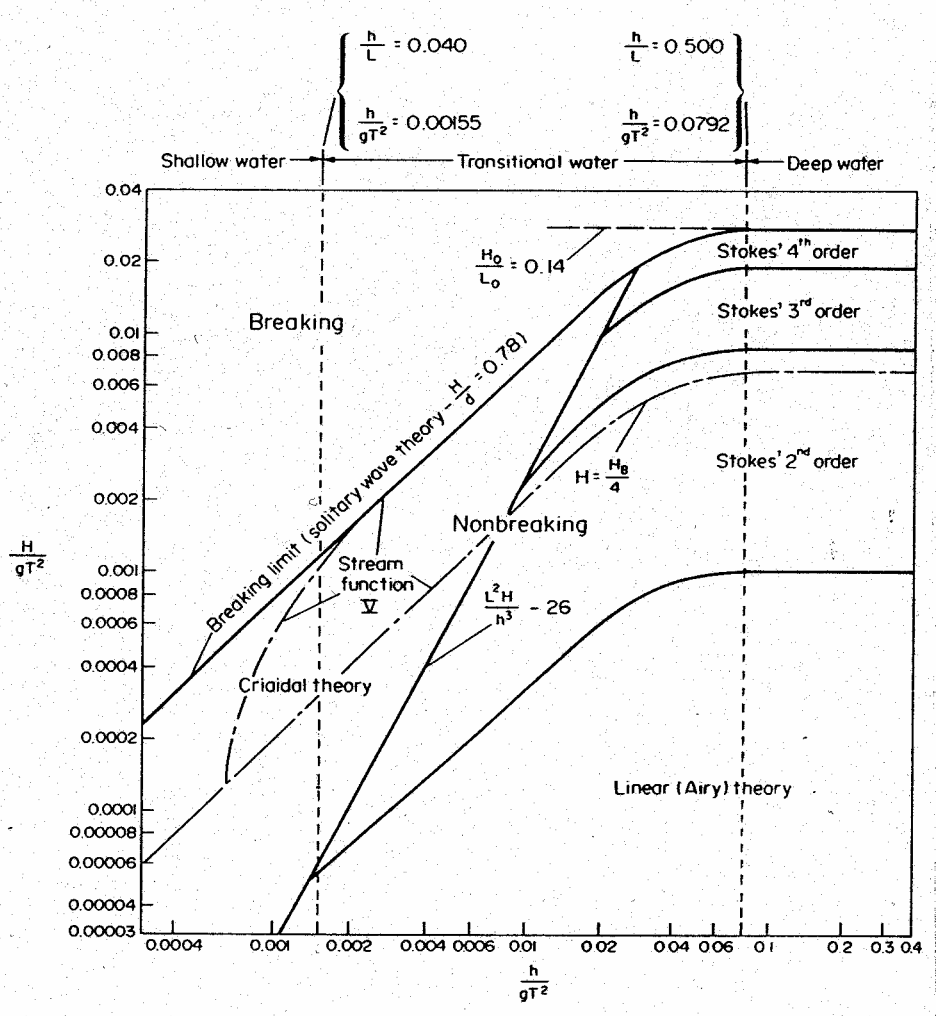

Figure 2.1 Regions of validity for various wave theories (Shore Protection Manual, 1984)

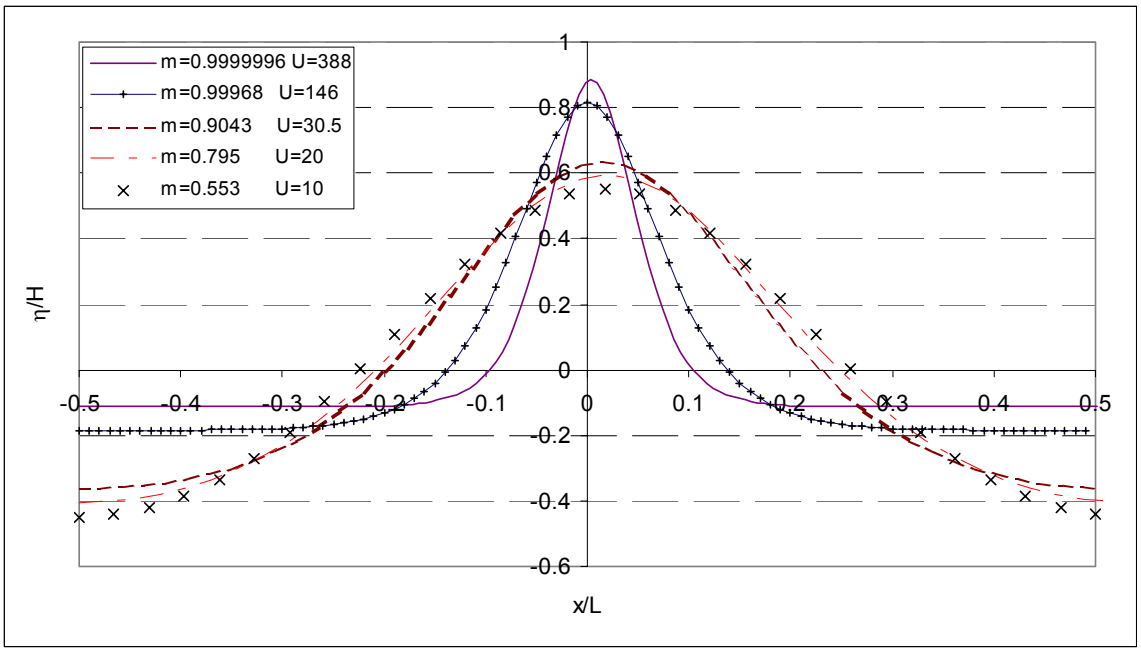

Figure 2.2 Cnoidal wave profiles as a function of the elliptic modulus, m

The Ursell number is also referred to as the Stokes parameter, because Stokes first pointed out the significance of the parameter (1847). The Ursell number is a comparison of amplitude dispersion (H/h) and frequency dispersion (h/L) in the following form,

$$U = \frac{H}{h}\left(\frac{L}{h}\right)^2 \tag{2.13}$$

A comparison of phase velocity expressions for linear (small amplitude) and non-linear (finite amplitude) waves shows the importance of the Stokes parameter. For linear shallow water waves, the phase velocity is given by,

$$c^2 = \left(\frac{w}{k}\right)^2 = \frac{g}{k}\tanh kh \tag{2.14.a}$$

Expanding in a Taylor series with *kh* to order 5,

$$c^2 = \frac{gh}{kh}\left[kh - \frac{1}{3}(kh)^3 + O[(kh)^5]\right] \tag{2.14.b}$$

In Eq. 2.14.b, frequency depends on wave length. Dispersion of waves in this theory is linear or frequency dispersion. However, for non-linear waves, c is given by,

$$c^2 = g(h+\eta) \tag{2.15.a}$$

and at the crest of a finite amplitude,

$$c^2 = gh(1+\frac{H}{h}) \tag{2.15.b}$$

In Eq. 2.15.b, frequency depends on wave height. Dispersion of this wave is non-linear or amplitude dispersion. Amplitude dispersion affects the wave so that higher parts travel faster than lower parts, resulting in steepening of the wave front. The wave front becomes vertical suggesting that finite amplitude waves have no permanent form in shallow water. This contradicts the observation by Scott Russel (1844). Shallow water waves of permanent form are possible if the increase in phase velocity due to nonlinearity (amplitude dispersion) and decrease due to frequency dispersion balance each other. This occurs when

$$gh(1+\frac{H}{h}) \cong gh\left[1-\frac{1}{3}(kh)^2\right] \tag{2.16.a}$$

or when

$$U = \frac{H/h}{(kh)^2} \cong O(1) \tag{2.16.b}$$

Finite amplitude waves of permanent form in uniform water depth (progressive waves without changing of form) are possible when frequency and amplitude dispersion are in balance. The simplest possible solution was first proposed by Korteweg and de Vries (1895). The balancing of dispersion effects can be achieved by adjusting the “hydrostatic pressure” assumption in shallow water wave theory by including the effect of vertical acceleration. An heuristic approach is given in section 2.2.a.1 to derive the Korteweg and de Vries equation from the Airy equations by adjusting the hydrostatic pressure distribution made in the Airy

theory by considering the vertical acceleration. The procedure used herein is adapted from Feir (1975).

Other cnoidal wave parameters are the phase speed (celerity) and height of the wave trough above the bottom. The celerity is given by,

$$c = \frac{L}{T} = \sqrt{gh}\left\{1 + \frac{H}{h}\left[\frac{2}{m} - \frac{3E}{mK}\right]\right\} \tag{2.17}$$

Wave height, H, is specified as $y_c = y_t + H$, where, y_c *and* y_t are the height of the wave crest and trough above the bottom respectively. The height of the wave trough above the bottom is given by,

$$y_t = \frac{H}{mK}(K - E) + h - H \tag{2.18}$$

where K and E are the first and second complete elliptic integrals, respectively, and g = acceleration of gravity. Wave height is given by, $H = a_c + a_t$ and $a_t = h - y_t$, in which a_c and a_t are distances from still water surface to the crest and trough, respectively. For a given depth, any two of the three parameters (H, L, and m) uniquely define a cnoidal wave. It is often the practice to specify wave period instead of wave length. The appropriate elliptic modulus, m, can be found iteratively if either the wave length or wave period is specified. Procedures for numerical evaluation of the elliptic functions can be found in Abromowitz and Stegun (1968), Goring (1978) and Dingemans (1997). A summary from Goring (1978) is presented in Appendix B.

Wave period, T, is a unique function of the elliptic parameter, m; however, Dingemans (1997) shows that for a given T, the elliptic parameter, m, is double valued. Two solutions for m are found when the wave period is specified. In numerical calculations care must be exercised so

that the appropriate solution is found. Dingemans (1997) states that for long waves in shallow water to exist,

$$T\sqrt{g/h} > 7 \tag{2.19}$$

where $T\sqrt{g/h}$ is a dimensionless wave period. For values of $T\sqrt{g/h}$ < 7, long waves in shallow water do not exist.

The potential and kinetic energy densities of a cnoidal wave are given by,

$$\frac{E_p}{H^2} = -\frac{1}{3m} + \frac{2}{3m}\left(1+\frac{1}{m}\right)\left(1-\frac{E}{K}\right) - \frac{1}{m^2}\left(1-\frac{E}{K}\right)^2 \tag{2.20.a}$$

and

$$E_k = \frac{c^2}{gh}E_p \tag{2.20.b}$$

where E_p and E_k are the potential and kinetic energies, respectively. Since $c^2 > gh$ in shallow water, $E_k > E_p$ for cnoidal waves. For linear waves $E_p/H^2 = 1/8$. Cnoidal wave potential energy from Equation 2.20.a is a function of the elliptic modulus m. For all values of m, Equation 2.20.a gives lower values than the potential energy than for corresponding linear waves. Thus, the kinetic and potential energy densities for cnoidal waves are less than for the corresponding linear wave of the same height and period.

2.2.a.1 DERIVATION OF KORTEWEG AND DE VRIES EQUATION:

The procedure used herein is adapted from Feir (1975). The classical shallow water (Airy) equations are given by Feir (1975) and Dingemans (1997),

$$u_t + uu_x + g\eta_x = 0 \tag{2.21}$$

$$\eta_t + [u(h_0 + \eta)]_x = 0 \tag{2.22}$$

where the subscripts t and x denote differentiation with respect to time and horizontal distance, respectively. The mean pressure over the depth $\overline{P}$ is given by,

$$\overline{P} = \rho g \eta \tag{2.23}$$

Then Eq 2.21 becomes,

$$u_t + uu_x + \frac{\overline{P}_x}{\rho} = 0 \tag{2.24}$$

Small amplitude, irrotational wave theory gives the velocity potential as,

$$\phi = \frac{ag}{w} \frac{\cosh k(y + h_0)}{\cosh kh_0} \sin\theta \tag{2.25}$$

where $\theta = kx - \omega t$ and dispersion relation is given by, $\omega^2 = gk \tanh kh_0$ and the water surface displacement is given by

$$\eta = -\frac{1}{g}\phi_t \Big|_{y=0} \tag{2.26}$$

evaluated at the free surface, $y = 0$. Hence,

$$\eta = a\cos\theta \tag{2.27}$$

The wave pressure is,

$$P = -\rho\phi_t \tag{2.28}$$

or,

$$P = \frac{\rho g a \cosh k(y + h_0)}{\cosh kh_0}\cos\theta \tag{2.29}$$

Then, $\overline{P}$, the mean pressure over the depth h_0 , is given by,

$$\overline{P} = \frac{1}{h_0}\int_{-h_0}^{0} P dy \tag{2.30}$$

or

$$\overline{P} = \rho g a \cos\theta \frac{\tanh kh_0}{kh_0} \tag{2.31}$$

which reduces to

$$\overline{P} = \rho g(\frac{\tanh kh_0}{kh_0})\eta \tag{2.32}$$

The Taylor series expansion of $tanhkh_0$ to order $(kh)^2$ gives,

$$\overline{P} = \rho g\left[1 - \frac{(kh_0)^2}{3}\right]\eta \tag{2.33}$$

Setting $\overline{g} = g\left[1 - \frac{(kh_0)^2}{3}\right]$, we have,

$$\overline{P} = \rho \overline{g} \eta \tag{2.34}$$

Taking the derivative with respect to *x*, we have,

$$\overline{P_x} = \rho \overline{g} \eta_x \tag{2.35}$$

Hence $\overline{g}$ includes the frequency dispersion effects of the shallow water wave equations. Feir (1975) gives the solution of Equation 2.21 (shallow water wave (Airy) equation) for particle velocity as,

$$u \cong c_0 \left[\frac{\eta}{h_0} - \frac{1}{4}\left(\frac{\eta}{h_0}\right)^2\right] \tag{2.36}$$

where, $c_0 = \sqrt{gh_0}$. To account for the hydrostatic pressure distribution assumption in terms of vertical motion, c_0 is $\overline{c_0} = \sqrt{\overline{g} h_0}$. Then $\overline{c_0}$ becomes,

$$\overline{c_0} = c_0 \left[1 - \frac{(kh_0)^2}{6}\right] \tag{2.37}$$

The particle velocity becomes,

$$u \cong \overline{c_0} \left[\frac{\eta}{h_0} - \frac{1}{4}\left(\frac{\eta}{h_0}\right)^2\right] \tag{2.38}$$

A solution is sought for a finite amplitude wave of permanent form in uniform depth of water by inserting Eq.2.38 into the shallow water equations, Eq. 2.21 and Eq. 2.22. The continuity equation, Eq.2.22, becomes,

$$\eta_t + h_0[u(1+\frac{\eta}{h_0})]_x = 0 \tag{2.39}$$

Substituting Eq.2.38 into Eq.2.39 and simplifying,

$$\eta_t + h_0\left[c_0\left[\frac{\eta}{h_0} + \frac{3}{4}\left(\frac{\eta}{h_0}\right)^2 - \frac{h_0 k^2}{6}\eta\right]\right]_x = 0 \tag{2.40}$$

Taking the derivative with respect to *x*,

$$\eta_t + c_0\left(1 + \frac{3}{2}\frac{\eta}{h_0}\right)\eta_x - \frac{c_0 {h_0}^2 k^2}{6}\eta_x = 0 \tag{2.41}$$

and the particle velocity becomes,

$$u = c_0\left[\frac{\eta}{h_0} - \frac{1}{4}\left(\frac{\eta}{h_0}\right)^2 - \frac{h_0 k^2}{6}\eta\right] \tag{2.42}$$

where $\eta = a\cos(kx - \omega t)$ differentiating with respect to *x* gives,

$\eta_x = k\eta$ and $\eta_{xx} = -k^2\eta$. Also $\eta_{xxx} = -k^2\eta_x$. Entering these into Eq. 2.41 and Eq.2.42 gives,

$$\eta_t + c_0\left(1+\frac{3}{2}\frac{\eta}{h_0}\right)\eta_x - \frac{c_0 {h_0}^2}{6}\eta_{xxx} = 0 \tag{2.43}$$

$$u = c_0\left[\frac{\eta}{h_0} - \frac{1}{4}\left(\frac{\eta}{h_0}\right)^2 - \frac{h_0}{6}\eta_{xxx}\right] \tag{2.44}$$

which are equivalent to the Korteweg and de Vries equations.

2.2.b SHOALING OF CNOIDAL WAVES

Local wave heights are used in calculation of bottom velocities. Wave heights were measured in horizontal part of the flume and shoaled across the beach profile by the shoaling of first order cnoidal theory. A discussion of shoaling of cnoidal waves is given in this section.

Svendsen and Brink-Kjaer (1972) analyzed the shoaling of cnoidal waves. They assumed constant wave period and that the wave energy flux through a vertical section remains constant as the water depth changes. Energy dissipation is not considered. This implies negligible wave reflection as the wave shoals. Energy flux, E_f, is defined by,

$$E_f = \rho g \eta^2 c \tag{2.45}$$

where ρ = density of water, c = phase celerity, η = surface profile. The energy transport per wave is,

$$E_{tr} = \rho g H^2 L / m^2 \left[\frac{1}{3}\left(3m^2 - 5m + 2 + (4m-2)\frac{E}{K}\right) - \left(1 - m - \frac{E}{K}\right)^2\right] \tag{2.46}$$

Shoaling was carried out by calculating E_{tr} at a reference point and then solving Eq. 2.9, Eq. 2.17, and Eq. 2.46 simultaneously for the desired depths. Since E and K are functions of m, the solution is iterative. A "shoaling equation" was derived by reducing four of the equations into one transcendental equation and a table was provided to solve the equation.

Svendsen and Buhr Hansen (1976) conducted laboratory experiments and compared sinusoidal with cnoidal shoaling. Energy dissipation due to friction was taken into account by assuming a laminar boundary layer. They found the cnoidal theory predicted the variation of wave height well even close to breaking. There was good agreement between experiments and theory for waves with small deep water steepnesses. The shoaling theory for cnoidal waves is valid for gently sloping bottoms. Shoaling over large bottom deformations is not described well.

Buhr Hansen (1980) studied cnoidal wave shoaling with an extensive series of experiments on a 1:33 slope. The variation of wave height and energy flux was predicted well by cnoidal theory for relatively small deep water wave steepness over gently sloping bottoms. For steep waves, deviations between the theory and experiments became more pronounced. He compared waves with Ho/Lo = 0.0019 and Ho/Lo = 0.0279. If the slope is too steep, the wave height can not adjust to the local water depth.

Hardy and Kraus (1987) calculated the shoaling of cnoidal waves with a second order theory. A perturbation method was used. Shoaling was calculated assuming that energy flux is conserved, wave period is constant and bottom friction is negligible. Numerical results were compared with experimental data from Buhr Hansen and Svendsen (1979). Their results are

shown in Figures 2.3 through 2.6. The notations cn I, cn II and SA in the figures refer to first order cnoidal theory, second order cnoidal theory and small amplitude theory, respectively. The results of the second order cnoidal wave theory fall between small amplitude and first order cnoidal theories. Second order cnoidal theory was closer to first order cnoidal theory for small deepwater wave steepnesses and closer to small amplitude theory for larger steepnesses. Second order cnoidal theory underpredicts wave height near breaking especially for steeper waves, e.g., H_o/L_o = 0.025 to 0.021 for T = 1.67 seconds as shown in Figures 2.3 and 2.4. First order cnoidal theory more closely describes wave height changes near breaking than does the second order theory, H_o/L_o = 0.025 for T = 2.5 seconds as shown in Figure 2.6. Also, small amplitude theory underpredicts the wave height near breaking. The variation of wave height calculated by second order cnoidal theory compares with small amplitude theory for large deep water wave steepness in deep to intermediate depth water.

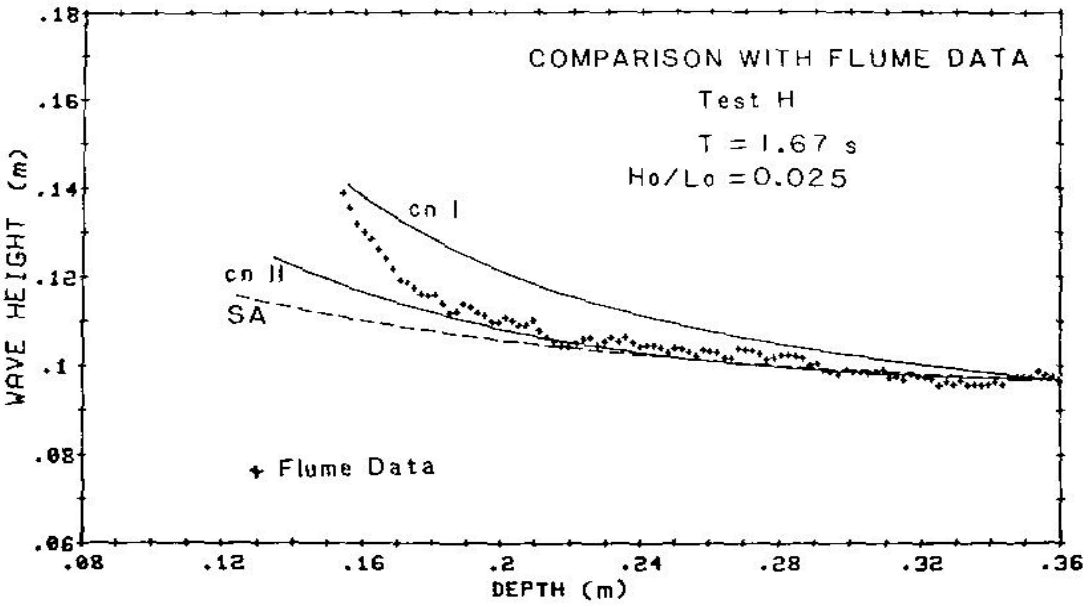

Figure 2.3 Shoaling of cnoidal waves for H_o/L_o = 0.025 (Hardy and Kraus, 1987)

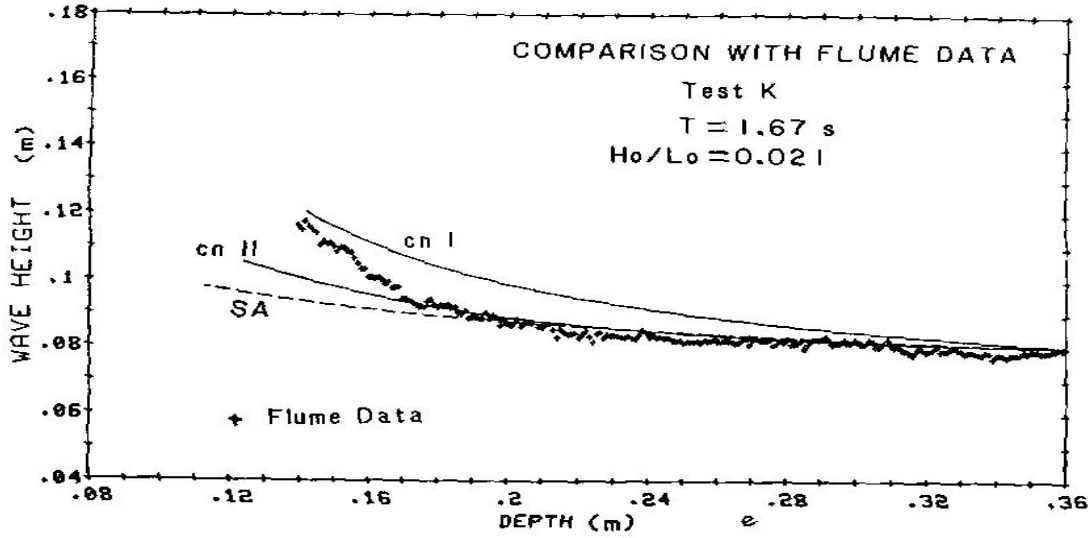

Figure 2.4 Shoaling of cnoidal waves for H_o/L_o = 0.021 (Hardy and Kraus, 1987).

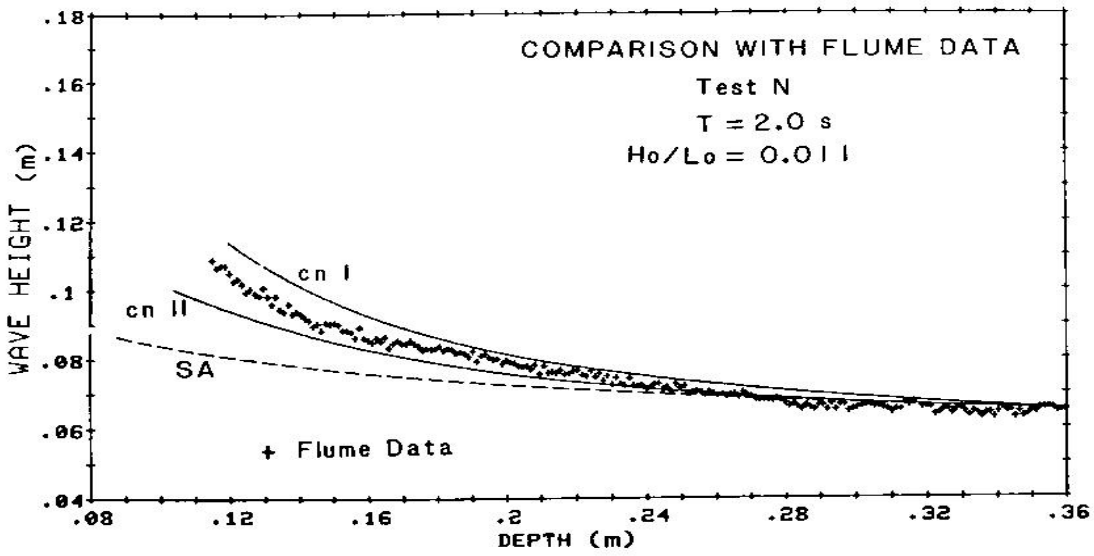

Figure 2.5 Shoaling of cnoidal waves for H_o/L_o = 0.011 (Hardy and Kraus, 1987).

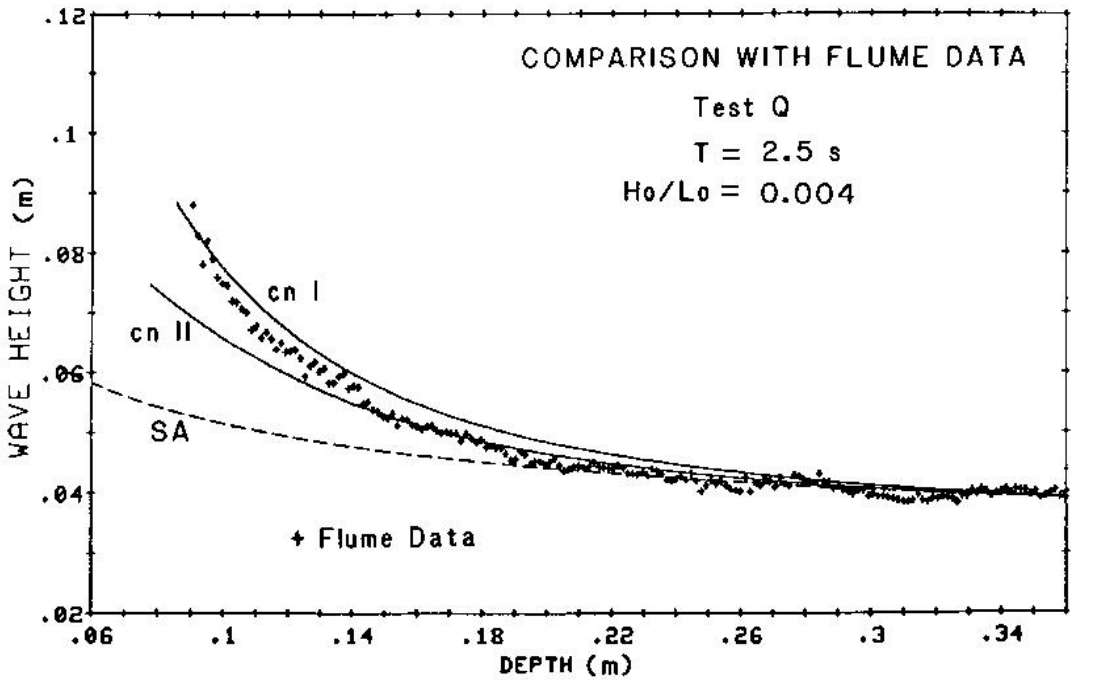

Figure 2.6 Shoaling of cnoidal waves for H_o/L_o = 0.004 (Hardy and Kraus, 1987).

2.2.c GENERATION OF CNOIDAL WAVES

Goring (1978) studied tsunamis in the laboratory using solitary and cnoidal waves. He developed a wave maker theory to produce cnoidal and solitary waves using a piston-type wave maker. His technique was adapted for the present study using a program developed in TurboC++. The code is given in Appendix C.

The basis of the theory is to match as closely as possible the motion of the wave paddle to the water particle motions of the desired wave. The rigid vertical paddle constrains the horizontal velocities in front of the paddle to be constant over depth. If the paddle displacement is ξ, and the depth averaged water particle velocity is $\overline{u}(\xi,t)$, then the paddle movement is,

$$\frac{d\xi}{dt} = \overline{u}(\xi,t) \tag{2.47}$$

During the forward stroke, the paddle must move faster to match the speed of the water particles under the cnoidal wave crest. During the backward stroke, the paddle moves slower under the trough. This requires a temporally asymmetrical trajectory. An example bulkhead displacement is given in Figure 2.7. The time averaged horizontal velocity is given by;

$$\overline{u}(x,t) = \frac{c\eta(x,t)}{h+\eta(x,t)} \tag{2.48}$$

It is also assumed that the wave has the following form;

$$\eta(\xi,t) = H[f(\theta)] \tag{2.49}$$

where $\theta = k(ct - \xi)$. Substituting Eq. 2.48 and Eq. 2.49 in to Eq. 2.47 yields,

$$\frac{d\xi}{dt} = \frac{H[f(\theta)]}{kh} \tag{2.50}$$

Integrating Eq. 2.48 gives the displacement of the wave paddle as a function of time.

$$\xi(t) = \frac{H}{kh}\int_0^{\theta} f(w)dw \tag{2.51}$$

in which w is a dummy variable. Eq. 2.49 was solved numerically by Newton's rule. θ is found iteratively for a given time from the following;

$$\theta^{(i+1)} = \theta^{i} - \frac{2Kht/T + (y_t - H(1-m)/m)\theta^{i} + HE(\theta|m)/m}{y_t + Hcn^2(\theta|m)} \tag{2.52}$$

and the displacement ξ is found from;

$$\xi = ct - \theta/k \tag{2.53}$$

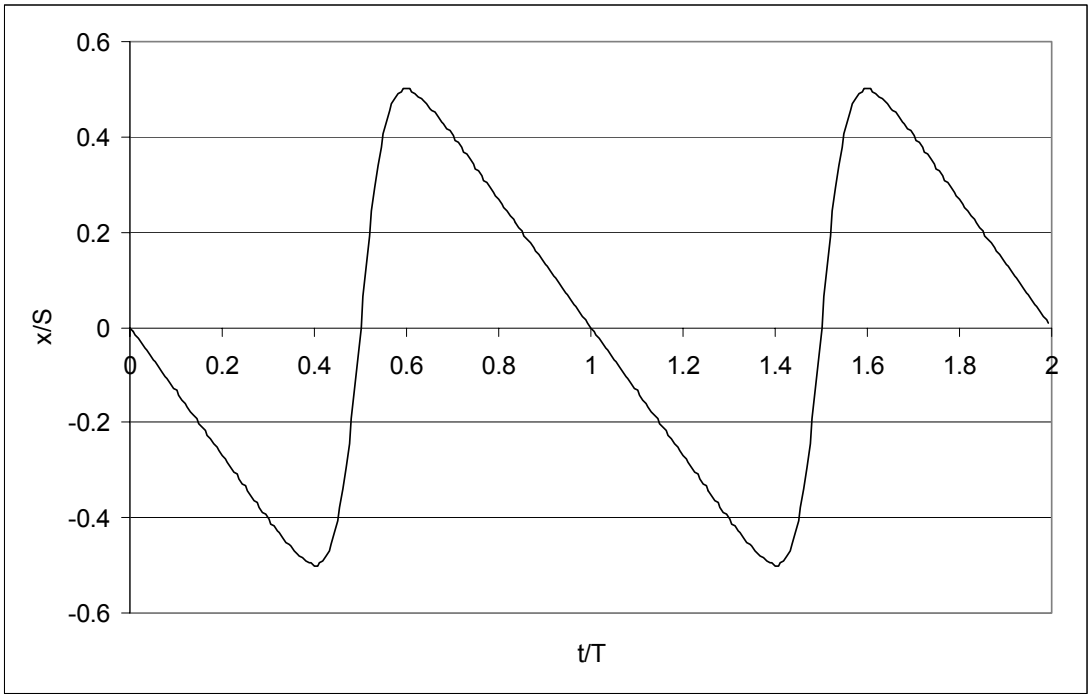

Figure 2.7 Paddle displacement for a cnoidal wave for U = 388, m = 0.9999996

2.3. WAVE MEASUREMENTS

Goda and Suzuki (1976) present a technique to estimate incident and reflected wave spectra from data collected simultaneously from two wave gages spaced some distance apart. A Fast Fourier Transform (FFT) technique is employed to estimate incident and reflected waves and the incident and reflected wave spectra that result. Reflection coefficients are determined from the ratio of incident to reflected wave heights.

If incident and reflected wave amplitudes are denoted as a_I and a_R, the surface elevations of incident and reflected waves, η_I and η_R, are given by,

$$\eta_I = a_I \cos(kx - \sigma t + \varepsilon_I) \tag{2.54}$$

$$\eta_R = a_R \cos(kx - \sigma t + \varepsilon_R) \tag{2.55}$$

in which, k = wave number, σ = angular frequency, and ε_I and ε_R = the phase angles of the incident and reflected waves, respectively. Surface elevations recorded at the first gage, η_1, can be represented as,

$$\eta_1 = (\eta_I + \eta_R) = A_1 \cos(\sigma t) + B_1 \sin(\sigma t) \tag{2.56}$$

where A_1 and B_1 are given by,

$$A_1 = a_I \cos\phi_I + a_R \cos\phi_R \tag{2.57}$$

$$B_1 = a_I \sin\phi_I - a_R \sin\phi_R \tag{2.58}$$

in which, $\phi_1 = kx_1 + \varepsilon_1$ and $\phi_R = kx_1 + \varepsilon_R$.

Similarly surface elevations at the second gage, η_2, a distance Δl from first, is given by,

$$\eta_2 = A_2 \cos(\sigma t) + B_2 \sin(\sigma t) \tag{2.59}$$

and the Fourier components A_2 and B_2 are given by,

$$A_2 = a_I \cos(k\Delta l + \phi_I) + a_R \cos(k\Delta l + \phi_R) \tag{2.60}$$

$$B_2 = a_I \sin(k\Delta l + \phi_I) - a_R \sin(k\Delta l + \phi_R) \tag{2.61}$$

Based on the above, the incident and reflected wave amplitudes are given by,

$$a_I = \frac{1}{2|\sin k\Delta l|}\sqrt{(A_2 - A_1 \cos k\Delta l - B_1 \sin k\Delta l)^2 + (B_2 + A_1 \sin k\Delta l - B_1 \cos k\Delta l)^2} \tag{2.62}$$

$$a_R = \frac{1}{2|\sin k\Delta l|}\sqrt{(A_2 - A_1 \cos k\Delta l + B_1 \sin k\Delta l)^2 + (B_2 - A_1 \sin k\Delta l - B_1 \cos k\Delta l)^2} \tag{2.63}$$

This method can be applied to both random or monochromatic wave records. Goda and Suzuki (1976) recommended that the wave gage spacing be,

$$0.05 < \frac{\Delta l}{L} < 0.45 \tag{2.64}$$

where Δl = distance between the two wave gages and L = wave length.

Goda and Suzuki (1976) also show that there is a singularity in the calculated incident and reflected wave heights when the wave gages are one-half wave length apart. Furthermore, they recommend that the gages be placed on a horizontal bottom (both gages in the same water depth) and at least one wave length from any reflecting body including the wave maker itself. Digitized wave data must be obtained nearly simultaneously at each of the two gages.

Mansard and Funke (1980) present a method to separate incident and reflected waves using simultaneous records from three gages. They employ a least squares method that gives good agreement when compared with laboratory measurements. Their method minimizes

sensitivity to noise and gage spacing. In their tests they observed energy transfer between frequencies due to reflection and amplification of transmitted energy in the reflected energy.

2.4. PCGODA

In the present study a computer program PCGODA was used to separate incident and reflected waves. It was developed by Goda (1976) and modified Hughes (1992). The method of Goda and Suzuki (1976) was adapted by using the Cooley-Tukey FFT. The program requires three wave gages. The program first analyzes Gages 1 and 2, and then Gages 1 and 3 using the Goda and Suzuki method. The user can interactively limit the frequency range over which the reflection analysis is performed. Incident and reflected wave spectra and the reflection coefficient based on those spectra are calculated for Gage 1 and Gage 2 and for Gage 1 and Gage 3 based on their spacing. Average values of incident and reflected spectra and incident and reflected wave heights result.

CHAPTER 3. LABORATORY EXPERIMENTAL FACILITIES AND PROCEDURES

3.1. WAVE TANK

Experiments were conducted in Drexel University's Hydraulics Laboratory wave flume. The flume is 96 ft long, 2.5 ft deep and 3 ft wide. The sides and bottom of the flume are of 0.5 in-thick tempered glass. The flume is 2 ft above ground and supported by aluminum bents every 5 ft along its length. The flume is shown schematically in Fig. 3.1. A programmable wave maker is installed at one end of the flume and a sand beach constructed at the other.

To reduce the load on the glass bottom, a wooden frame was built to support the sand beach. The offshore part of the sand beach rested on the glass bottom while the onshore part rested on the support structure. A non-woven composite geotextile was placed on the wooden frame to support and retain the sand. The geotextile is a geonet with geotextile layers on both sides. The sand beach was constructed on the geotextile. A cross-section of the flume is shown in Figure 3.1. An *in-situ* infiltration test was performed to investigate the permeability of the beach. Details of the infiltration test and data on the permeability of the beach are given in Appendix D.

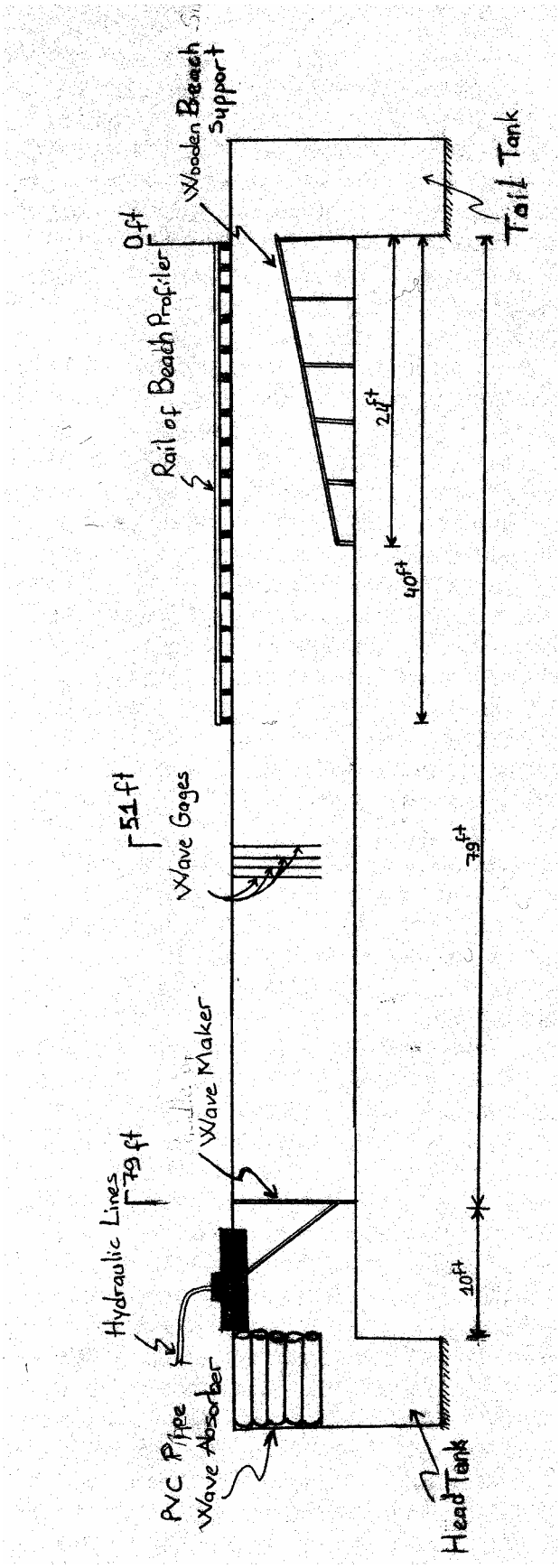

Figure 3.1 Schematic sketch of Drexel University wave flume

3.2. WAVE GENERATION SYSTEM

A hydraulically actuated, piston-type programmable wave generator is installed at one end of the wave flume as shown in Figure 3.2. It consists of a wave paddle, an hydraulic unit, a control unit, and an active wave absorption system. The paddle has a maximum travel of 3 ft on rails supported by a frame fixed to the floor and isolated from the flume. Rubber seals are attached along the sides and bottom of the paddle.

A double-acting hydraulic piston controls the paddle movement by fluid pressure supplied by the hydraulic unit through two hydraulic lines. Control signals are generated by a computer program (WAVEGEN) provided by the manufacturer, HR Wallingford (1996). The signals sent by WAVEGEN through the control unit box are converted to hydraulic pressures by the hydraulic unit.

The wave generator can produce regular and random waves by responding to signals produced by the wave generation software, WAVEGEN. The system can also take an external signal to specify wave paddle displacement. WAVEGEN runs on a personal computer and can produce a desired wave height and period in a specified water depth. The program specifies bulkhead displacements and sends them to the control unit. WAVEGEN uses digital filters pre-programmed to generate monochromatic waves, bichromatic waves, solitary waves, and a number of wave spectra including Pierson-Moskowitz, JONSWAP, Darbyshire, Neumann and Bretschneider spectra.

Figure 3.2 Wave generator hydraulic unit.

Along with the pre-programmed waveforms, WAVEGEN allows a “user-defined sequence” to specify any desired bulkhead displacement sequence in an ASCII text file. Thus, cnoidal waves and a TMA. spectrum could be generated for the present study. WAVEGEN also provides ramp-up and ramp-down times at the start and end of a run.

The number of user-specified points in the ASCII file is limited to 32,000, which in turn limits the duration of a test. An animation of paddle movement and the characteristics of the desired waves can be viewed on the computer screen prior to sending the signal to the control unit.

The control unit provides a variety of options. An external signal generator can be connected to the control unit box. A control switch on the control unit box lets the user position the wave paddle manually so it starts at the same position for each run. Another switch controls the hydraulic unit. An active wave absorption system is also available.

The absorption system can absorb waves reflected from a beach or other structure by a dynamic wave absorption system. Two parallel wire sensors on the front of the paddle measure the water level. This signal is converted into an “equivalent paddle position signal” and compared with the demand signal from WAVEGEN. The difference between the two signals is calculated and used to correct the paddle position. Compensation for the cable connecting the parallel wires to the control unit box was made during wave maker installation. Adjustment of the absorption system was made whenever the water level was changed.

3.3. WAVE MEASUREMENTS

Waves were measured using four parallel-wire resistance wave gages. A sketch of a wave gage is shown in Figure 3.3. It consists of two parallel stainless steel wires 0.01 inch in diameter spaced 0.16 inch apart. The wires are insulated from each other and stretched between the ends of a ¼-inch diameter brass rod. The resistance between the two stainless steel wires varies with the water level changes. Voltage changes due to resistance changes are converted to digital signals and recorded with a data acquisition system. The gages were connected to a signal preprocessor by shielded cables and connected to the data acquisition system. The signal preprocessor is used to calibrate and adjust the drift of the signals.

The wave gages were calibrated manually by moving them up and down in known increments over the range of expected water surface variation. The range of calibration was generally from 6 cm above the expected maximum water level to the bottom of the wave gage. Depth of immersion was changed in 3 cm increments and the voltage recorded. Gages were calibrated before and after each run and an average calibration used. A second-order polynomial was fitted to the average calibration data and used to determine water surface fluctuations. A typical calibration and wave record time series are given in Figure3.4. The corresponding calibration curve is given in Figure3.5.

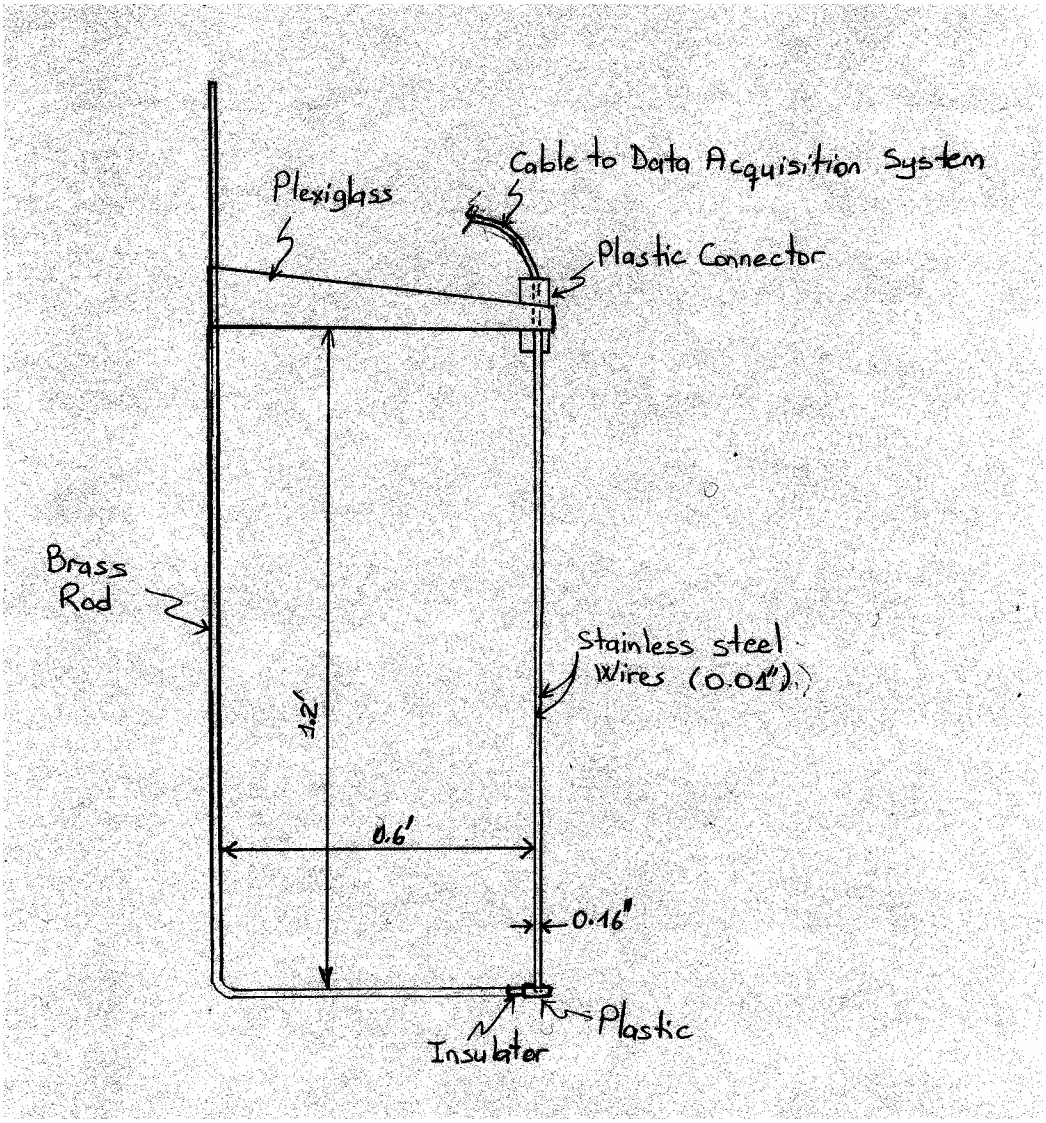

Figure 3.3 Schematic sketch of the resistance wave gage

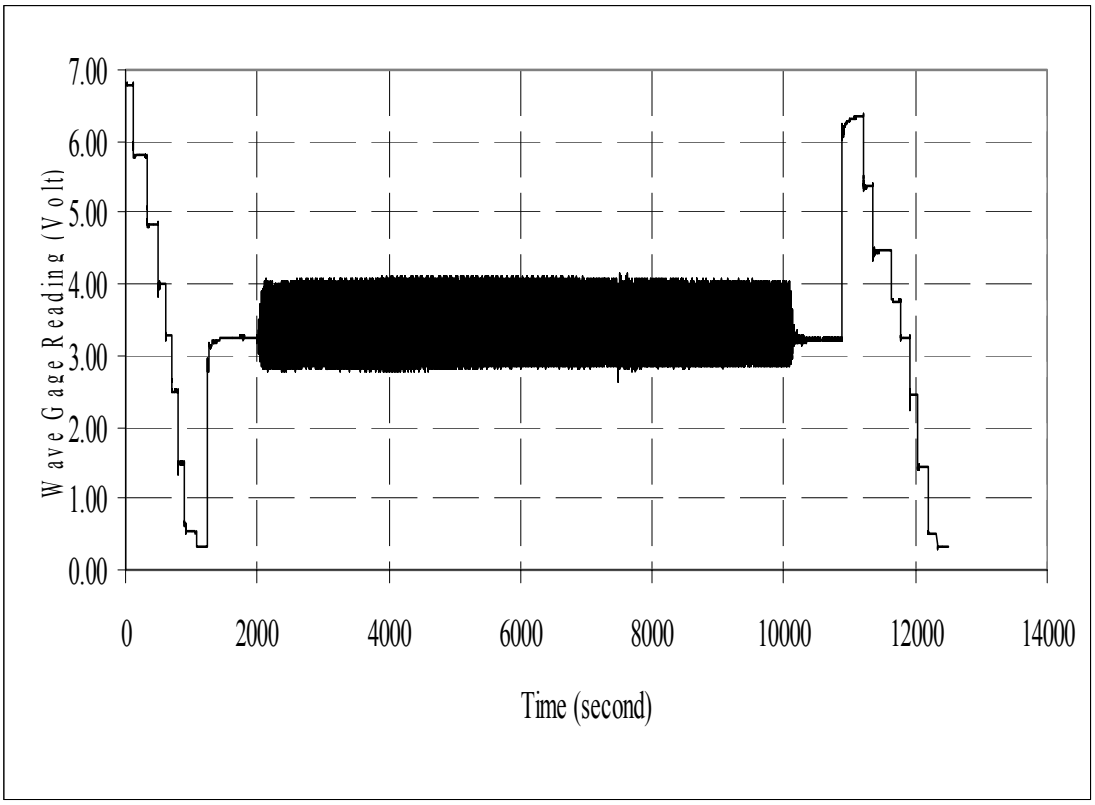

Figure 3.4 Time series of a wave record showing calibration at beginning and end of test run.

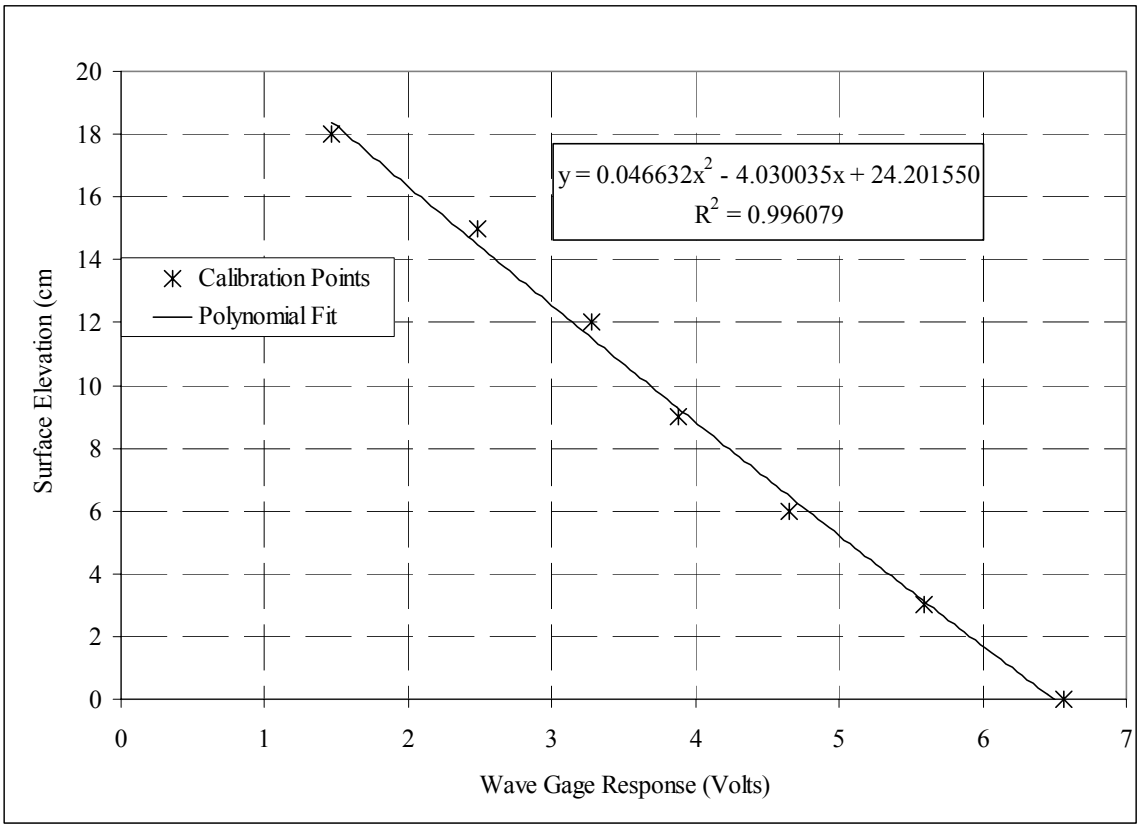

Figure 3.5 Example wave gage calibration

The distance between wave gages was changed in some tests; however the distances suggested by Goda and Suzuki (1976) were generally used. The minimum spacing should be more than 10 % of the wave length and the maximum spacing less than 45 %. Wave gages were located in the middle of the wave flume, as shown in Figure 3.1.A fourth wave gage was positioned 51 ft from the tail tank. The positions of wave gages were approximately two wave lengths away from wave paddle and one wave length away from the beach. Wave gage wires were cleaned before each run.

3.4. DATA ACQUISITION SYSTEM

An HP Agilent 34970A data acquisition system was used to measure and record the DC voltage from the wave gages. It can take 600 readings per second on a single channel with scan rates of up to 250 channels per second and can store up to 50,000 time stamped readings. In the present tests, the data acquisition system obtained 6 data points per second for each channel with a scan interval of 1/27 (0.037) seconds between consecutive channels. Recorded data were exported to an Excel spreadsheet. The system has a real-time display unit. Performance of the four wave gages was monitored through the display unit.

3.5. BEACH PROFILE ELEVATION MEASUREMENTS (BEACH PROFILER)

Beach profile measurements were obtained with a profiler system developed for the present experimental program. The profiler moves on a carriage on rails on top of the flume. The V shaped aluminum rail is 40 ft long and is level to ± 0.003 ft. The beach profiler is shown in Figure3.6.

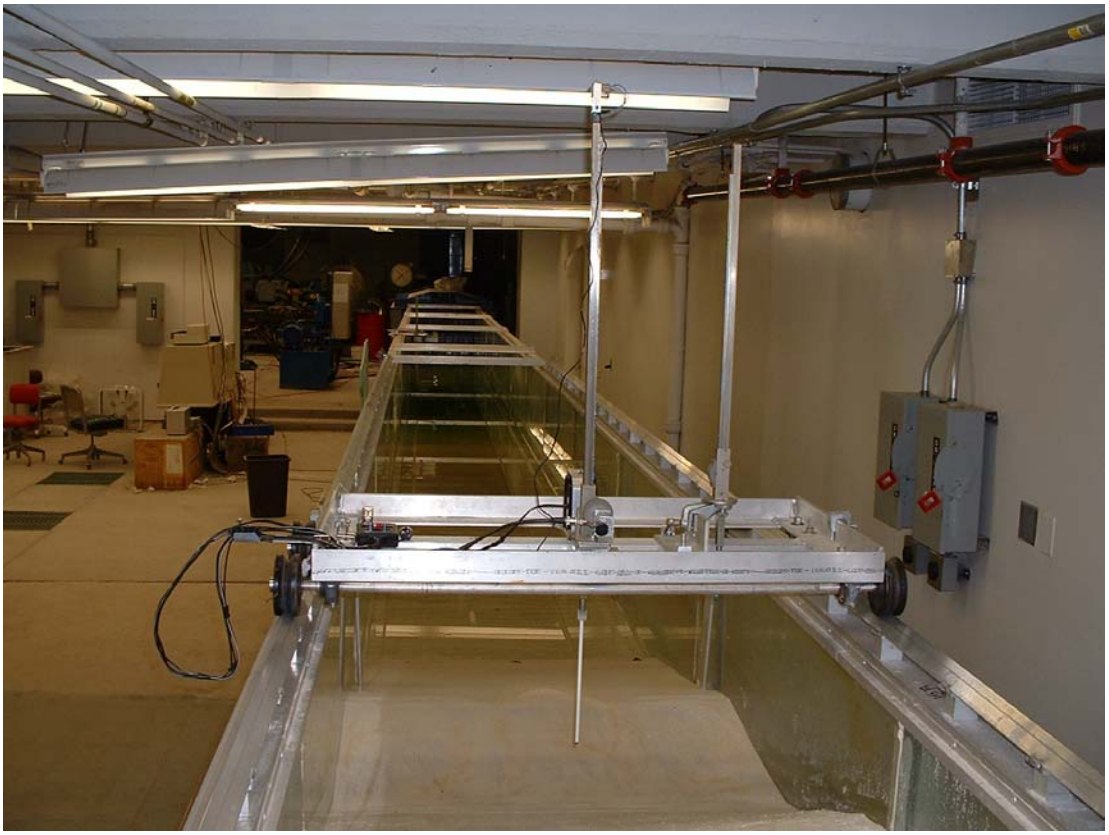

Figure 3.6 Beach Profiler, view looking toward wave generator

The profiler consists of a point gage staff that can be moved vertically, a vernier scale to read vertical distance, a sensor that lights when the profiler probe touches the beach surface and a motor to move the point gage vertically. A steel tape on the side of the aluminum rail was used to measure horizontal position. The profiler was moved horizontally manually and its position read from the steel tape. A motor moved the point gage vertically and the vertical distance was read from the vernier scale. A lightweight rod hung with a spring is used with a relay switch as a sensor. The sensor stopped the profiler when the probe touched the beach surface. Horizontal and vertical readings were read to ± 0.001 ft.

Readings were usually taken when the profiler was positioned along the center line of the channel; however, it is possible to position the profiler on either side of the carriage to measure profiles off the centerline. Data was entered into an Excel spreadsheet as it was obtained. Errors could be checked in real time from a plot of the data generated as the measurements progressed.

3.6. BEACH

Beach profiles were constructed between 17 ft and 40 ft of the wave flume (see Figure 3.1) at three different scales. Measurements are given relative to tail tank where the 0 ft station starts. The horizontal length of the beach profile varied for each test depending on the scale. Quartz sand was used to build the beach. Sand with a median grain size diameter of d_{50} = 0.22 mm was used in the SUPERTANK experiment which served as a prototype for the present tests. Commercially available Ottawa F-55 sand with a similar median grain size diameter was used in this study. A comparison of the sediment size distribution for the SUPERTANK sand and the sand used in this study is shown in Figure 3.7.

.

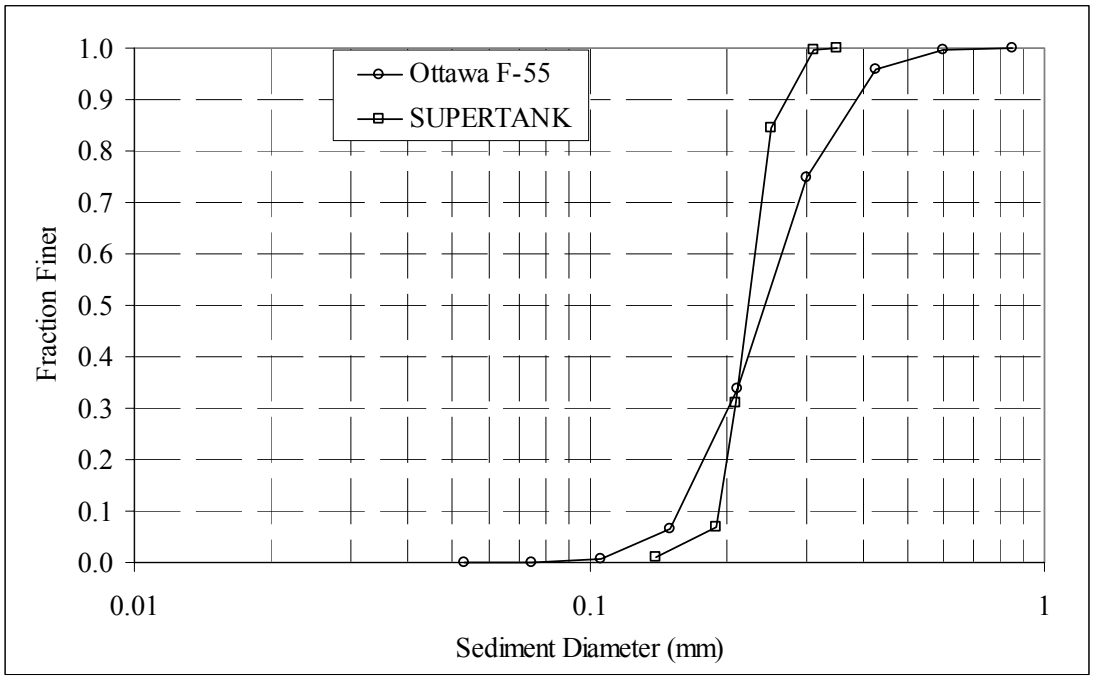

Figure 3.7 Sediment size distribution for sand used in this study (Ottawa F-55) and for sand used in SUPERTANK test.

The initial beach profile was constructed by adding sand to the flume while running low amplitude, high frequency waves so that the sand was deposited in a wave environment. The shape of the desired initial profile was drawn on the side wall of the flume and the profile graded to this template. In addition to periodic profile surveys, a video camera was used to record beach profile evolution. The beginning of a test, changes in profiles and wave conditions, and the conclusion of a test were all recorded. A 3 in. by 3 in. grid on the glass side of the flume was used as a reference for analysis of the videotapes. After each run, still photographs of the profiles were taken. The still photographs were used to measure the offshore part of the profiles beyond the profiler's reach.

3.7. EXPERIMENTAL PROCEDURES

Wave gages were left at their zero positions for 30 minutes to reach a stable value before beginning a test. The data acquisition system was turned on and the wave gages calibrated. WAVEGEN was run and signals on the control unit checked prior to starting the hydraulic unit. The absorption system was monitored through the wave probe monitor. The wave paddle position was controlled and adjusted manually. The hydraulic unit was started and waves produced. Additional measurements of waves, including wave heights at different locations, breaking wave heights and their locations, standing wave heights and their locations were carried out manually and recorded in a laboratory log book along with observations of profile changes. After each run, the wave gages were recalibrated and the distance between gages recorded. Water temperature was noted and the final shape of the profile drawn on the glass sidewall of the flume.

The wave generator was off when profiles were measured. Profile elevation readings were taken in horizontal increments of approximately 0.06 ft and special care was given to ripple measurements.

The water level was checked before each run and water added if necessary. After each test, the water was drained and the flume cleaned.

CHAPTER 4. ANALYSIS

This chapter describes the analytical program parameters and the analytical methods used to derive characteristics such as the spectra of incident and reflected waves, reflection coefficients, phase angles between incident and reflected waves at the measurement point, reflection points, calculated bottom velocities and beach profile evolution under the wave conditions investigated. An investigation of re-reflected waves is also presented.

4.1. ANALYTICAL METHODS

Expanding upon the physical theory presented in the literature survey in Chapter 2, a summary of the theoretical basis of the calculations used in the present study is given here.

4.1.a FOURIER SERIES AND SPECTRAL ANALYSIS

Spectral analysis for this study was based on Fourier series representation of a time series. Components of Fourier series were used to estimate the power spectrum (energy per unit frequency bandwidth) in the spectral analysis. Any finite length, periodic time series can be represented by a linear summation of sine and cosine series, termed a Fourier series (Bendat and Piersol 1971). A time series is said to be periodic if the function can be represented as;

$$f(t) = f(t + mT) \tag{4.1}$$

where m is an integer, T is the interval of periodicity or period. The Fourier series is given by,

$$f(t) = a_0 + \sum_{n=1}^{n=\infty} a_n \cos n\sigma t + \sum_{n=1}^{n=\infty} b_n \sin n\sigma t \tag{4.2}$$

where, n is an integer and $\sigma = \frac{2\pi}{T}$, a_0, a_n, and b_n are the Fourier components given by,

$$a_0 = \frac{1}{T}\int_t^T f(t)dt \tag{4.3}$$

$$a_n = \frac{2}{T}\int_t^{t+T} f(t)\cos n\sigma t dt \tag{4.4}$$

$$b_n = \frac{2}{T}\int_t^{t+T} f(t)\sin n\sigma t dt \tag{4.5}$$

Alternatively, using the Euler formula ($e^{\pm ix} = \cos x \pm i \sin x$), the Fourier series can be expressed as,

$$f(t) = c_0 + \sum_{n=1}^{n=\infty} c_n \cos(n\sigma t - \varepsilon_n) \tag{4.6}$$

where $c_0 = a_0$, ε = phase angle, and c_n is called the amplitude spectrum given by,

$$c_n = \sqrt{{a_n}^2 + {b_n}^2} \tag{4.7}$$

ε_n , called phase spectrum, is defined over the range 0 and 2π, given by;

$$\varepsilon_n = \tan^{-1}\left(\frac{b_n}{a_n}\right) \tag{4.8}$$

The energy spectrum is defined in terms of the amplitude spectrum as;

$$\frac{c^2}{2} = \frac{{a_n}^2 + {b_n}^2}{2} \tag{4.9}$$

Since the data being analyzed has a finite length, the spectra are “discrete”. The result of the above energy spectrum calculation is symmetrical having two sides. A one sided spectrum is obtained by doubling the values of one side and omitting the other.

An alternative procedure is to use the complex form of the Fourier series given by,

$$f(t) = \sum_{n=-\infty}^{n=\infty} F(n) e^{in\sigma t} \tag{4.10}$$

where the F(n) are complex components of the Fourier series given by,

$$F(n) = \frac{1}{T} \int_{t}^{t+T} f(t) e^{in\sigma t} dt \tag{4.11.a}$$

$$F(n) = a_n^{\,*} - i b_n^{\,*} \tag{4.11.b}$$

where the complex components are related to the real components as $a_n^{\,*} = \frac{a_n}{2}$ and $b_n^{\,*} = \frac{b_n}{2}$.

Most FFT programs require that the number of data points, n, be a power of 2.

4.1.a.1 EXAMPLE OF CALCULATED AND MEASURED CNOIDAL WAVES

A comparison of a measured cnoidal wave profile generated for DSTI02 test with H = 5 cm, T = 2.53 sec, d = 33.1 cm U = 27.7 with the theoretical cnoidal profile is given in Figure 4.1.a. The cnoidal program developed in the present study was used to calculate the theoretical wave profile in Figure 4.1.a. In the present study waves were measured using 3 gages. Details of the wave measurements are discussed in Chapter 3. The wave profile was measured approximately 1 wave length from the beach and about the same distance from the wave maker. Comparison of energy spectral analysis for calculated and measured cnoidal waves are given in Figure 4.1.b. PCGODA was used to calculate the energy spectra in Figure 4.1.b.

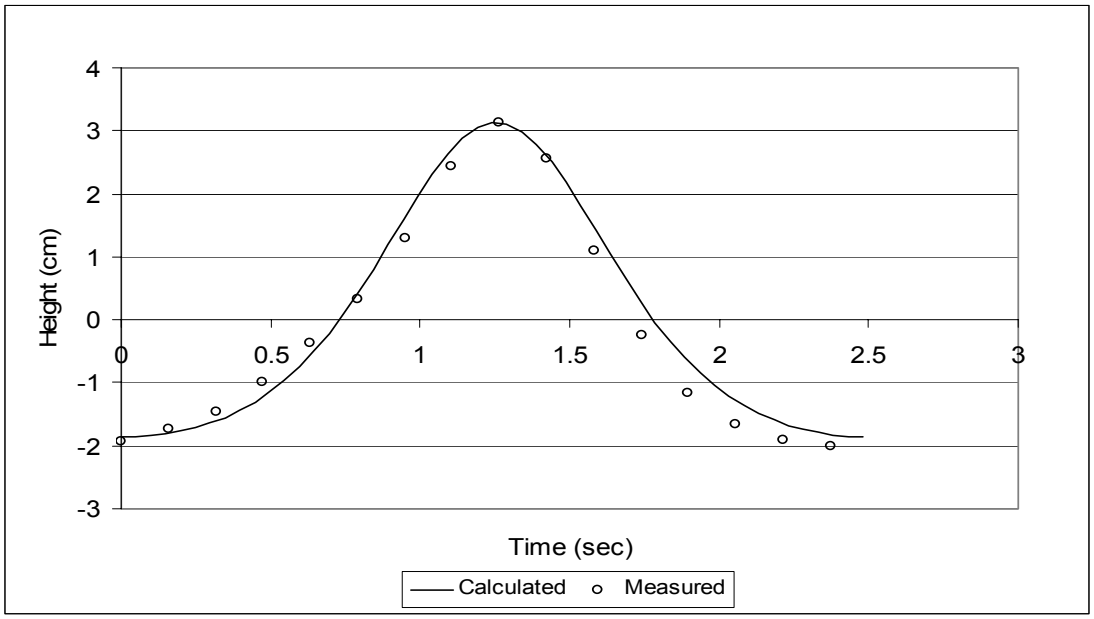

Figure 4.1.a Comparison of calculated and measured cnoidal wave profile for DSTI02 with H = 5 cm, T = 2.53 sec, d = 33.1 cm U = 27.7

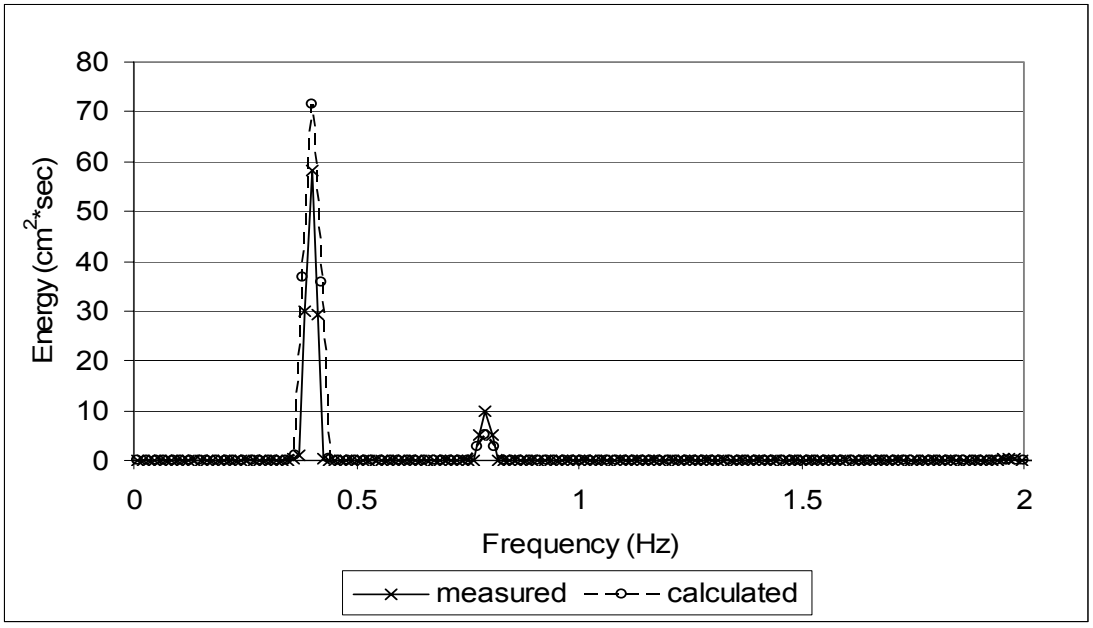

Figure 4.1.b Energy spectra for calculated and measured cnoidal wave for DSTi02, H = 5 cm, T = 2.53 sec, d = 33.1 cm U = 27.7

4.1.b PHASE SPECTRUM

The phase relationship between incident and reflected waves propagating across a sand beach was calculated for this study. To calculate the phase angles, the similarity between calculating the reflection coefficient and the frequency response of a system was recognized. Phase angles were given as a function of the reflection coefficients components. Theory and method of calculation of a frequency response of a system is given by Bendat and Piersol (1971), and Emery and Thomson (2001). A summary from Santamarina and Fratta (1998) is given here.

If a system is excited with different frequencies, then an array of complex numbers, H_u can be assembled, where H is the frequency response of a system. If *x(t)* and y*(t)* are input and output functions of a system, then the relation can be shown as;

$$y(t) = H_u x(t) \tag{4.12}$$

Incident and reflected wave records are taken as input and output functions respectively and the frequency response function calculated as;

$$H_u = \frac{Y_u}{X_u} \tag{4.13}$$

where, X_u and Y_u are the Fourier transform components of the incident and reflected waves in complex form. Then the phase angles (phase shifts) are given as;

$$\varphi = \tan^{-1}\left(\frac{\mathrm{Im}\, H_u}{\mathrm{Re}\, H_u}\right) \tag{4.14}$$

where φ is the phase angle, ImH_u is the imaginary part of H_u, and ReH_u is the real part of H_u. Since the calculation of H_u is given as the ratio of reflected wave to incident wave, it also corresponds to the complex form of the reflection coefficient at the discrete frequency.

To carry out the calculations, the complex forms of incident and reflected waves are needed to calculate the H_u. However, incident and reflected wave spectra, calculated by PCGODA are given as real numbers. The complex forms of incident and reflected waves were obtained by applying a simulation procedure to the incident and reflected wave spectra. The procedure

of reproducing a wave record from the energy spectrum is given in Section 4.1.c. An example is given in the next section to show how phase shifts between the higher harmonics of incident and reflected waves were calculated.

4.1.b.1 PHASE SPECTRUM EXAMPLE

A synthetic incident and a reflected wave record with given wave heights and periods are presented in Table 4.1. The waves are constructed with three different phase lags, $\varphi_1=45^0$ $\varphi_2=30^0$ $\varphi_3=15^0$ between incident and reflected waves for the fundamental frequency, 1^{st} and 2^{nd} harmonics, respectively.

Table 4.1 Incident and reflected wave characteristics used in the example problem

	H_1 (cm)	H_2 (cm)	H_3 (cm)	T_1 (sec)	T_2 (sec)	T_3 (sec)
Incident	10	10	10	6	3	1.5
Reflected	6	6	6	6	3	1.5

The wave record for the given incident and reflected waves is shown in Figure 4.2. Fourier analysis gives the energy spectra for incident and reflected waves shown in Figures 4.3.a and 4.3.b, respectively.

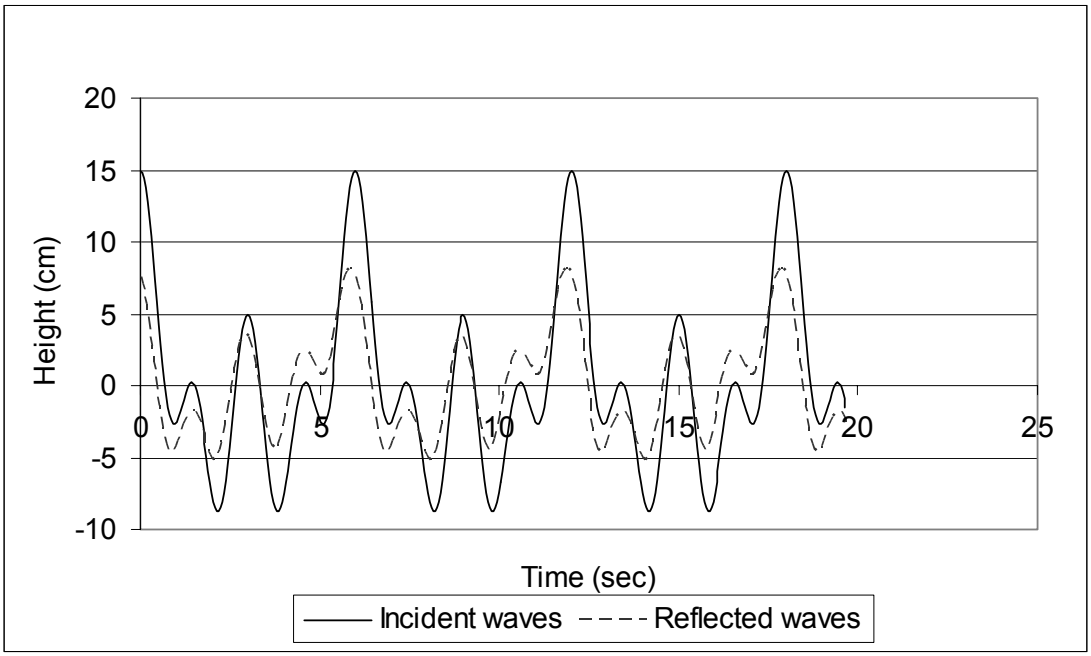

Figure 4.2 Synthetic wave record for incident and reflected waves of example problem.

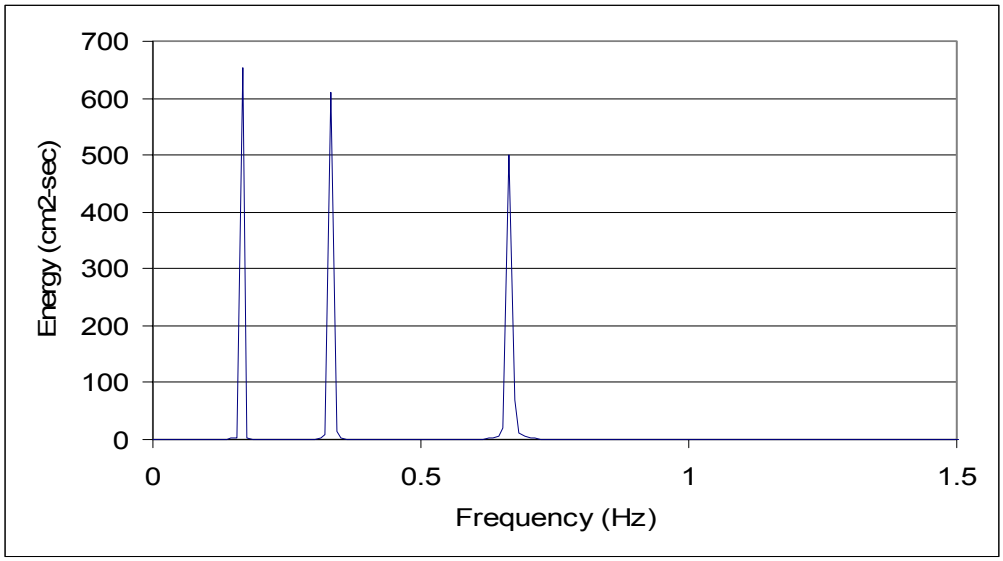

Figure 4.3.a Energy spectrum for incident waves of example problem

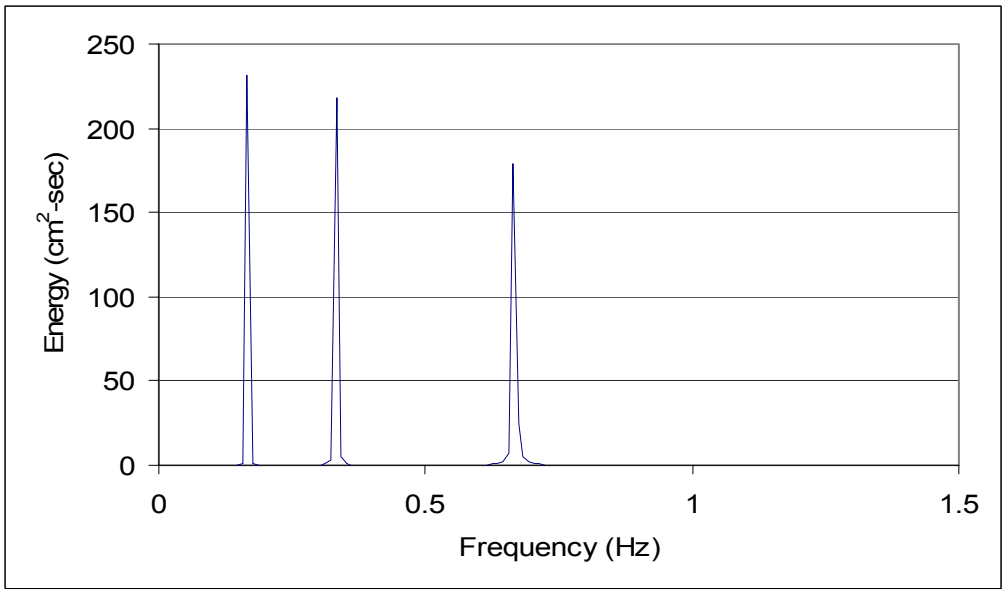

Figure 4.3.b Energy spectrum for reflected waves of example problem

The Fourier analysis gives the complex form of the incident and reflected waves for each frequency which is used to calculate the reflection coefficient, H_u, using Eq. 4.13. Using the imaginary and real parts of H_u, phase shifts for each frequency are calculated by Eq. 4.14. The calculated phase spectrum for the example problem is given in Figure 4.4. An enlarged portion of the phase spectrum with fundamental and 1st and 2nd harmonics is given in Figure 4.5. The fundamental frequency, f_1, = 0.167 Hz, the 1st harmonic, f_2, = 0.333 Hz and the 2nd harmonic, f_3, = 0.667 Hz.

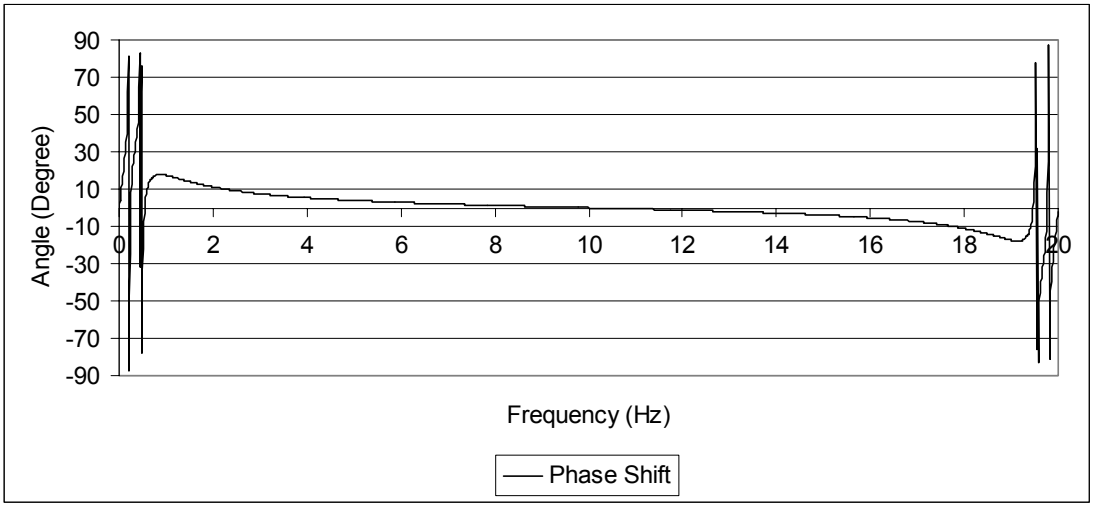

Figure 4.4 Calculated phase spectrum for example problem

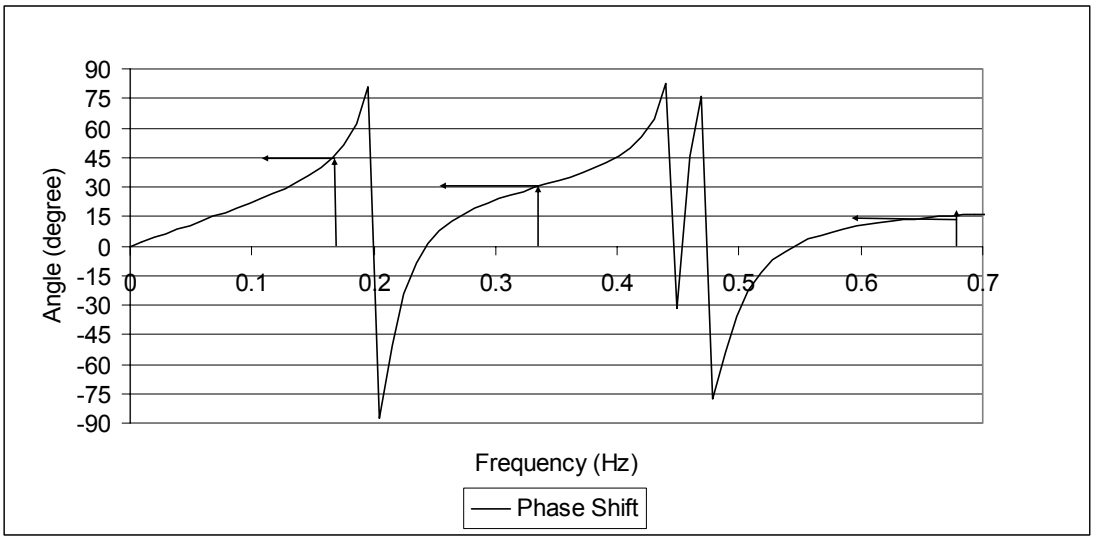

Figure 4.5 Enlarged phase spectrum for example problem with $f_1 = 0.167$ Hz $f_2 = 0.333$ Hz and $f_3 = 0.667$ Hz showing the corresponding phase angles, $\varphi_1 = 45^0$, $\varphi_2 = 30^0$, $\varphi_3 = 15^0$

Figure 4.5 shows that the phase shifts at each frequency coincide with the given phase shifts. The method described in Section 4.1.b was used to calculate phase shifts for the measured incident and reflected waves.

4.1.c REPRODUCTION OF WAVE RECORD FROM ENERGY SPECTRUM

To calculate the phase spectrum, a complex number representation of the reflection coefficient was needed. Incident and reflected wave records were reproduced from the energy spectra obtained from PCGODA. The procedure was adapted from Dean (1980). A discrete energy spectrum concentrated at σ_n can be expressed as;

$$S(\sigma_n)\Delta\sigma = \int_{\sigma_n}^{\sigma_n+\frac{\Delta\sigma}{2}} S(\sigma_n)d\sigma \tag{4.15}$$

The corresponding wave record is given by,

$$f(t) = 2\sum_{n=0}^{N-1}\sqrt{S(\sigma_n)\Delta\sigma}\cos(\sigma_n t - \varepsilon_n) \tag{4.16}$$

where the period of the data series is $T = \frac{2\pi}{\Delta\sigma}$.

4.1.d REFLECTION POINT

A reflection point in this study refers to a point on the beach from which a wave of given frequency appears to be reflected. For a given frequency, a multiple apparent reflection points exist on a profile. They occur at each point when incident and reflected waves have phase differences that are multiples of π Calculations were made to find the reflection point or points where incident waves reflected from the beach. Local wave length and local phase

angles were calculated for small Δx increments across the beach profile. Figure 4.6 shows the reflection point and other terms used in the calculations. Several possible reflection points were calculated and the closest point to the shoreline was taken as the most likely reflection point for each frequency.

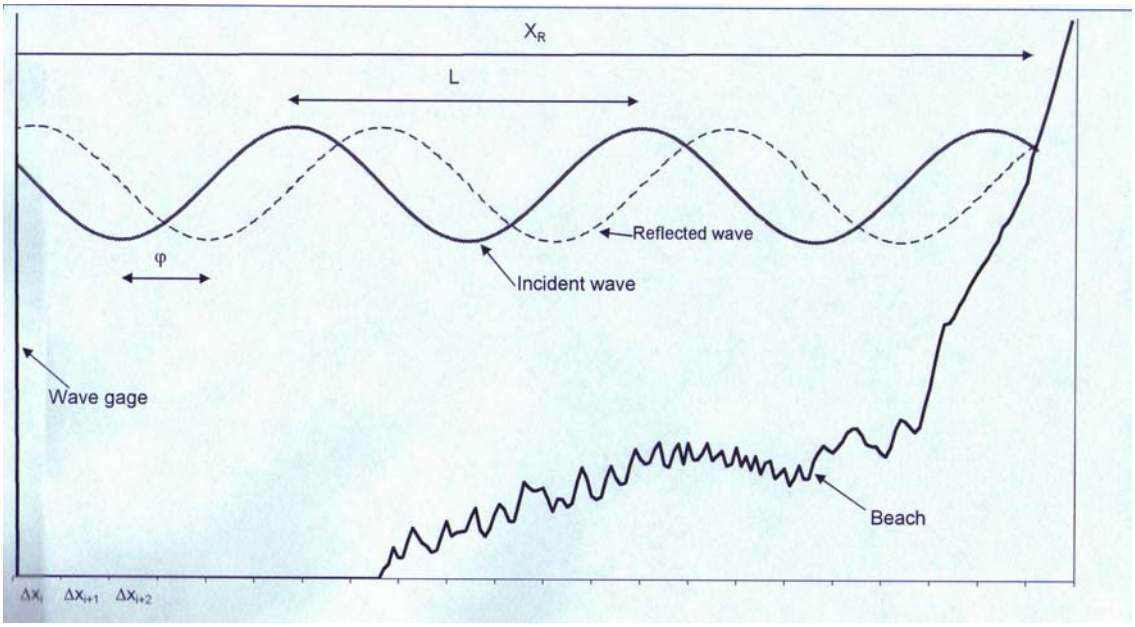

Figure 4.6 Definition of reflection point (X_R), and phase angle (φ) on a beach

The distance from the wave gage to the possible reflection point, l_o, was calculated using the local wavelength and local phase angle according to the following,

$$l_0 = \frac{L_{iavg}}{2}\left(\frac{m}{2} - \frac{\varphi_i}{2\pi}\right) \tag{4.17}$$

where, m is 1, 2, 3…, $L_{i\,avg}$ is averaged local wave length at point i and φ_i is local phase angle in radians. $L_{i\,avg}$ is given by,

$$L_{iavg} = \frac{L_i + L_{i+1}}{2} \tag{4.18}$$

where L_i and L_{i+1} are local wave lengths at points i and i+1 respectively. An apparent reflection point occurs when the phase angle between incident and reflected waves is zero or a multiple of π. Therefore each possible reflection point, X_R, is found for each m value (1, 2, 3,..) when l_o is 0. Local phase angles are calculated by taking the wave gage location as the boundary and the phase angle calculated at gage, φ_0, as the initial phase angle. The local phase angle φ_i at point i, Δx from gage, is calculated by,

$$k_0 x_0 + \varphi_0 = k_1 x_1 + \varphi_1 \tag{4.19.a}$$

where k_0 is wave number at gage, k_1 wave number at point 1, φ_0 phase angle at gage, φ_1 is phase angle at point 1, x_1 is horizontal distance from gage. Calculation of the phase angle at the wave gage, φ_0, is discussed in Section 4.1.b.

Wave number, k, is given by, $k = \frac{2\pi}{L}$, then Eq. 4.19.a becomes,

$$\frac{2\pi x_0}{L_0} + \varphi_0 = \frac{2\pi x_1}{L_1} + \varphi_1 \tag{4.19.b}$$

Since $\Delta x=x_0-x_1$ is an infinitesimal distance, L_0 and L_1 can be averaged to an L_{iavg} and φ_1 is found by,

$$\varphi_1 = \varphi_0 + \frac{2\pi(x_0 - x_1)}{(\frac{L_0 + L_1}{2})} \tag{4.19.c}$$

Then local phase difference at each *i* can be found from,

$$\varphi_i = \varphi_0 + \sum_{i=1}^{N} \frac{4\pi(x_{i-1} - x_i)}{L_{i-1} + L_i} \tag{4.20}$$

To calculate the travel time from the gage to a point on the beach profile, the local wave speed at small Δx increments across the profile was calculated. For adjacent points the average speed was used. Thus,

$$C_{avg} = \frac{C_i + C_{i+1}}{2} \tag{4.21}$$

where C_i = the wave celerity at point i, and C_{avg} = average local wave speed over the interval. The wave celerity at each point was calculated by linear wave theory.

$$\Delta t_i = \frac{\Delta x_i}{C_{avg}} \tag{4.22.a}$$

where Δx = the increment at distance across the beach profile. Time Δt_i is summed to find travel time. Thus,

$$T_N = \sum_i^N \Delta t_i \tag{4.22.b}$$

The distance, X_i, for each cumulative travel time is found by adding Δx to the previous distance.

$$X_N = \sum_i^N \Delta x_i \qquad (4.22.c)$$

Reflection distances were calculated for each harmonic. Figure 4.7 shows the reflection distances measured from the gage for DSTi05 after the profile had reached equilibrium. The lines for each frequency represent the cumulative distance and travel time (X_i and T_i) calculated from Equations 4.22.b and 4.22.c. Points on the lines for l_0 were calculated using Equation 4.17. The gage is at 0 ft and the shoreline is 29.9 ft from the gage for this figure. Assumed reflection points (those points closest to the shoreline) are X_R = 26.62 ft for the fundamental, X_R = 29.49 ft for the 1st harmonic, X_R = 29.43 ft for the 2nd harmonic, and X_R = 29.63 ft for the 3rd harmonic. Reflection points for higher harmonics were generally closer to shore.

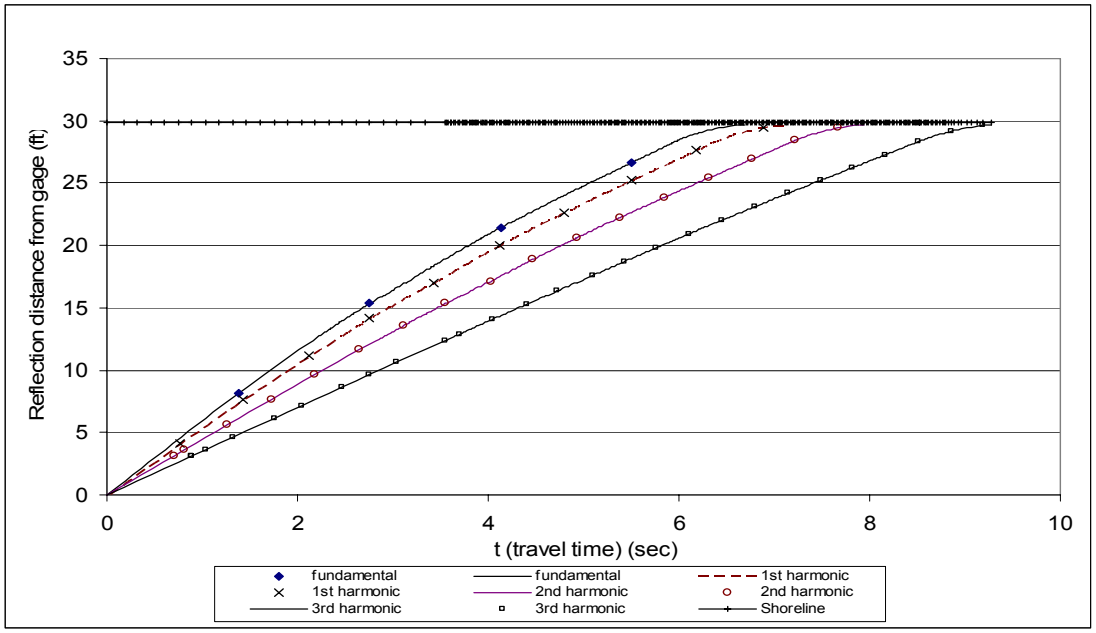

Figure 4.7 Reflection distance calculation for DSTi03 at equilibrium

4.1.e RE-REFLECTED WAVE ANALYSIS

The wave generation system has an active wave absorption system. To investigate its performance energy spectra for waves reflected from the beach and re-reflected from the wave generator after the wave generator ceased producing waves were analyzed. Re-reflected waves are reflected from the beach to the wavemaker and back from the wavemaker to the beach. They are laboratory effects that corrupt the incident waves. In the prototype, waves reflected from a beach are scattered to infinity and do not return to the beach. In the laboratory, they reflect from the wave paddle back to the beach. To investigate re-reflected waves in the present study, a wave record was taken after the wave maker ceased making waves but while the wave absorption capacity was still active. Reflected and re-reflected waves were identified by changes in the wave height as time progressed. A wave record for test DSTI02 is shown in Figure 4.8 for the time after the incident wave signal stopped. The crest of the last incident wave in Figure 4.8 is t = 0. The travel time from wave gage to shore for the incident wave was calculated to be 5.5 seconds. The travel time from wave gage to the wavemaker was calculated to be 4.5 seconds. At t = 10 seconds and at t = 20.3 seconds the wave heights change. At t = 23 seconds in Figure 4.8 a re-reflected wave is seen. The waves for $23.61 < t < 30.8$ second in Figure 4.8 are re-reflected waves. Their spectral energy is given in Figure 4.9.a. The energy spectrum for the incident waves in this test is given in Figure 4.9.b. Comparing Figure 4.9.a with Figure 4.9.b shows that the re-reflected waves exist in the flume; however, they are small and the absorption system performs well.

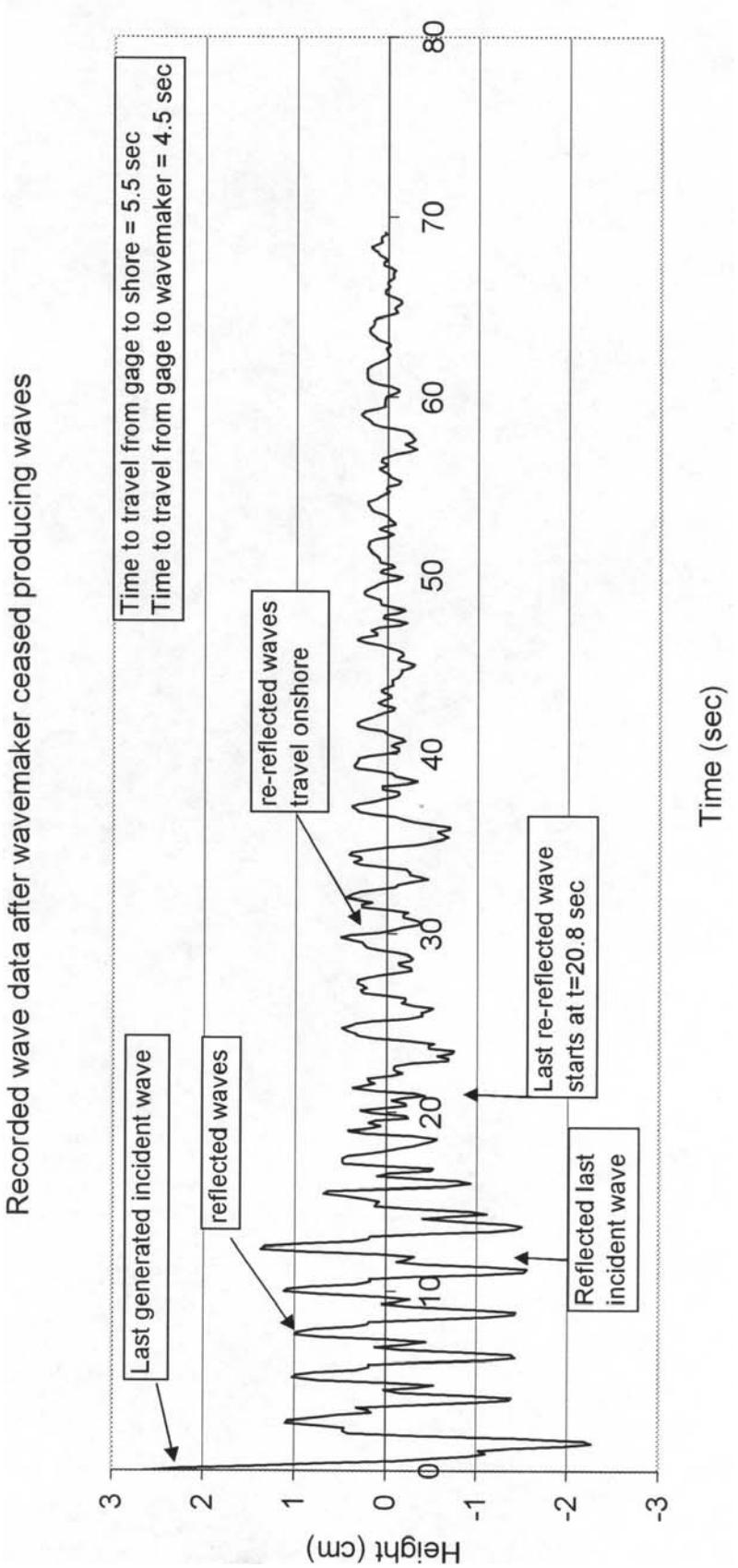

Figure 4.8 Re-reflected wave record

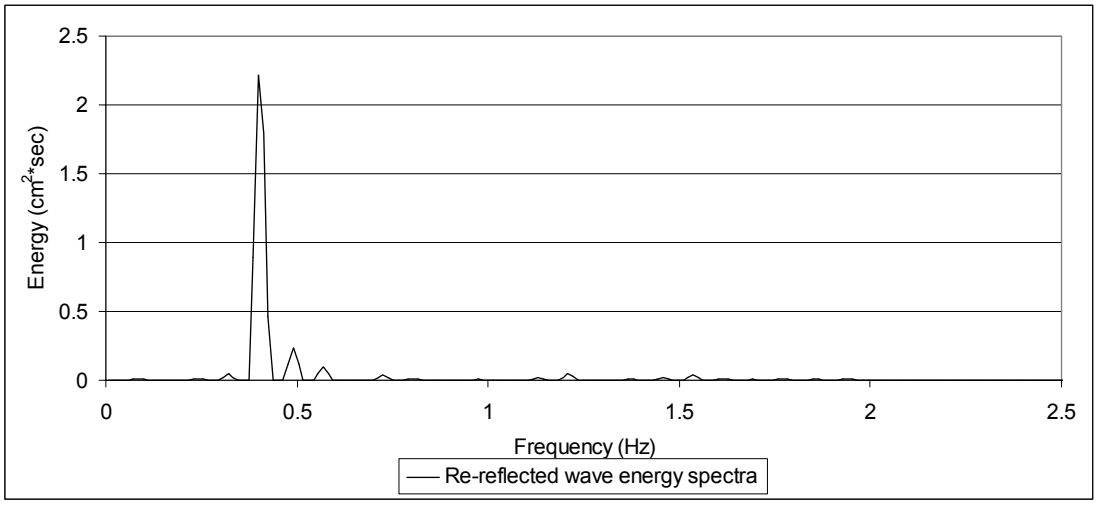

Figure 4.9.a Re-reflected wave energy spectra

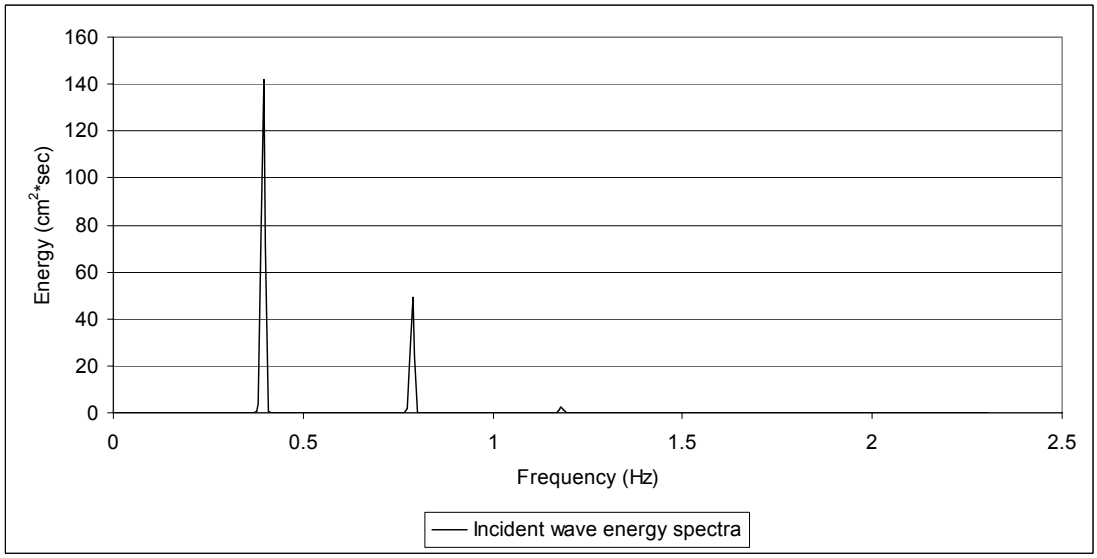

Figure 4.9.b Incident wave energy spectra

4.2. EXPERIMENTAL PROGRAM

This section describes the experimental program and the parameters of the test series. The initial beach profile had an offshore bar. The tests were intended to simulate beach profile recovery or accretion following a storm that had removed material from the beach and deposited it offshore. The initial profile for prototype test STi0 is given in Figure 4.10. Two tests from SUPERTANK (ST10 and STi0) were reproduced at a reduced scale. ST10 was a test of erosive random waves with significant height, Hs = 0.8 m, and modal period T = 3 seconds. A TMA spectrum was used to produce shallow water conditions. Test STi0 was for accretionary, monochromatic waves with H_S = 0.5 m and T = 8 sec. Water depth in the prototype test was 305 cm.

Test ST10 was reproduced at 1:10 scale using the Froude model law. The Drexel reproduction of the test is referred to as DST10 (for Drexel ST10). According to the Froude law, the wave steepness in prototype and model are the same.

$$\frac{H_m}{gT_m^{\,2}} = \frac{H_p}{gT_p^{\,2}} \tag{4.23}$$

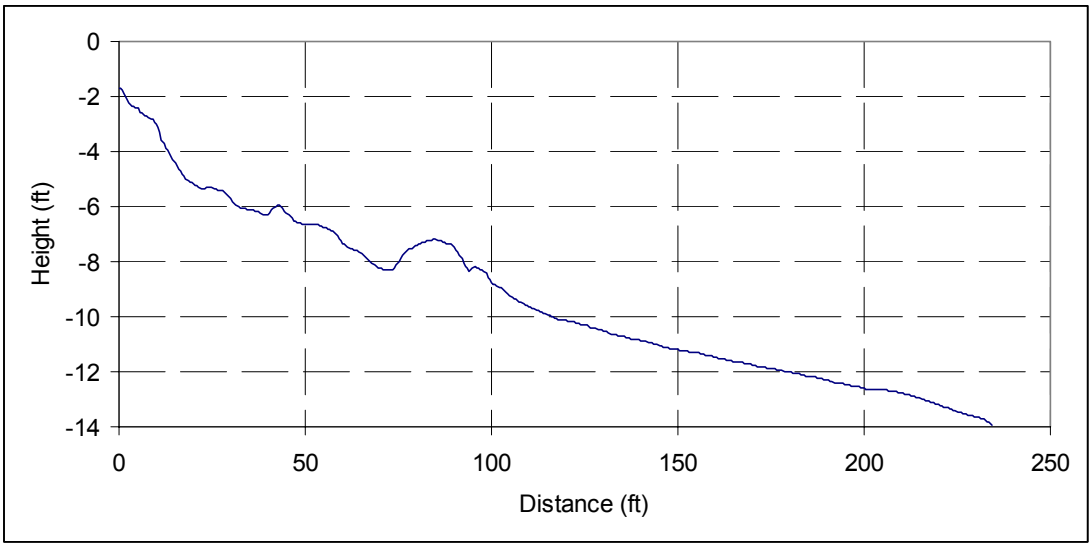

Figure 4.10 Initial beach profile STi0

where the subscripts *m* and *p* refer to model and prototype, respectively, H = wave height and T = wave period. The Ursell number to reproduce ST10 test was less than 25.

The STi0 test was modeled at three scales, 1:10; 1:8.5 and 1:11 with both sinusoidal and cnoidal waves. The same initial profile was used for each test. The modeled tests are designated DSTi01, DSTi02, DSTi03, DSTi04, DSTi05 and DSTi06 with odd numbers designating sinusoidal wave tests and even numbers cnoidal tests. A summary of tests and wave characteristics is given in Table 4.2.

Table 4.2 Summary of wave conditions used in this study

Test	Wave Type	Scale	Wave Height (cm)	Wave period (sec)	Water depth (cm)
ST10 Prototype	TMA Spectrum	1/1	80	3.00	305
STI0 Prototype	Sinusoidal	1/1	50	8.00	305
DST10	TMA Spectrum	1/10	8.00	1.05	33.1
DSTi01	Sinusoidal	1/10	5.00	2.53	33.1
DSTi02	Cnoidal	1/10	5.00	2.53	33.1
DSTi03	Sinusoidal	1/8.5	5.88	2.74	35.85
DSTi04	Cnoidal	1/8.5	5.88	2.74	35.85
DSTi05	Sinusoidal	1/11	4.54	2.41	27.7
DSTi06	Cnoidal	1/11	4.54	2.41	27.7

For the 1:10 scale test the water depth should have been 30.5 cm; however, 33.1 cm was used. Hence, water depths for tests DST10, DSTi01, and DSTi02 corresponded to a 1:9.2 scale, while wave and beach characteristics for those tests were reproduced at 1:10 scale. Also, the peak period for DST10 was calculated as 0.949 sec, but during adjustment of the wavemaker, the period was mistakenly set at 1.05 second (1/0.949=1.05). The impact of the errors on the results of the present analysis is believed to be negligible.

Initial beach profiles were scaled using different horizontal and vertical scales. LeMehaute (1970) suggests scaling horizontal dimensions by the horizontal wave velocity and vertical dimensions by the sediment fall velocity. This leads to the horizontal scale relations,

$$\frac{X_p}{gT_p^{\,2}} = \frac{X_m}{gT_m^{\,2}} \tag{4.24}$$

and the vertical scale relation,

$$\frac{Y_p}{w_p T_p} = \frac{Y_m}{w_m T_m} \tag{4.25}$$

where the subscripts *m* and *p* refer to model and prototype dimensions, respectively; w = the sediment fall velocity; *X* and *Y* = horizontal and vertical profile dimension, respectively. Horizontal dimensions were scaled by Equation 4.24; however, vertical scaling did not follow the fall velocity scaling of Equation 4.25. Equation 4.25 would have required a 4 ft depth in the flume for 1:8.5 scaling, which exceeds the flume's dimensions. Vertical profile dimensions were thus scaled geometrically so that wave height and vertical profile dimensions were reproduced by geometrical scaling.

CHAPTER 5. RESULTS OF ANALYSIS

5.1. WAVE SPECTRA

Wave spectra were calculated using PCGODA which is described in Chapter 2.3.a. Three wave spectra were computed for each run, a combined spectrum including both incident and reflected waves, and separate spectra for each of the incident and reflected waves. The combined spectrum was obtained from the raw wave data. An example combined spectrum for sinusoidal and cnoidal waves is given in Figures 5.1 5.2. The combined spectra are taken from DSTi05 and DSTi06, respectively. The combined spectrum was calculated using three gages located more than ten water depths from the wave maker. This spacing was selected to minimize wavemaker effects. See Figure 3.1.

Incident and reflected waves were separated using Goda and Suzuki's (1976) procedure for two wave-gage pairs. Incident and reflected spectra were obtained using Gages 1 and 2 and Gages 1 and 3. An average incident and reflected wave spectrum was calculated from each gage pair. Thus, 35 spectra were calculated for the seven tests. Their evolution during a test is shown on Figures 5.1 and 5.2 where incident and reflected wave spectra are plotted. The "triangulation with linear interpolation" procedure with SURFER was used to spatially interpolate the data. Figures 5.3 and 5.4 show the incident sinusoidal and cnoidal wave spectra after 150 minutes. The peak incident wave energy is at the fundamental frequency (0.41 Hz) with lower peaks at higher harmonics. Figures 5.3 and 5.4 also show reflected sinusoidal and cnoidal wave energy after 150 minutes. For the reflected waves, for both sinusoidal and cnoidal waves, the peak of the reflected energy was at the first harmonic.

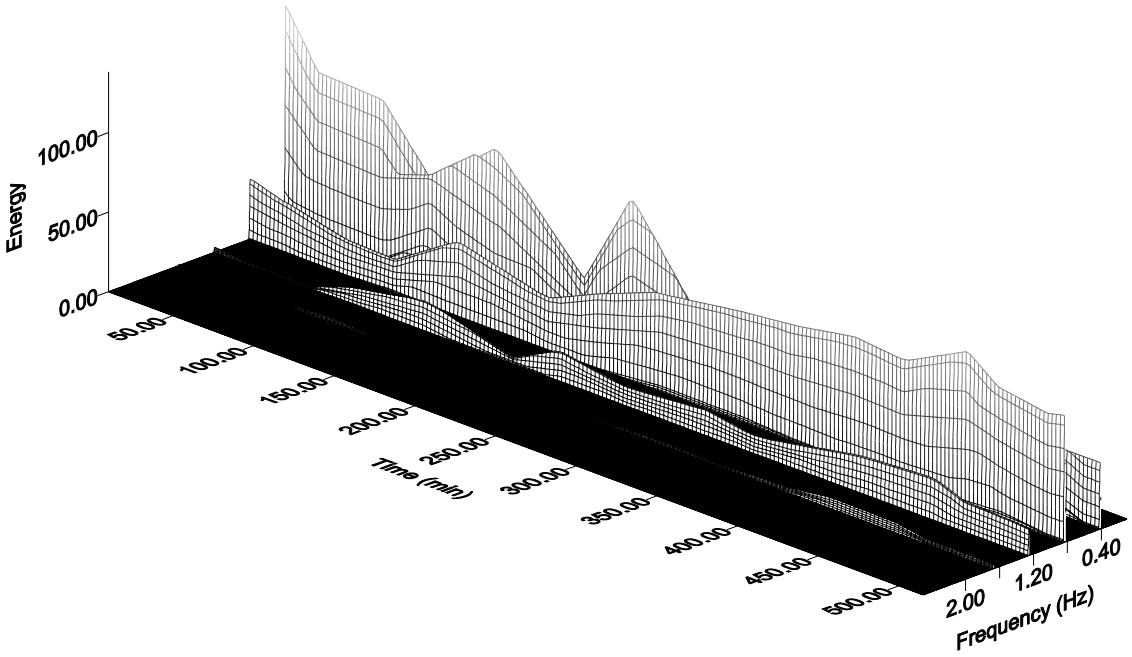

Figure 5.1 Gage 1 Spectra for DSTi05, (sinusoidal waves)

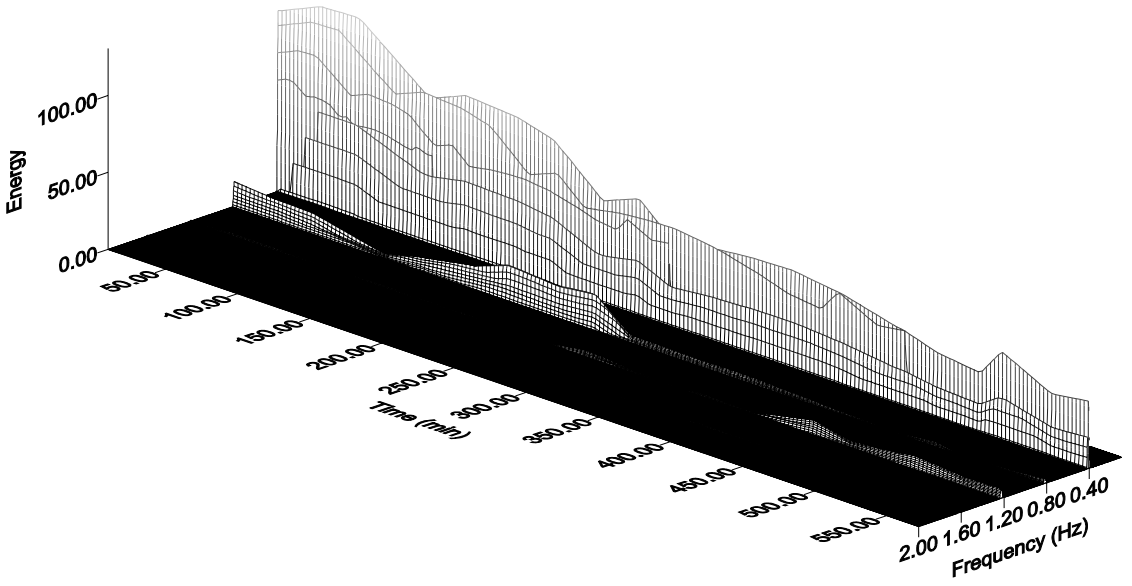

Figure 5.2 Gage 1 Spectra for DSTi06, (cnoidal waves)

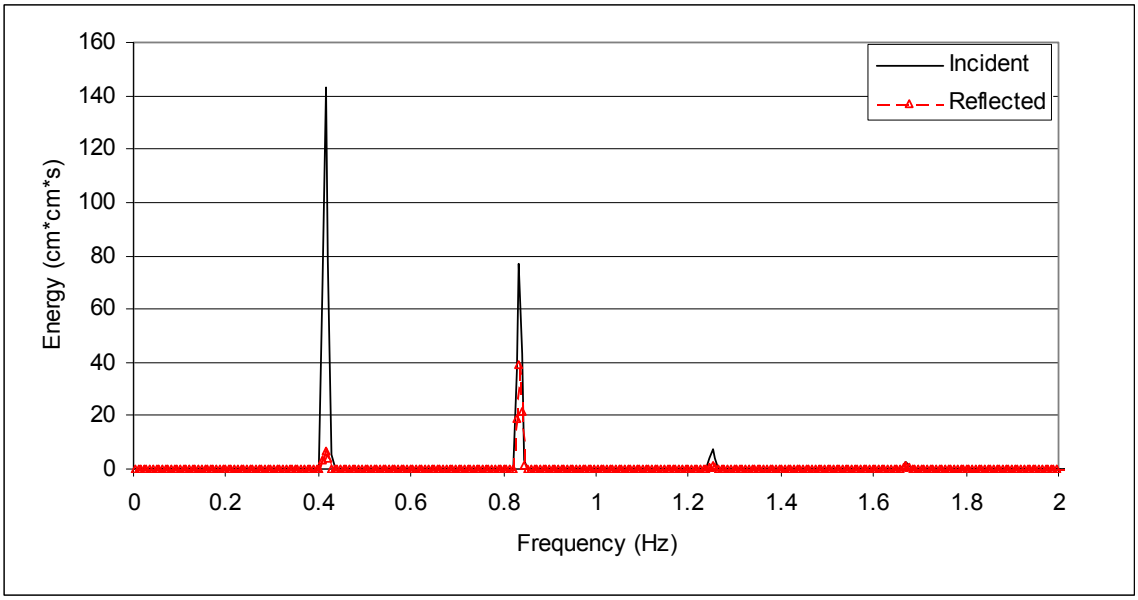

Figure 5.3 Incident and reflected spectra for DSTi05, t = 150 min (sinusoidal wave)

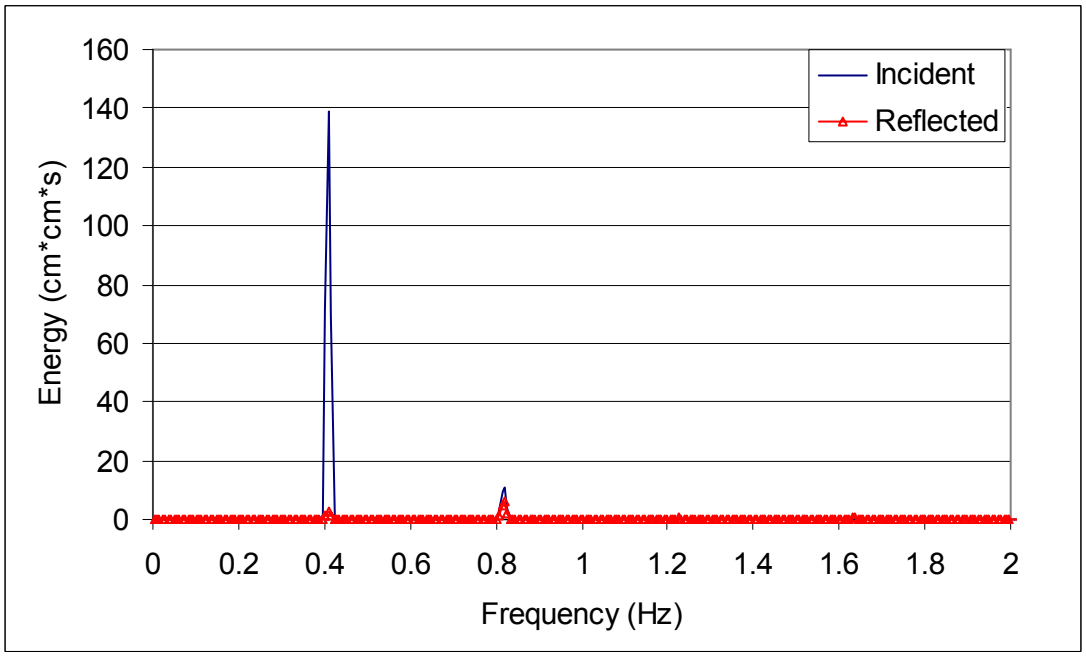

Figure 5.4 Incident and reflected spectra for DSTi06, t = 150 min (cnoidal wave)

Incident and reflected spectra for DSTi05 (sinusoidal waves) are given in Figures 5.5 and 5.6. Incident and reflected spectra for DSTi06 (cnoidal waves) are given in Figures 5.7 and 5.8. These spectra, and a comparison of sinusoidal with cnoidal waves, are discussed below.

Figures 5.3 through 5.6 show the difference between incident and reflected spectra for sinusoidal and cnoidal waves as the profile causing that reflection evolved.

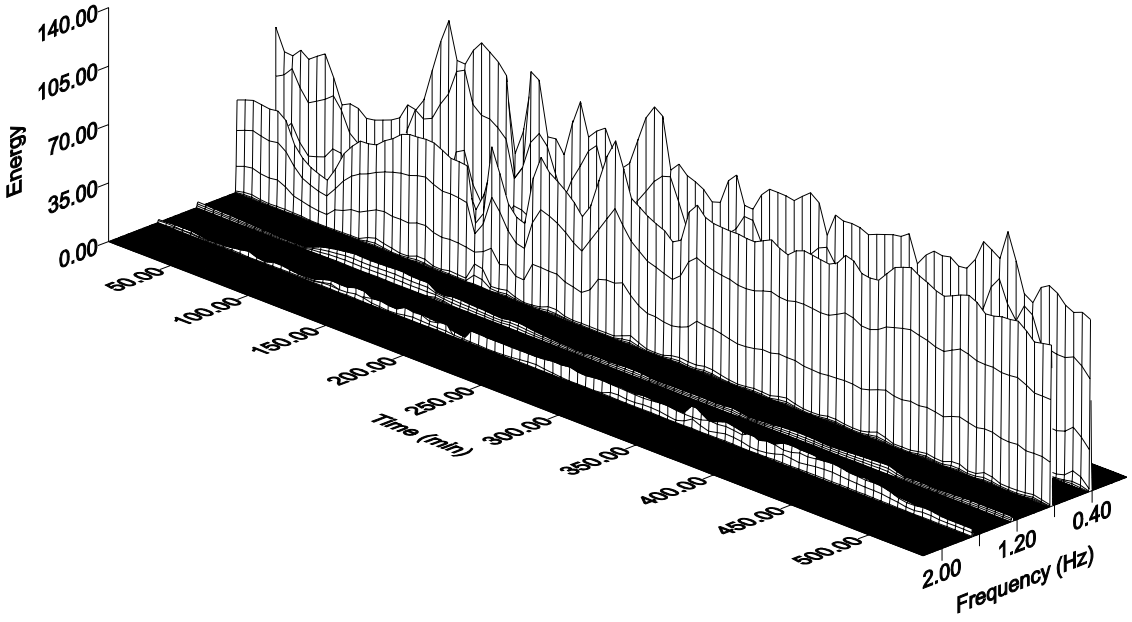

Figure 5.5 Incident wave spectra, DSTi05 (sinusoidal waves)

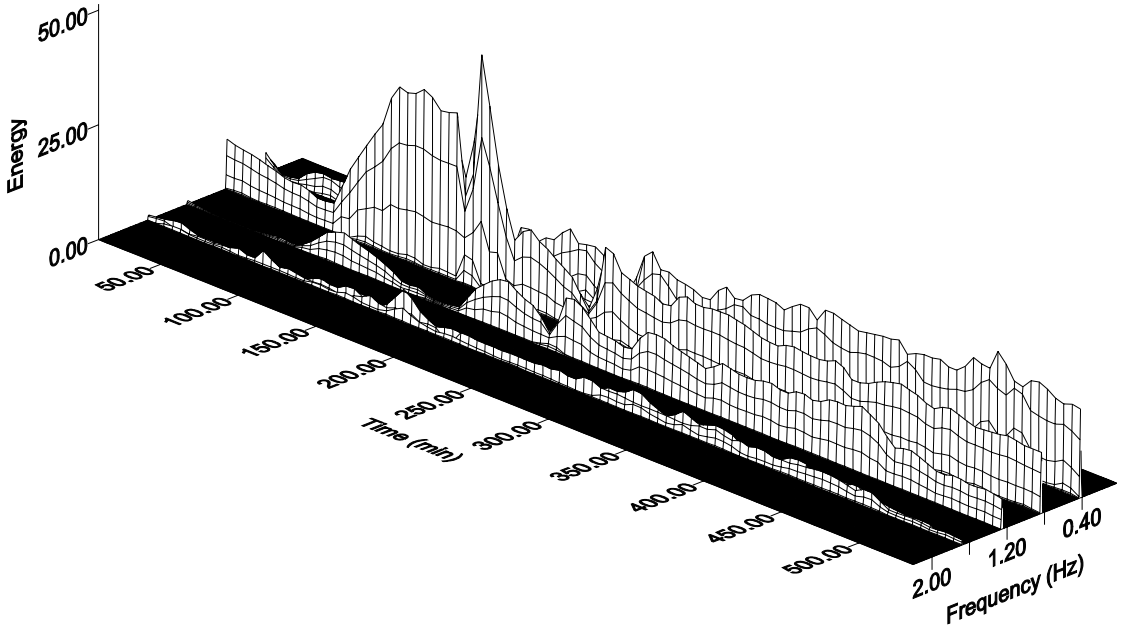

Figure 5.6 Reflected wave spectra, DSTi05 (sinusoidal waves)

5.1.a SINUSOIDAL WAVE SPECTRA

Figures 5.5 and 5.6 show spectra obtained over the duration of DSTi05, the sinusoidal wave test. The fundamental and first harmonic dominated throughout the tests for both reflected and incident waves. The first harmonics were not as pronounced as the fundamental in the DSTI01. Fluctuations in incident wave spectra occurred due to a "start up" effect. Waves at the beginning of each test were slightly larger.

Four harmonics were observed in the reflected sinusoidal wave's spectrum see Figure 5.6. Energy in the reflected fundamental was generally small at the beginning of a test. After about 100 minutes, it began to increase and continued until the end of the test. The reflected first harmonic was almost as large as the fundamental at the beginning of a test. After 100 minutes the first harmonic increased steadily until 160 minutes when it reached its highest value. It then decreased to its starting level about 200 minutes into the test and remained there until the beach reached equilibrium. The second reflected harmonic first appeared when the first harmonic peaked and remained at about the same magnitude until the end of the test.

Sinusoidal wave spectra for both incident and reflected waves showed more energy variation at the beginning of each test. In the reflected spectra, the energy content in the first, second and third harmonics increased during the tests. Higher harmonics of the reflected waves appeared after about 100 minutes, which was about one quarter of the total run time. Higher harmonics appear as the beach profile evolves. See Figure 5.6 for DSTi05 and Appendix E for incident and reflected spectra for all tests.

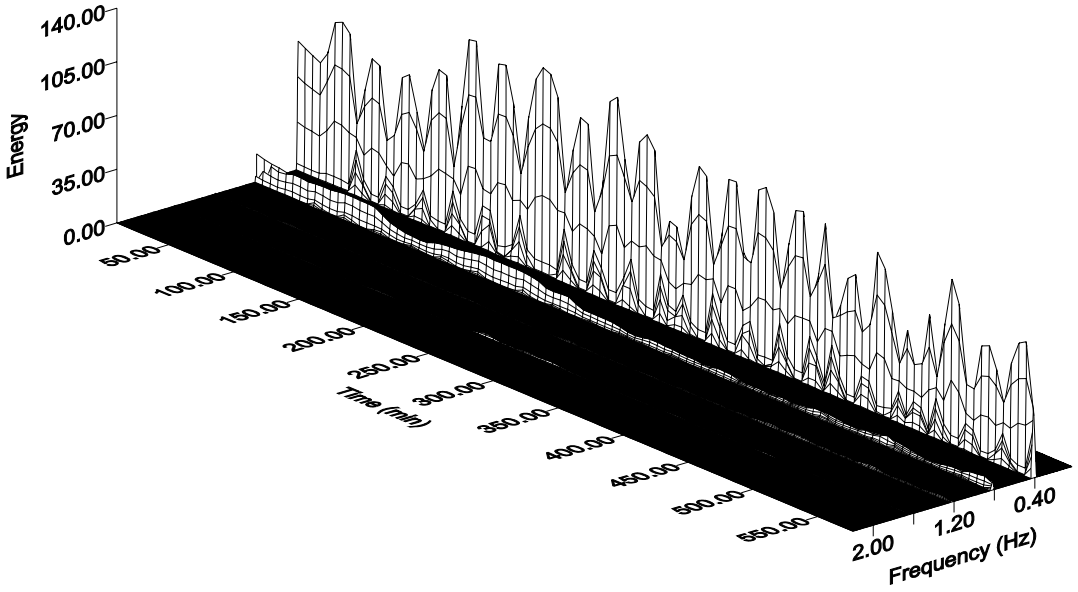

Figure 5.7 Incident wave spectra, DSTI06 (cnoidal waves)

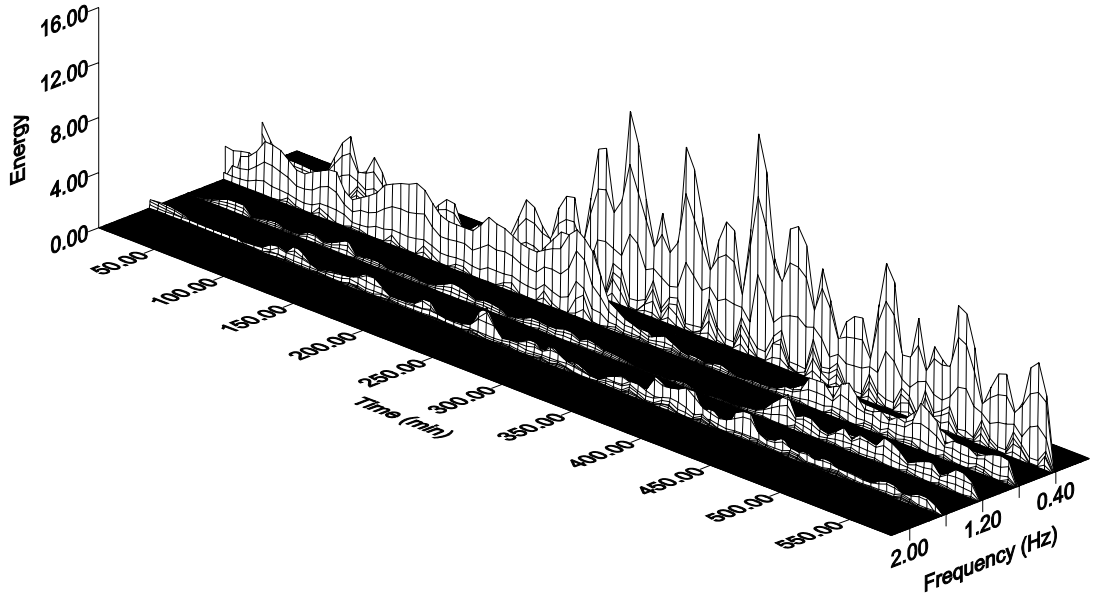

Figure 5.8 Reflected wave spectra, DSTI06 (cnoidal waves)

5.1.b CNOIDAL WAVE SPECTRA

Cnoidal waves behaved differently than sinusoidal waves. Figures 5.7 and 5.8 (Test DSTi06) show incident and reflected spectra. Both the fundamental and first harmonic were present throughout the test. Cnoidal first harmonics were not as large as sinusoidal first harmonics. Figure 5.7, the cnoidal incident spectrum for DSTi06, shows a periodic variation at the start of each run suggesting a "start up" effect. Start up effects occurred for each test; however, the effect was more pronounced for the cnoidal tests. Sinusoidal waves could be run for longer durations than cnoidal waves and so start up effects were less frequent. Cnoidal waves could be run continuously only for 25 minutes since WAVEGEN accepts only 32,000 points which corresponds to 25 minutes of run time.

A reflected cnoidal spectrum for DSTi06 showing fundamental and higher harmonic is given Figure 5.8. Second and third harmonics were always smaller than the fundamental and first harmonic. A steady increase in the fundamental was observed in DSTi02 after the first quarter of the test. The first harmonic was present at the start of each test but decreased as the test progressed. The fundamental increased during cnoidal tests.

The area under each frequency is given for DSTI03 and DSTI04 in Figures 5.9 through 5.12.

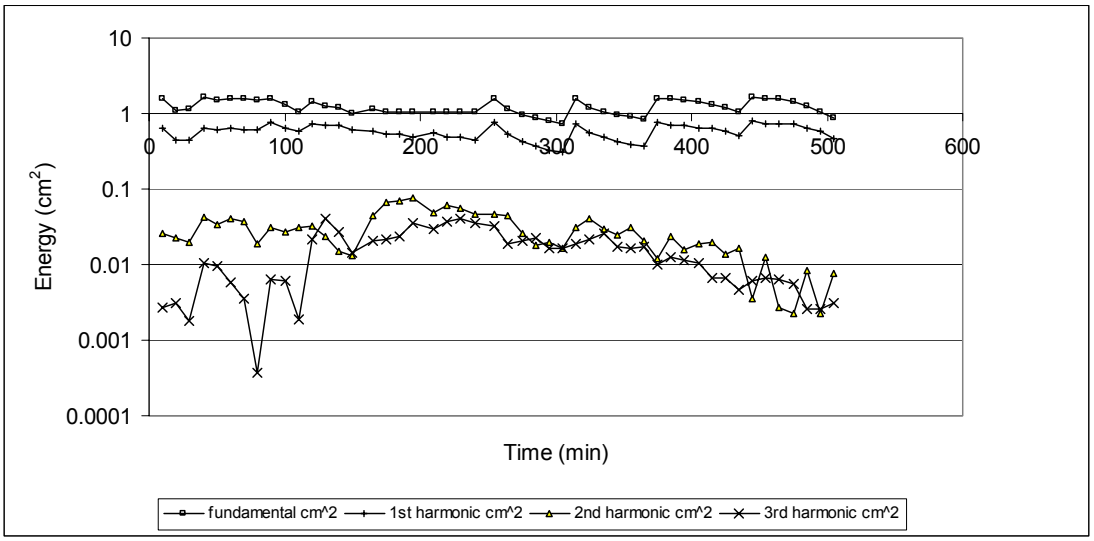

Figure 5.9 Area under incident wave spectra for DSTi03

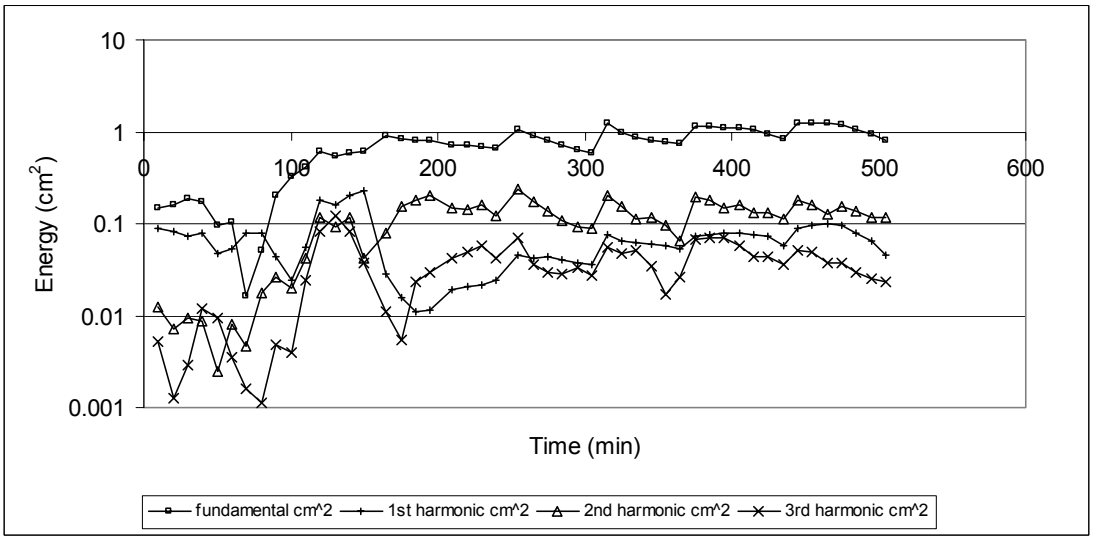

Figure 5.10 Area under reflected wave spectra for DSTi03

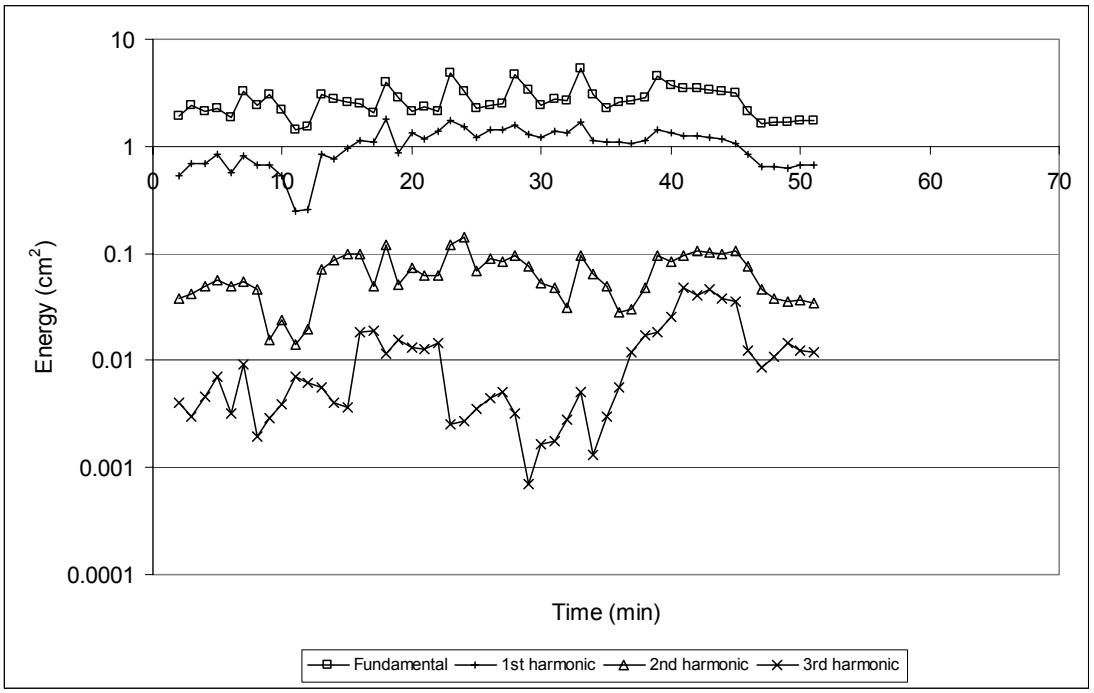

Figure 5.11 Area under incident wave spectra for DSTi04

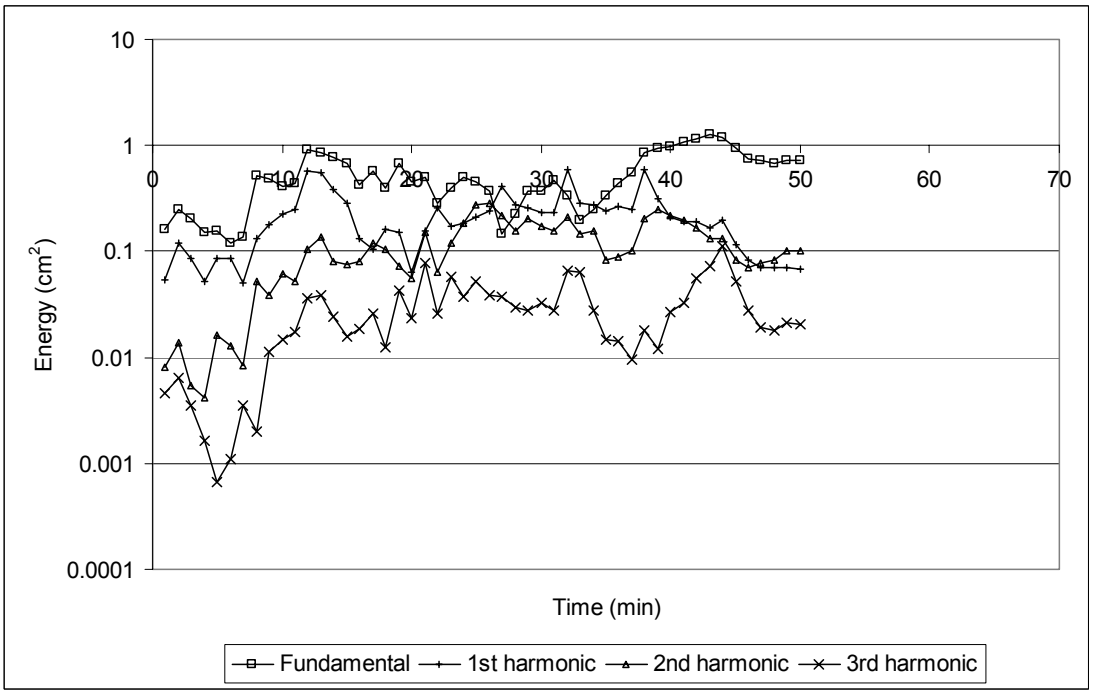

Figure 5.12 Area under reflected wave spectra for DSTi04

In addition, there was an energy transfer from first harmonic to the fundamental in the reflected wave spectra after berm slope was established. See Figure 5.8 for DSTi06 and Figure 5.6 for DSTi05. For reflected waves, energy transfer between 2nd and 3rd harmonics was observed for both sinusoidal and cnoidal waves.

5.2. WAVE REFLECTION

Points on the beach from which wave reflections appear to occur and their relation to beach profile features were investigated. Any irregularity on the profile reflects some wave energy. The amount of reflection and the location of reflection points varied as the profile evolved. Wave reflection coefficients were calculated from,

$$C_R = \frac{H_r}{H_i} \tag{5.1}$$

in which H_i = incident wave height and H_r = reflected wave height. C_R varies from 0 to 1. H_i and H_r were obtained from PCGODA as described in Chapter 2.3.

The reflection coefficient indicates when the beach profile reaches equilibrium. As the profile evolved, the reflection location and amplitude of reflected waves changed. As the profiles approached equilibrium, reflection from the beach increased and approached a constant value. This suggests that the reflection coefficient is an indicator of equilibrium. Reflection coefficients for sinusoidal and cnoidal tests are given in Figures 5.13 and 5.14, respectively.

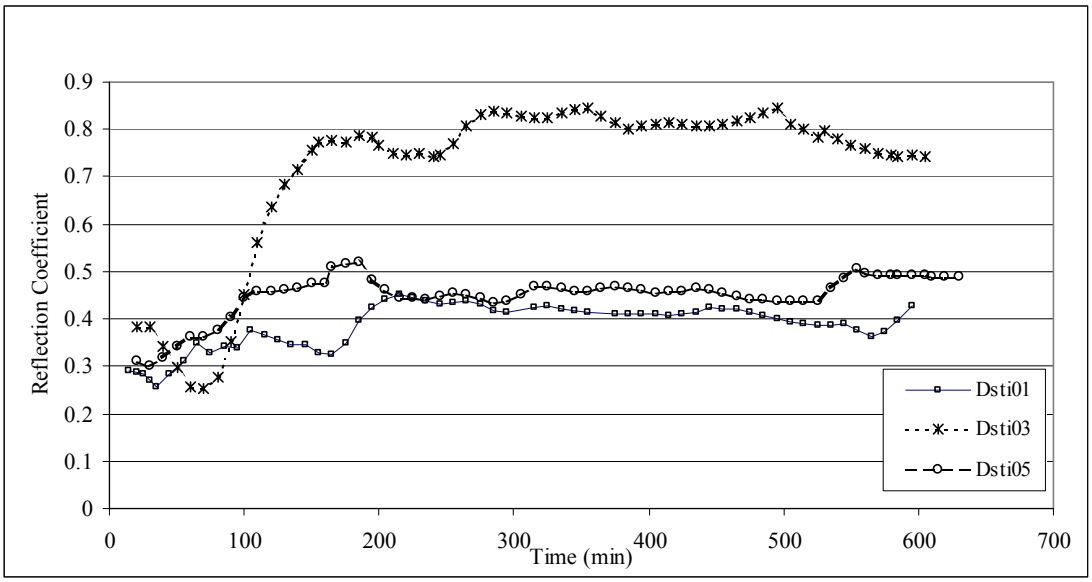

Figure 5.13 Wave reflection coefficients for sinusoidal tests

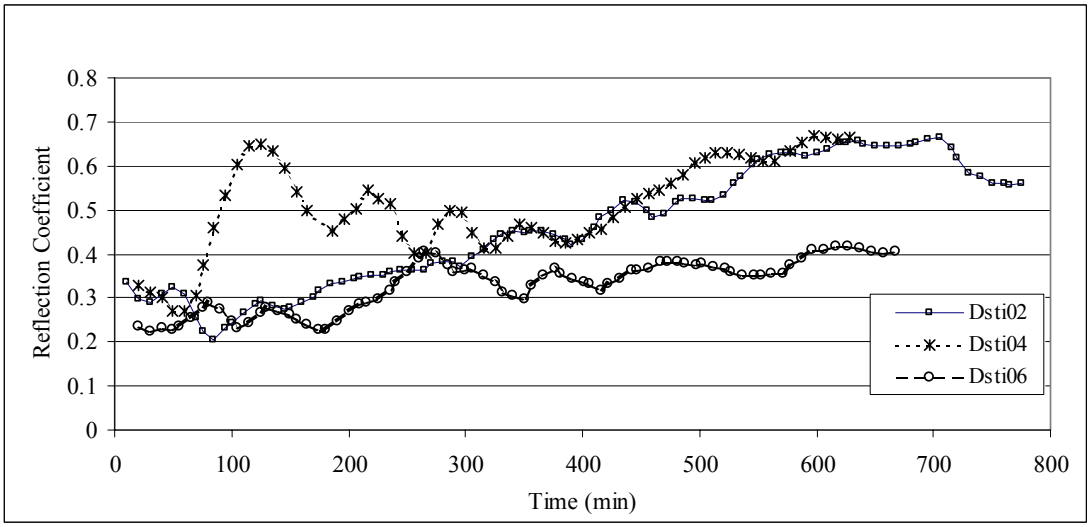

Figure 5.14 Wave reflection coefficients for cnoidal tests

5.2.a SINUSOIDAL WAVE REFLECTION

At the beginning of each sinusoidal wave test, C_R increased rapidly, reached a constant value early in the test, and then remained constant. The berm face on the profile evolved early during tests with sinusoidal waves. Once the berm developed the reflection coefficient remained constant. Profile observations suggest that the constant reflection coefficient was related to the building of the slope of the berm face. When the berm crest was fully established, C_R attained its highest value.

5.2.b CNOIDAL WAVE REFLECTION

In contrast with sinusoidal waves C_R for cnoidal waves continued to increase throughout the tests and became constant only as the profile approached equilibrium. In contrast to sinusoidal waves, the process of building the berm face continued until the end of the tests when equilibrium was finally achieved. Once the berm slope was fully developed, the reflection coefficient was constant. A decrease in C_R was observed when the troughs of offshore bars deepened.

5.2.c COMPARISON OF SINUSOIDAL AND CNOIDAL WAVES

Reflection coefficients were calculated for each harmonic based on the energy under each frequency. Individual reflection coefficients are given in Figure 5.15 for DSTi05 and in Figure 5.16 for DSTi06, for sinusoidal and cnoidal tests, respectively. (Appendix F presents this data for all tests.) Reflection coefficients for both sinusoidal and cnoidal waves for each frequency show the reflection coefficient for the first harmonic to be higher than fundamental in response to profile berm establishment. First harmonic reflection coefficient increases as

the berm crest forms. After the berm crest is established, it decreases and remains constant. However, DSTi01 is an exception.

The role of wave reflection forming bed features was first pointed out by Carter, Liu, and Mei (1973). They found that the reflection coefficient affected the magnitude and direction of mass transport in the bottom boundary layer in a wave flume. They also found that bars could be generated by standing waves and the associated reversal of mass transport in the boundary layer. This caused sand to accumulate at the nodes of the standing wave system. For flow reversal to occur, a significant amount of wave reflection had to occur. They found the magnitude and direction of mass transport velocity to vary with the reflection coefficient. A critical reflection coefficient was $Cr = 0.414$. For $Cr > 0.414$, the mass transport direction was opposite to the incident wave direction. They also found that for $Cr < 0.414$ ripple growth on the bed took place; for higher reflection coefficients, ripples superimposed and coalesced, leading to large bedforms.

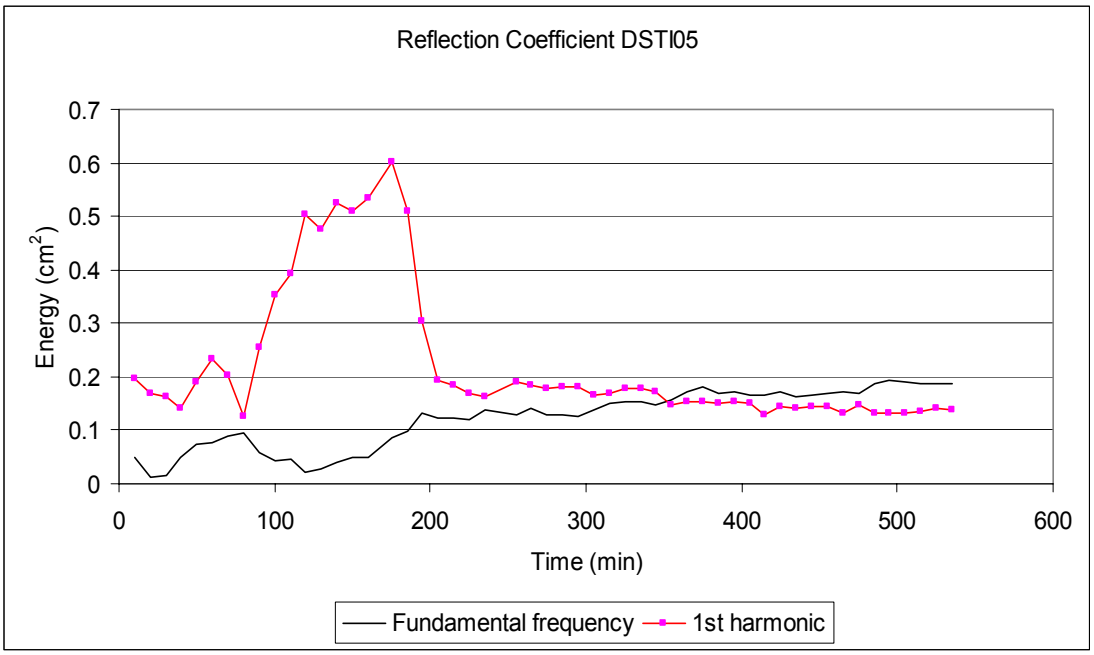

Figure 5.15 Reflection coefficients for fundamental and first harmonic, DSTi05

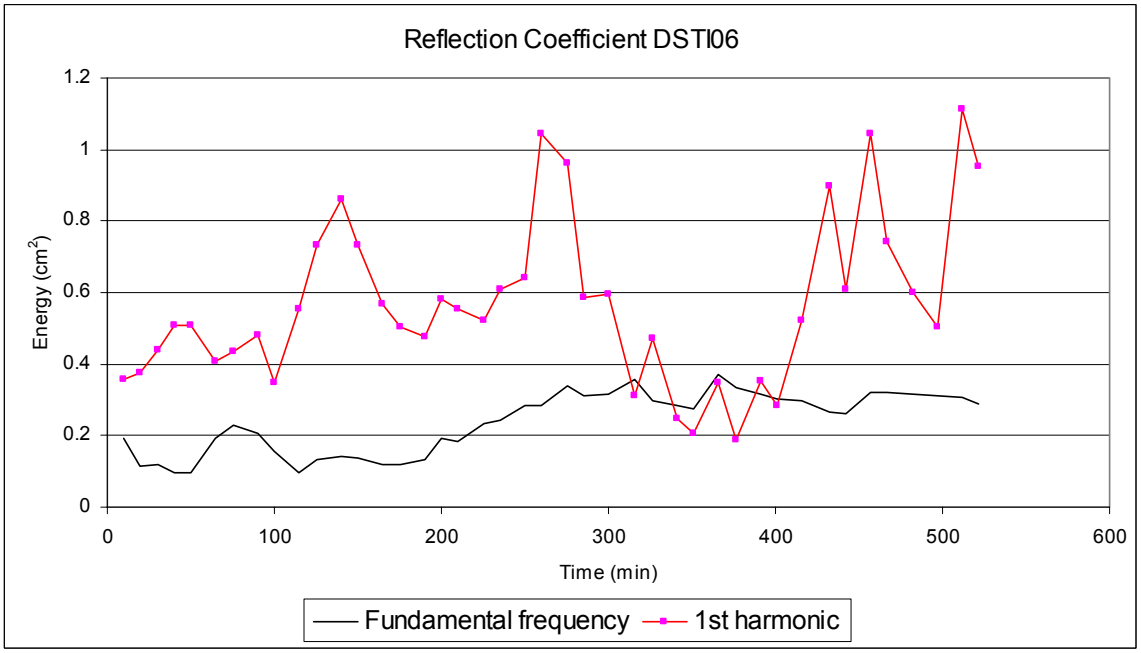

Figure 5.16 Reflection coefficients for fundamental and first harmonic, DSTi06

5.3. REFLECTION POINT

Reflection points were calculated using the procedure described in Chapter 4.1.d. For each fundamental and harmonic, the distance was calculated from the wave gage to the apparent point on the beach from whence each frequency could be reflected. Reflection point calculations are sensitive to the computed phase difference between incident and reflected wave.

5.4. PHASE RELATIONS OF REFLECTED AND INCIDENT WAVES

Calculation of the phase angles between incident and reflected waves is described in Chapter 4.1.b and discussed in Chapter 6.

5.5. CALCULATED BOTTOM VELOCITIES

Cnoidal waves have higher crests and flatter troughs than sinusoidal waves. Crests are shorter in duration than troughs. Bottom velocities under crest and troughs are also significantly different. The asymmetry in wave surface profiles also appears in the horizontal water particle velocities at the bottom. Water particle velocities are higher under crest and of lower under troughs. This asymmetric velocity is important for sediment transport since it is responsible for an imbalance in shoreward and offshore directed transport. Higher onshore velocities generally lead to a net onshore sediment transport.

For a sinusoidal wave, the maximum horizontal bottom velocity is given by,

$$u_{\max} = \frac{\pi H}{T} \frac{1}{\sinh kh} \tag{5.2}$$

in which u_{max} = the water particle velocity, k = wave number, and h = water depth. for cnoidal waves the maximum horizontal bottom velocity under a crest is given by (Dingemans, 1997),

$$u_c^{\,b} = c\frac{a_c}{h+a_c} - \frac{H^2}{4m(h+a_c)^2}\sqrt{gh} \tag{5.3}$$

and the maximum velocity under a trough is given by,

$$u_t^{\,b} = c\frac{a_t}{h-a_t} + \frac{(1-m)H^2}{4m(h-a_t)^2}\sqrt{gh} \tag{5.4}$$

in which, $u_c^{\,b}$ and $u_t^{\,b}$ = the crest and trough bottom velocities, respectively; a_c and a_t = the distance from still water level to the crest and trough, respectively; h = the water depth; H = wave height ($H = a_c + a_t$) ; m is the elliptic modulus, and g = acceleration of gravity.

Bottom velocities were calculated for incident and reflected waves using the appropriate linear or cnoidal theory. Shoaling relationships for sinusoidal waves and cnoidal waves were used to calculate wave heights for both incident and reflected waves. Details are given in Chapter 2. Incident and reflected bottom velocities were added vectorally. Velocities of incident waves under the crest and reflected waves under the trough are both directed onshore. Similarly, incident waves under the trough and reflected waves under the crest are directed offshore. The phase differences between incident and reflected waves were considered in the calculations with the reflected wave bottom velocities under crest and trough are multiplied by the cosine of the local phase difference. (The calculation of local phase differences is discussed in Chapter 4.1.d.)

The onshore-directed bottom velocity was found by adding the incident wave velocity under the crest to the reflected wave velocity under the trough. Similarly, the offshore-directed bottom velocity was found by adding the reflected wave velocity under the crest to the

incident wave velocity under the trough. Sinusoidal velocities and cnoidal velocities for DSTi03 and DSTi04 at selected times are compared in Figures 5.17.a through 5.17.d and Figures 5.18.a through 5.18.d. The critical velocity to initiate sediment transport for the 0.22 mm sand is also shown on the figures. Critical velocities were calculated using Madsen and Grant (1976). Figures 5.17.a through 5.17.d give bottom velocities at selected times for incident and reflected waves for DSTi03 for the fundamental and 1st harmonic. Figures 5.18.a through 5.18.d give bottom velocities for incident and reflected waves at selected times for DSTi04, a cnoidal wave for the fundamental and 1st harmonic. Figures 5.17.d and 5.18.d show that bottom velocities under the cnoidal troughs are smaller than sinusoidal troughs. The bottom velocity under the trough for DSTi04 is directed onshore at the shorewardmost bar at equilibrium. Velocities are maximum at breaking. As the profile approached equilibrium under cnoidal waves bottom velocities decreased. Bottom velocities for all tests are given in Appendix G.

The importance of the bottom velocity in cross-shore transport is described by Ahrens and Hands (2000). They developed a model to predict cross-shore transport based on nonlinear wave theory and showed that sediment movement depends more on near-bottom velocity under the trough than velocity under the crest. Nonlinear waves have higher onshore-directed velocities under their crests and relatively lower (but more persistent), offshore-directed velocities under their troughs. They compared field and laboratory studies and found the profiles to be accretionary when $U_t < 1.8$ regardless of the value of U_c ,where U_t is the ratio of the near bottom velocity under the trough to the critical velocity to initiate sediment movement. U_c is the ratio of the crest bottom velocity to the critical velocity. They state that "although the onshore directed velocity under the crest is greater than the offshore directed velocity under the trough, the offshore directed velocity persists longer and may dominate for

$U_t < 2$". Linear waves however, have the same bottom velocity duration under both crest and trough; hence, U_t is not a good indicator of the sediment transport direction for regular waves.

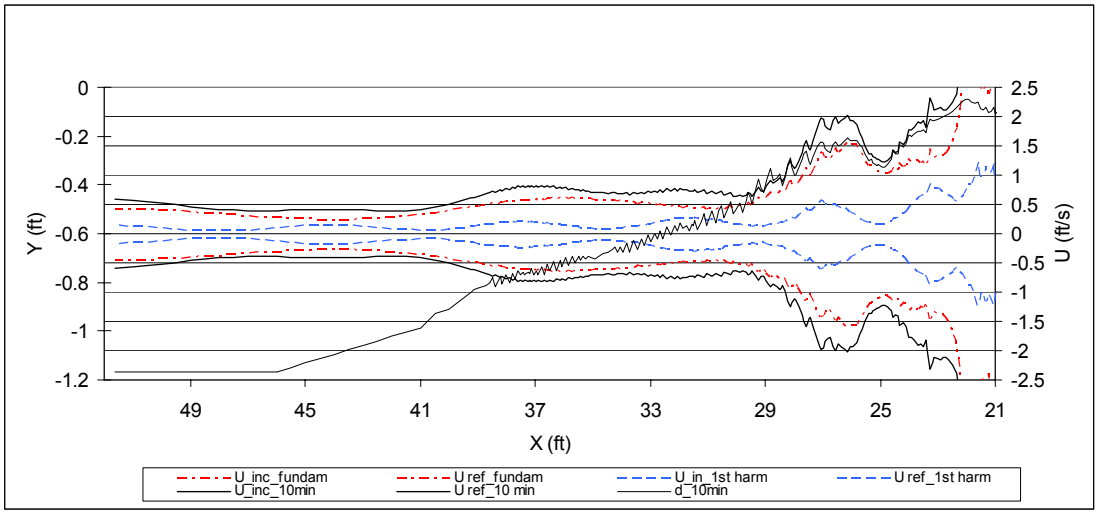

Figure 5.17.a Calculated bottom velocities, DSTi03 at t = 10 min

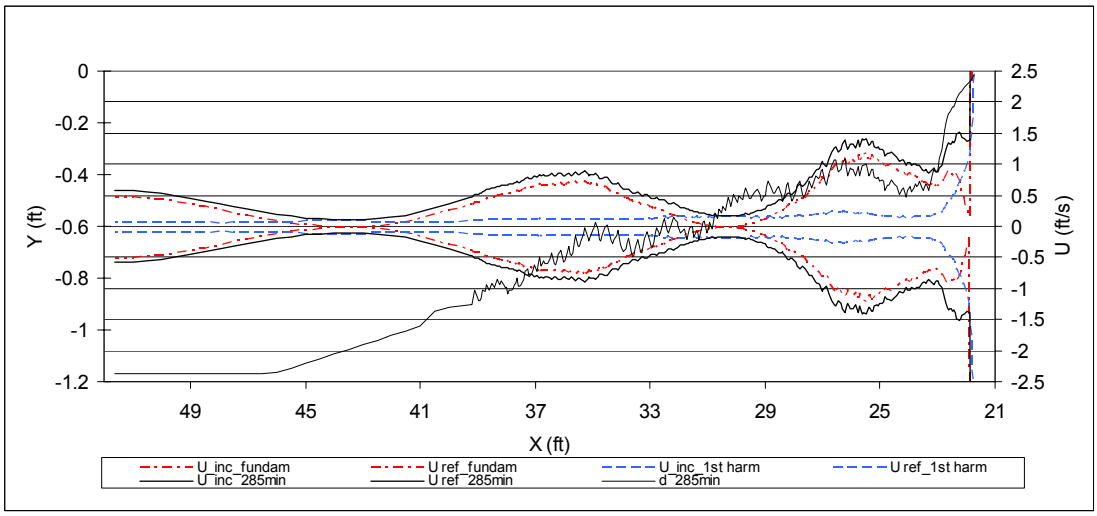

Figure 5.17.b Calculated bottom velocities, DSTi03 at t = 285 min

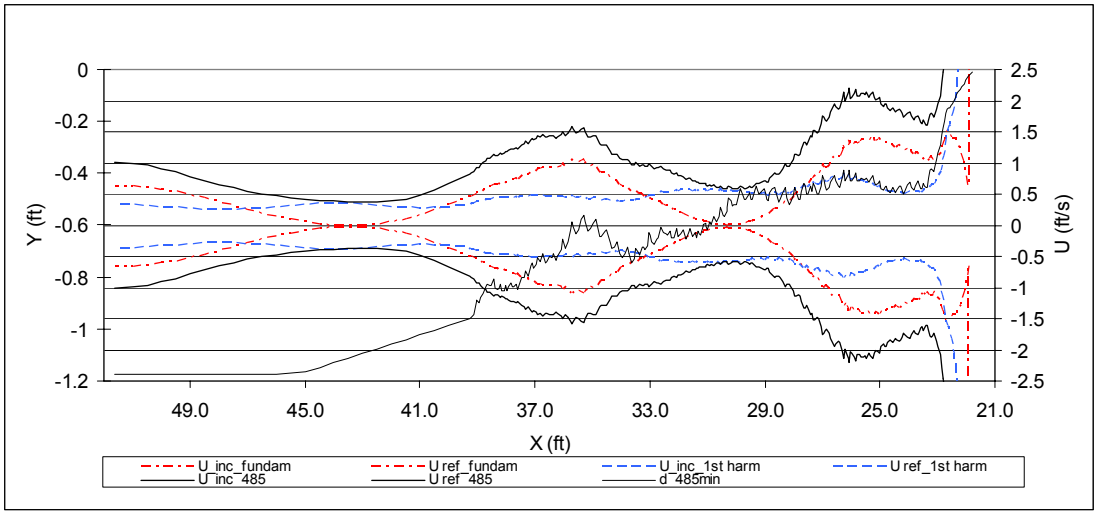

Figure 5.17.c Calculated bottom velocities, DSTi03 at t = 485 min

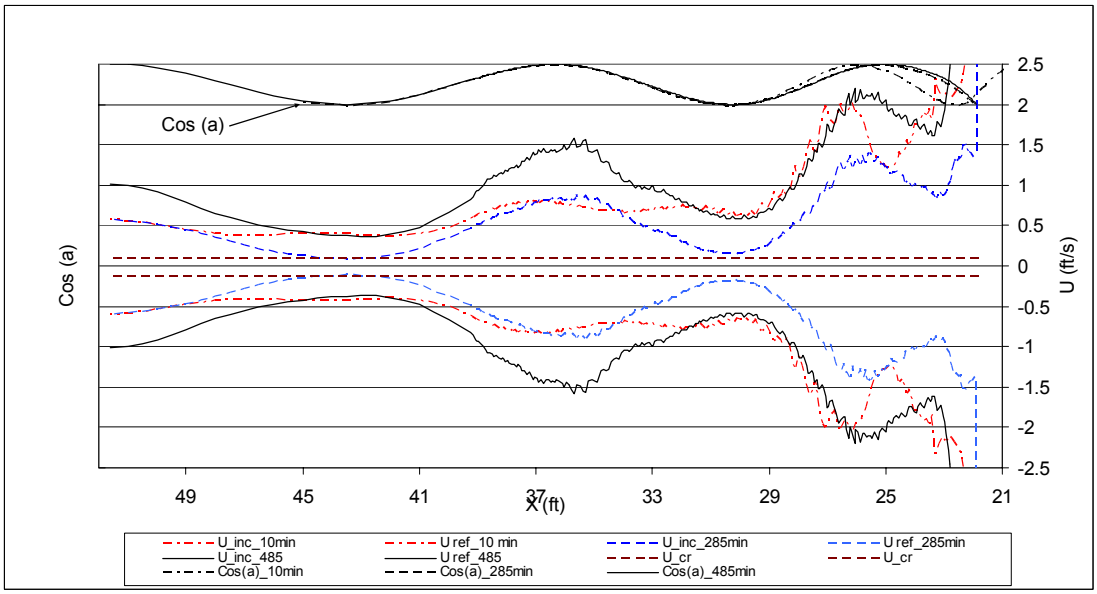

Figure 5.17.d Comparison of calculated bottom velocities and cosine of local phase angles, DSTi03

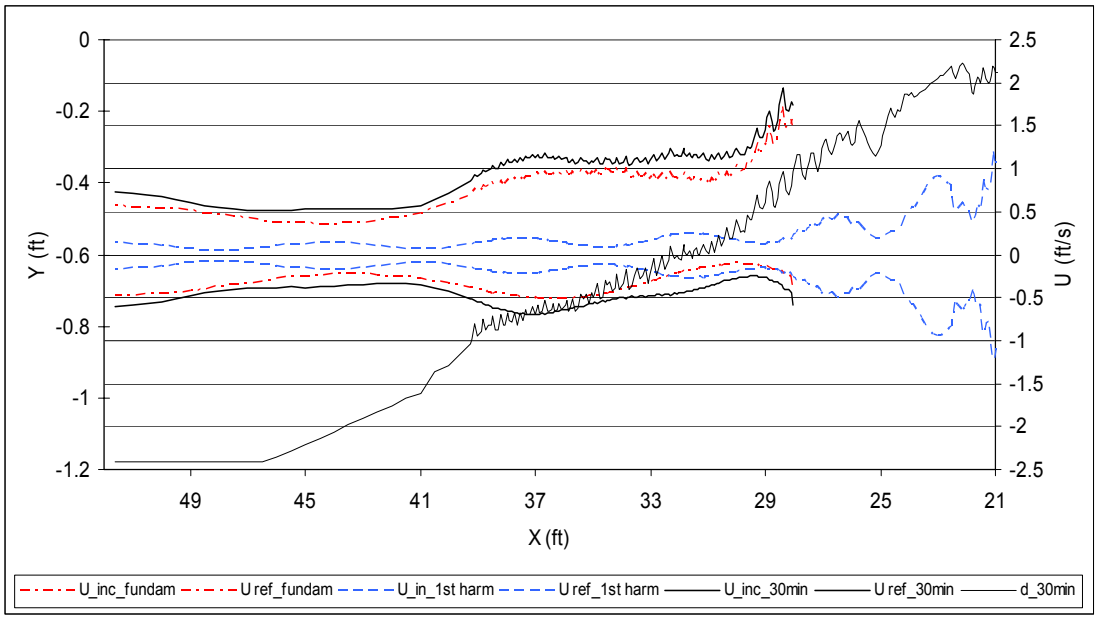

Figure 5.18.a Calculated bottom velocities, DSTi04 at t = 30 min

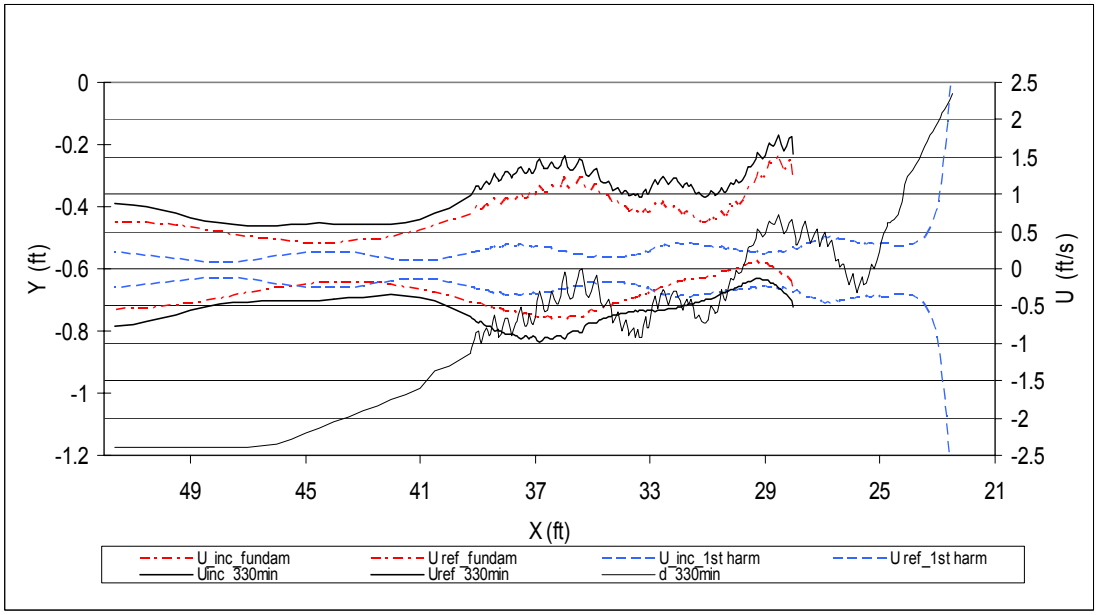

Figure 5.18.b Calculated bottom velocities, DSTi04 at t = 330 min

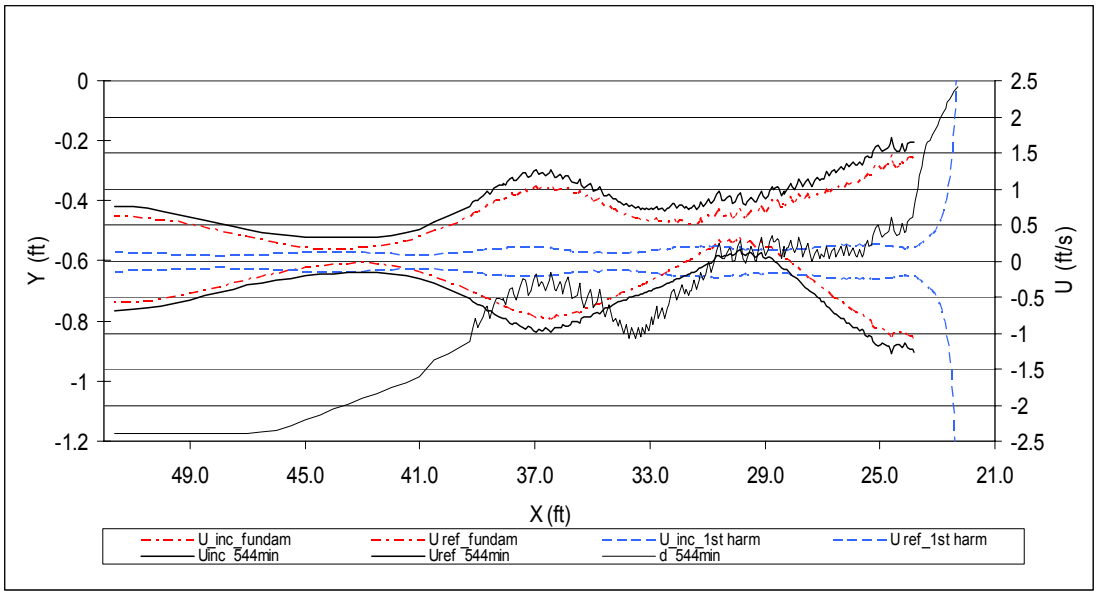

Figure 5.18.c Calculated bottom velocities, DSTi04 at t = 544 min

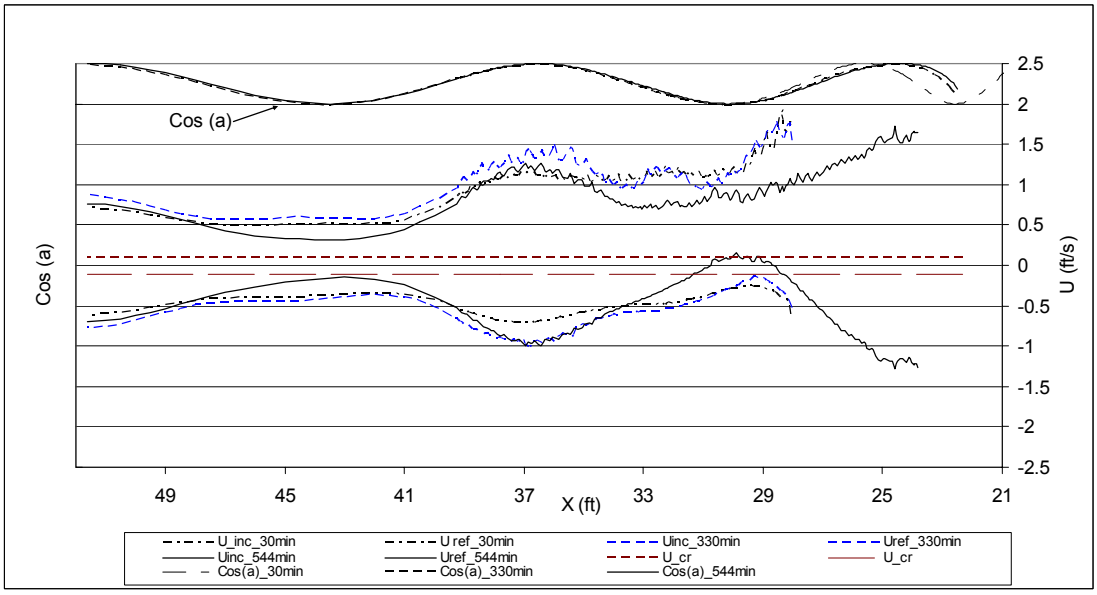

Figure 5.18.d Comparison of calculated bottom velocities and cosine of local phase angle, DSTi04

5.6. BEACH PROFILES vis a vis WAVE CONDITIONS

Tests were run until no significant changes in the beach profile were detected. This was deemed to be the equilibrium profile. By calculating local sediment transport rates across the profile between consecutive profile surveys, equilibrium was defined as when no significant net sediment transport occured and when no change was observed on the profile. A run is defined as a collection of profile surveys for a unique incident wave conditions. A test is a series of runs that describe profile evolution from an initial profile to equilibrium. For example, beach profile evolution of tests DSTI05 and DSTI06 with time is shown in Figures 5.19 and 5.20.

5.6.a EQUILIBRIUM OF WAVES AND BEACH

The wave reflection analysis suggests that the reflection coefficient approaches a constant maximum when the profile reaches equilibrium. For sinusoidal waves, the reflection coefficient was constant after about 180 to 200 minutes - about one third of the total run time. It remained relatively constant until the end of the test. For cnoidal waves, however, reflection coefficients increased steadily throughout a test and reached a constant value only near the end of a test.

A correlation between the increase in reflection coefficient and berm establishment and foreshore slope was found when comparing beach profile evolution with reflection coefficients. The reflection coefficient increased until the berm crest and foreshore slope were established. For sinusoidal waves, the berm crest and foreshore slope were established after about 200 to 250 minutes. For cnoidal waves this occurred only in a test only as the profile approached equilibrium. This difference in behavior explains the observed difference in

beach evolution: Under sinusoidal waves, the beach profile first changed nearshore, the berm crest grew and the foreshore slope developed. Later, multiple bars developed offshore. Under cnoidal waves, the beach profile changed across the entire profile throughout a test. Beach slope and berm became fully established only toward the end. Thus, the cnoidal wave reflection coefficients increased steadily during a test and reached an equilibrium only toward the end.

With the exeption of DSTi02, it also took longer for the beach to reach equilibrium under cnoidal waves. (Toward the end of DSTI02, the geotextile underlying the beach structure was exposed in the beach scarp area between the wave break point and the beach face. The test was terminated before it reached equilibrium although it was believed to be close to equilibrium.)

Berm overwash was high at the beginning of each test and decreased toward the end. Because of overwash, a pool of water existed behind the berm for much of the time. Overwash ceased and the pooled water disappeared as the beach reached equilibrium.

Wave breaking patterns were also observed and noted throughout the tests. Plunging waves were observed for both sinusoidal and cnoidal waves from the start to near the end of all tests. However, as the profile approached equilibrium, breaker type changed from plunging to surging. Surging waves are indicator of high wave reflection and steep beaches.

Ripples formed shortly after the start of each test. They started on different parts of the profile. Observations on ripples are in Appendix H.

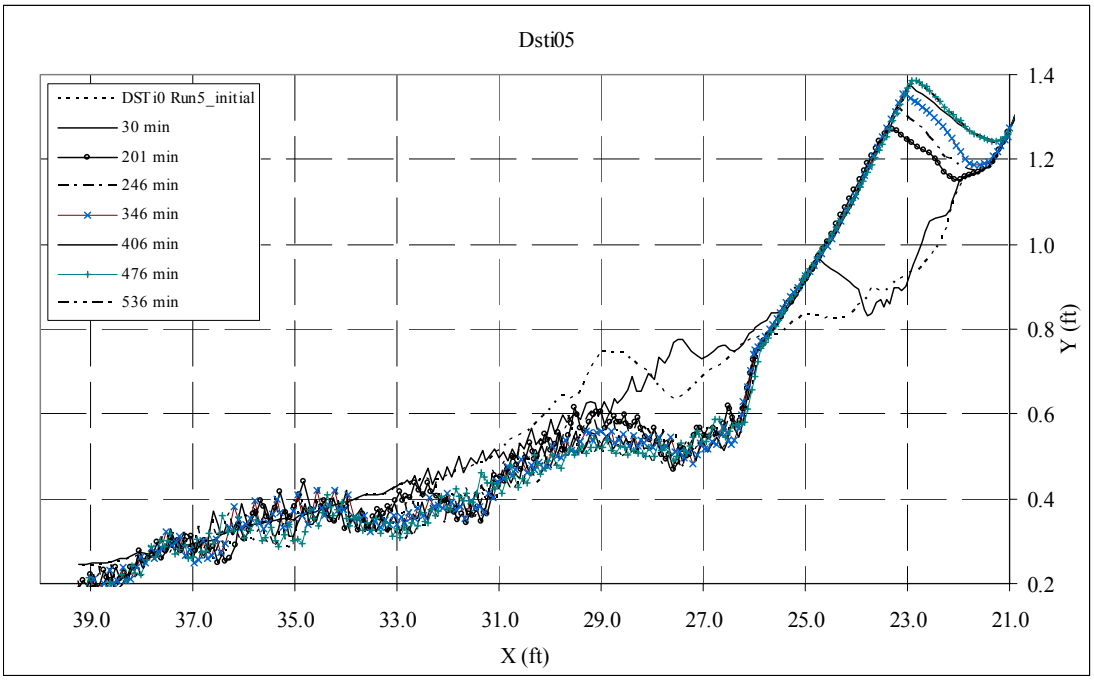

Figure 5.19 Beach profile evolution, DSTi05

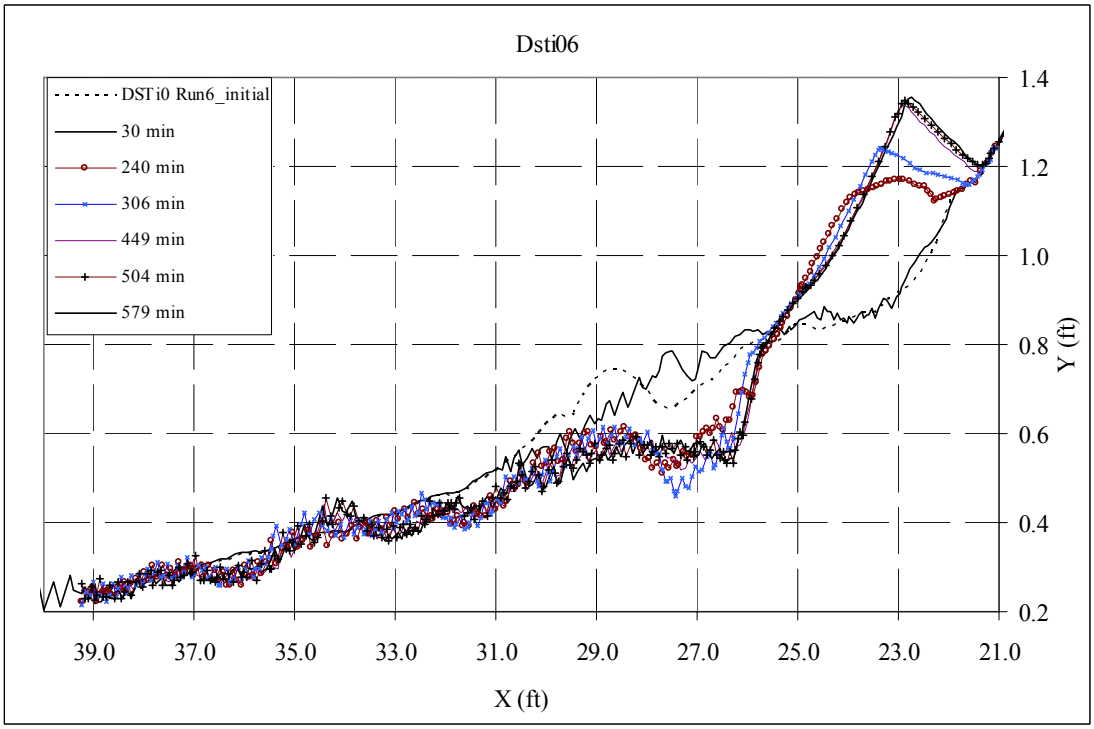

Figure 5.20 Beach profile evolution, DSTi06

CHAPTER 6. DISCUSSION OF RESULTS

Observations made during the tests and their physical interpretations are presented here. The SUPERTANK test, STi0 and the corresponding tests at 1:10, 1:8.5 and 1:11 scale are compared. Discussion is focused on the differences in: beach profile evolution under cnoidal and sinusoidal waves, reflection coefficients, phase angles between incident and reflected waves, apparent reflection points on the profile, and calculated bottom velocities.

Beach profiles resulting from sinusoidal and cnoidal waves are given in Figures 6.1 through 6.3. The figures show the differences in profile evolution under sinusoidal and cnoidal waves. Each figure shows the profiles at the same elapsed time. The initial profile for all tests was a barred profile. Both sinusoidal and cnoidal waves flattened the profile by removing the bar. Sinusoidal waves acted sequentially on different parts of the beach profile. Changes were first observed onshore as berm building and after the berm crest was established, offshore bars grew. Under cnoidal waves changes were observed across the entire profile simultaneously.

With sinusoidal waves, the berm first built and the foreshore slope established itself. Changes on the other parts of the profile then occurred. Standing waves developed and multiple bars formed. The times when standing waves were first observed are given in Table 6.1.

Table 6.1 Time when nodal points appeared and total time of the tests

Test	Wave Type	Scale	*H/L*	*U*	T_N (min)	$T_{DURATION}$ (min)
DSTi01	Sinusoidal	1/10	0.01136	26.69	100	578
DSTi02	Cnoidal	1/10	0.01116	27.67	156	718
DSTi03	Sinusoidal	1/8.5	0.01181	31.65	50	506
DSTi04	Cnoidal	1/8.5	0.01160	32.80	88	638
DSTi05	Sinusoidal	1/11	0.01181	31.70	85	536
DSTi06	Cnoidal	1/11	0.01162	32.69	106	579

T_N = time when nodal points appear, $T_{DURATION}$ = total duration of test, U = Ursell number and H/L = wave steepness.

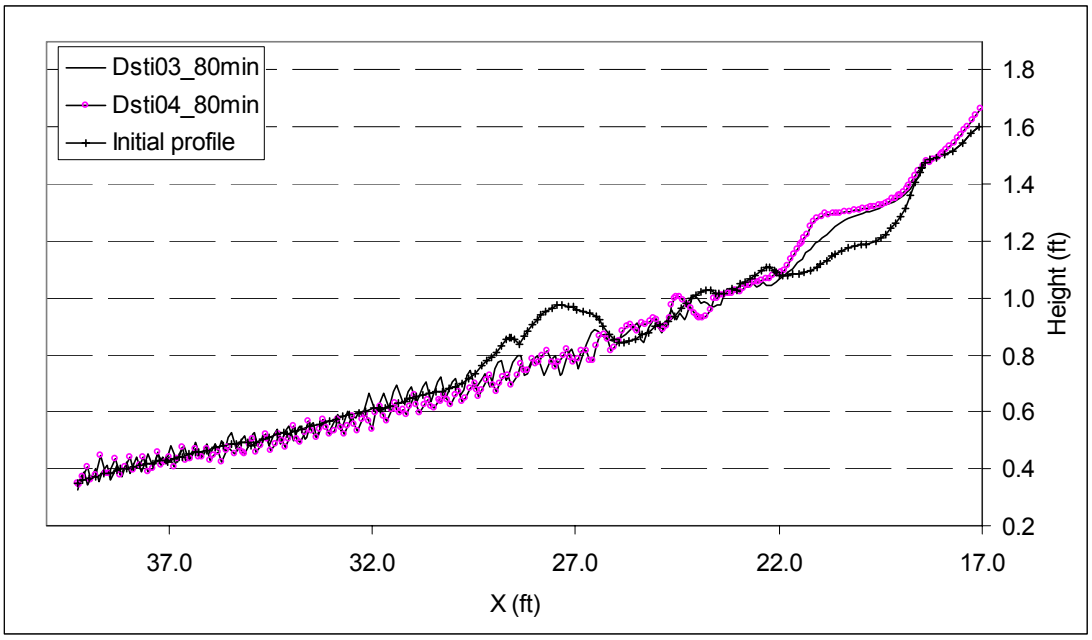

Figure 6.1 Beach profiles under sinusoidal and cnoidal waves at t = 80 minutes

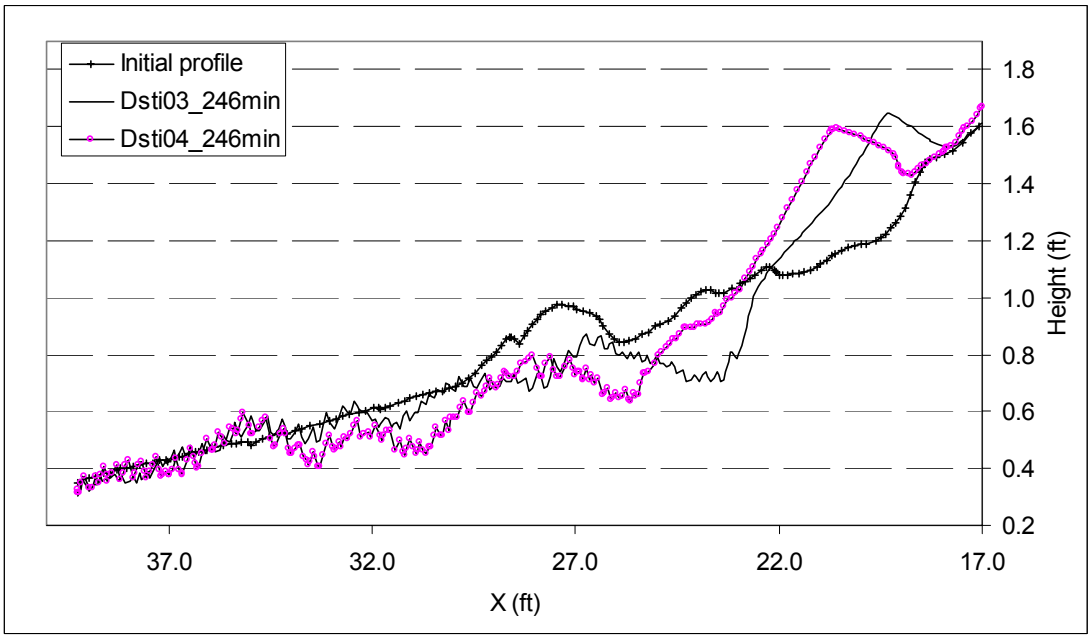

Figure 6.2 Beach profiles under sinusoidal and cnoidal waves at t = 246 minutes

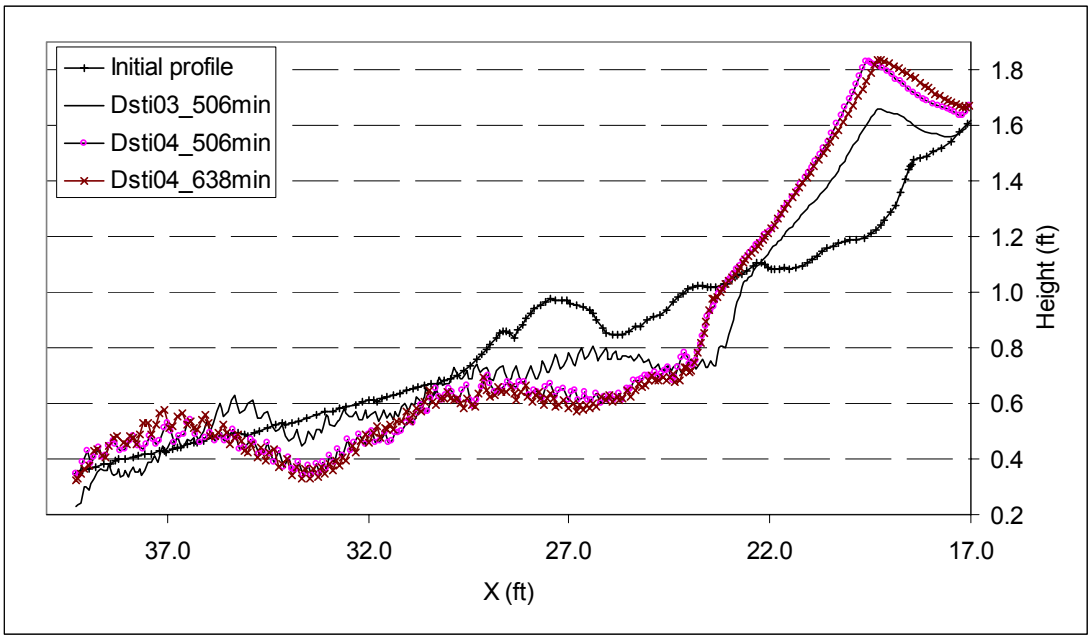

Figure 6.3 Beach profiles under sinusoidal (DSTi03) and cnoidal (DSTi04) waves at equilibrium

Beach profiles under sinusoidal and cnoidal waves are compared in Figures 6.1 through 6.3 for DSTi03 (sinusoidal waves) and DSTi04 (cnoidal waves). The results for other tests are given in Appendix I.

Multiple bars developed on the profile. Under cnoidal waves, bars formed on onshore part of the profile as shown in Figure 6.2. The offshore profile deepened and multiple bars formed. Under sinusoidal waves, multiple bars formed after the berm crest and beach face slope were established. Figure 6.3 shows that as the beach approached equilibrium for DSTi03 (506 minutes) and DSTi04 (638 minutes), the offshore bar trough under the cnoidal waves was deeper than under sinusoidal waves. The berm crest for cnoidal waves was higher than the crest for sinusoidal waves. Hence, to reach equilibrium cnoidal waves carried more sand onshore than sinusoidal waves. Although all tests had the same initial profile and the same wave height and period, the final profiles differed.

For DSTi03, multiple bars formed toward the end of the tests as shown in Figure 6.4. The formation of multiple bars has been reported for many laboratory experiments as well as for field studies. Boczar-Karakiewicz and Davidson-Arnott (1987) explained multiple bars in terms of energy shifts between the fundamental frequency and the first harmonic due to shoaling. The study was based on wave spectra from field measurements. Kriebel, Dally, and Dean (1986) conducted small-scale flume experiments on profile recovery. Wave reflection was found to have a major effect on profile recovery. Reflection from their beach resulted in outer bars at the antinodes of partial standing waves.

Incoming waves are reflected from the steep beach face. This leads to standing waves. As the standing waves become more pronounced, multiple bars form and grow. As partial reflection increased, more bars formed as shown in Figures 6.1 through 6.3. The effect of standing waves on an erodible bed was discussed by Davies (1985). He stated "…standing waves might give rise to the formation of bed features. Beneath the antinodes of standing waves, where the lowest velocities are found close to the bed surface, sedimentation rather than erosion might occur. On the other hand, under the nodes, where there is a greatest horizontal activity near the bed, erosion rather than sedimentation might occur". Komar (1998) discusses the growth of bars under standing waves. See Figure 6.5. In the present study, bar crests were observed approximately at half way between the nodal points of the standing waves.

Once the berm built up, reflected waves were noticeable, i.e. after 84 minutes in DSTi06.

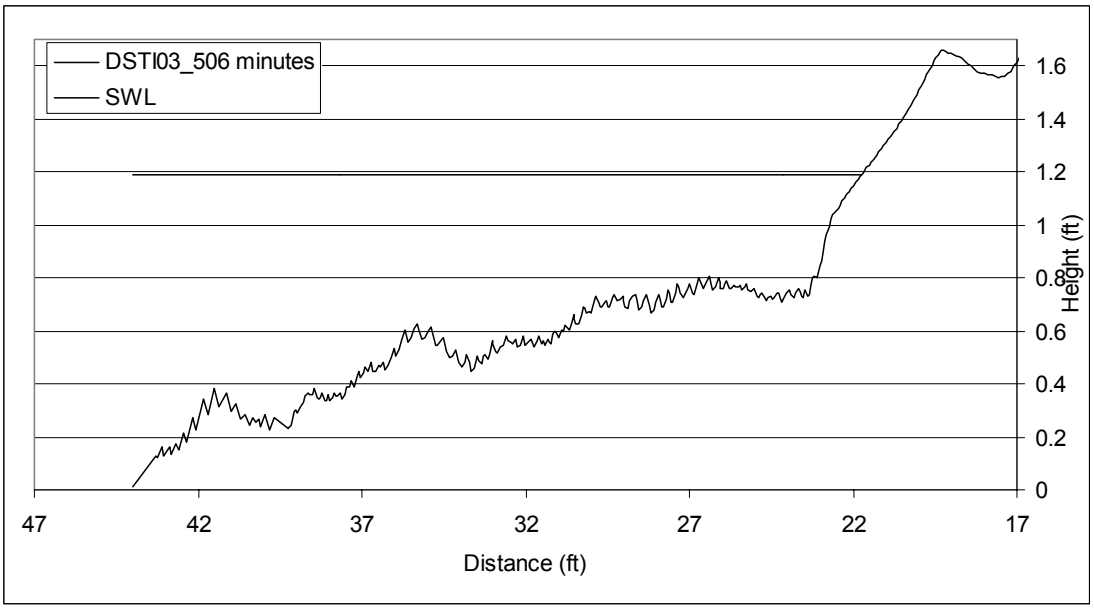

Figure 6.4 Multiple bars at equilibrium, DSTi03

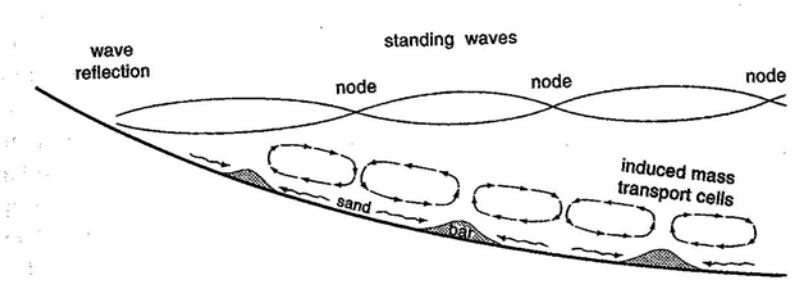

Figure 6.5 Bar formation under standing waves (Komar, 1998)

Berm height depends on breaker height. The higher the waves, the higher will be the berm (Wiegel, 1964, pg.346). This was also observed in the present study. Figures 6.1 through 6.3 show higher berm heights for cnoidal waves, all other factors being equal. Berm height and berm slope are associated with the reflected waves. Berm height and reflection coefficients are shown in Figures 6.6 and Figure 6.7 for sinusoidal and cnoidal waves (DSTi03 and DSTi04) respectively. In the figures h_c = height of berm crest, h_{c_eq} = height of berm crest at equilibrium and C_R = reflection coefficient. The berm crest height at equilibrium was 1.66 ft and 1.84 ft in DSTi03 and DSTi04 respectively. At the start of the tests, wave reflection was small, indicating that most incident wave energy was dissipated. As the profile evolved and berm height increased, more energy was reflected. Figure 6.8.a shows the reflection coefficient as a function of foreshore slope. Cnoidal waves resulted in a steeper foreshore slope and a smaller reflection coefficient than sinusoidal waves. Figure 6.8.b shows the foreshore slope evolution with time expressed as the number of waves, n = t/T, where t is time and T is the wave period.

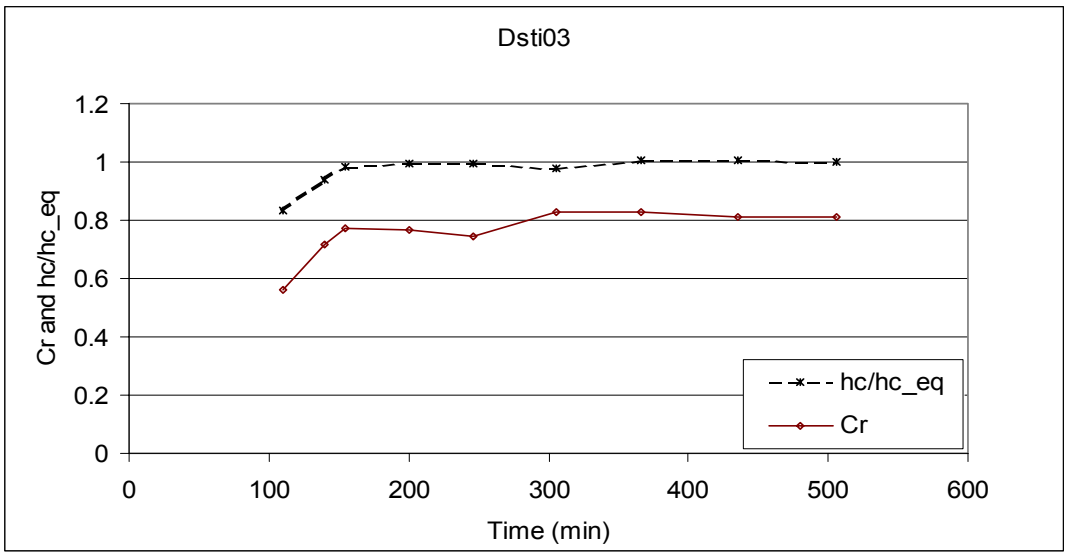

Figure 6.6 Evolution of berm crest and reflection coefficient, DSTi03 (sinusoidal wave)

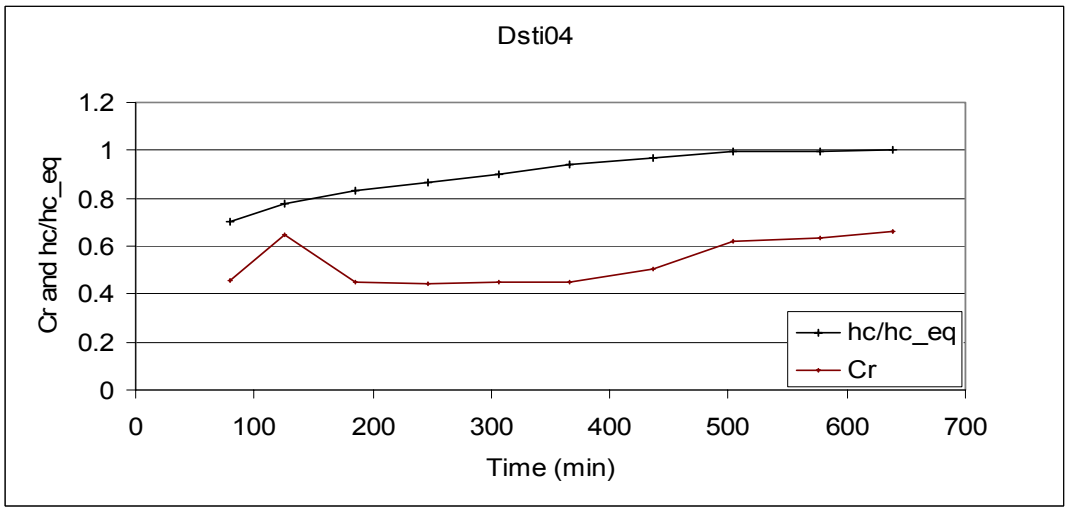

Figure 6.7 Evolution of berm crest and reflection coefficient, DSTi04 (cnoidal wave)

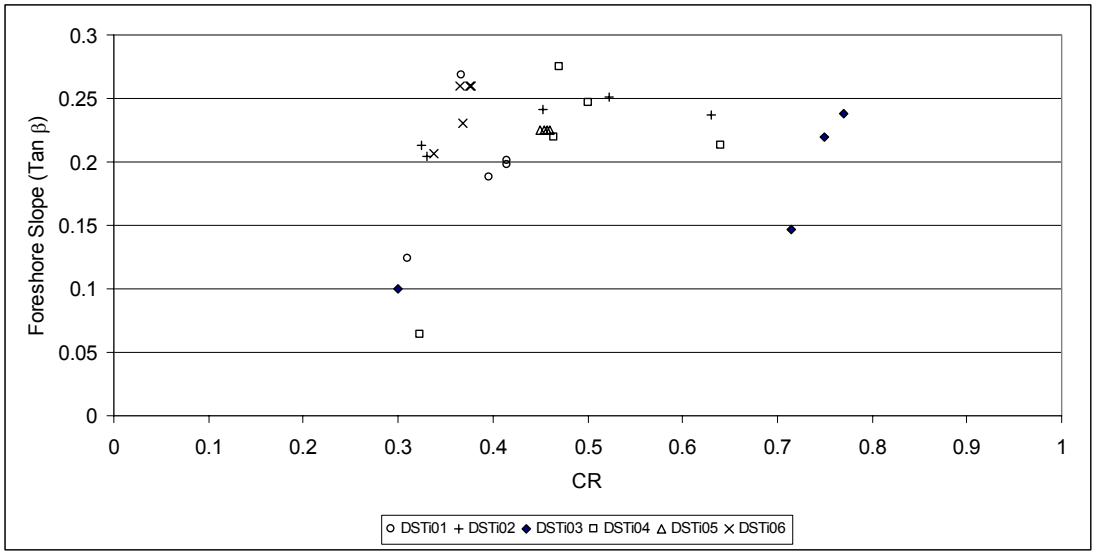

Figure 6.8.a Reflection coefficient (C_R) vs. foreshore slope

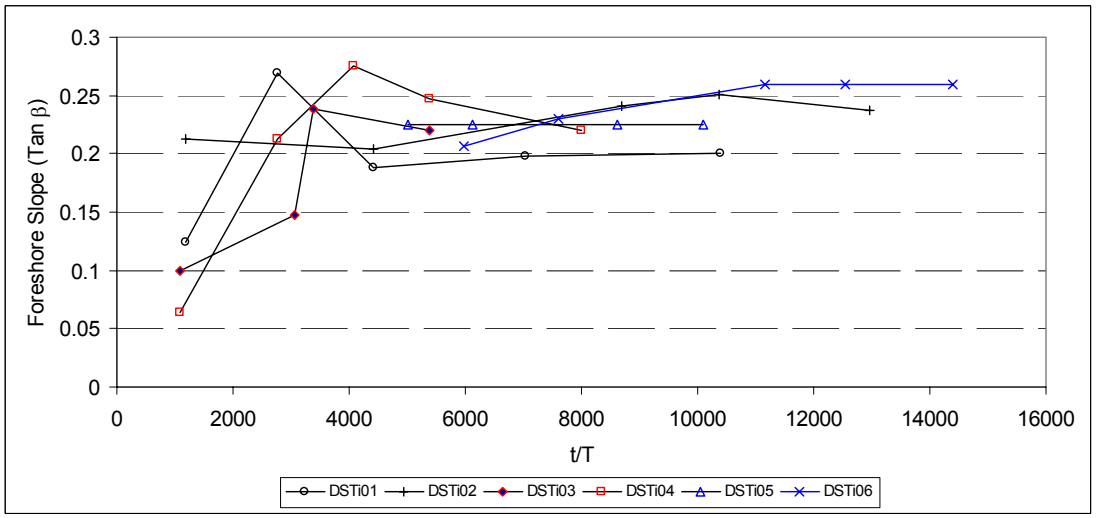

Figure 6.8.b Foreshore slope

Reflection coefficient also differed between cnoidal and sinusoidal tests. C_R showed the difference of beach profile evolution as test progressed. Possible reflection points on the profile were investigated and bottom velocities calculated to quantify the profile difference under the two types of waves. Local phase angles between incident and reflected wave were determined at the gage. Phase difference between incident and reflected waves across the profile were used to determine possible reflection points and bottom velocities.

The phase angle between incident and reflected waves was calculated using the method presented in Chapter 4.1.b. A shift in the phase angle occurred as the berm developed and the profile reached equilibrium. Figures 6.9 and 6.10 show the phase spectra for DSTi03 and DSTi04 for all frequencies over the test duration. Figures 6.11 and 6.12 show phase shifts for the fundamental, 1st, 2nd, and 3rd harmonics for DSTi05 and DSTi06, respectively. That phase shift for the fundamental and 1st harmonic was very small at the wave gage, see Figures 6.11 and 6.12. However, the phase shift was higher for the 2nd and 3rd harmonics. Phase shifts for other tests are given in Appendix J.

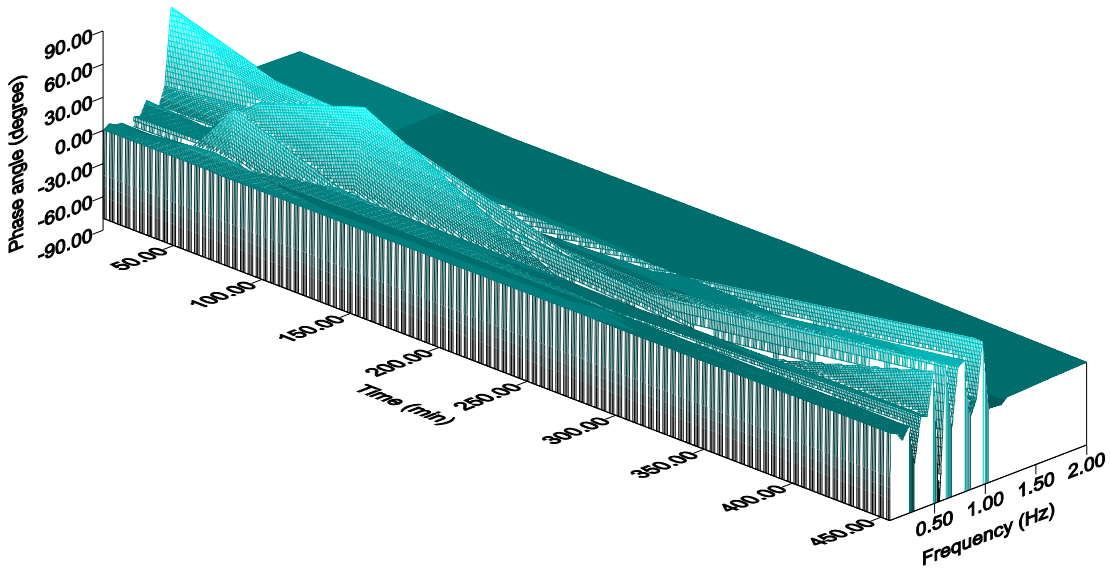

Figure 6.9 Phase spectra, DSTi03

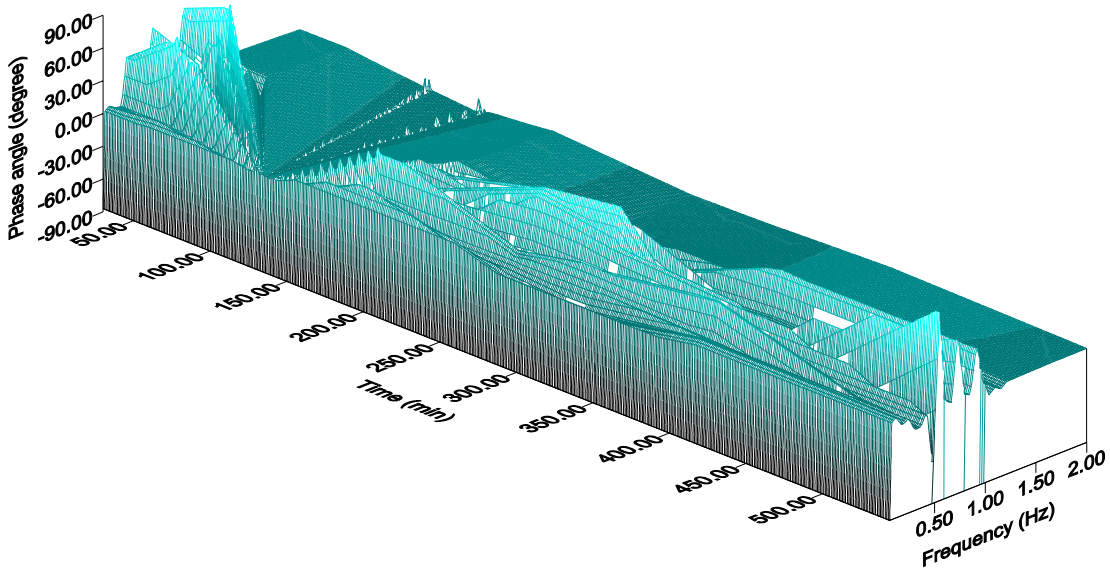

Figure 6.10 Phase spectra, DSTi04

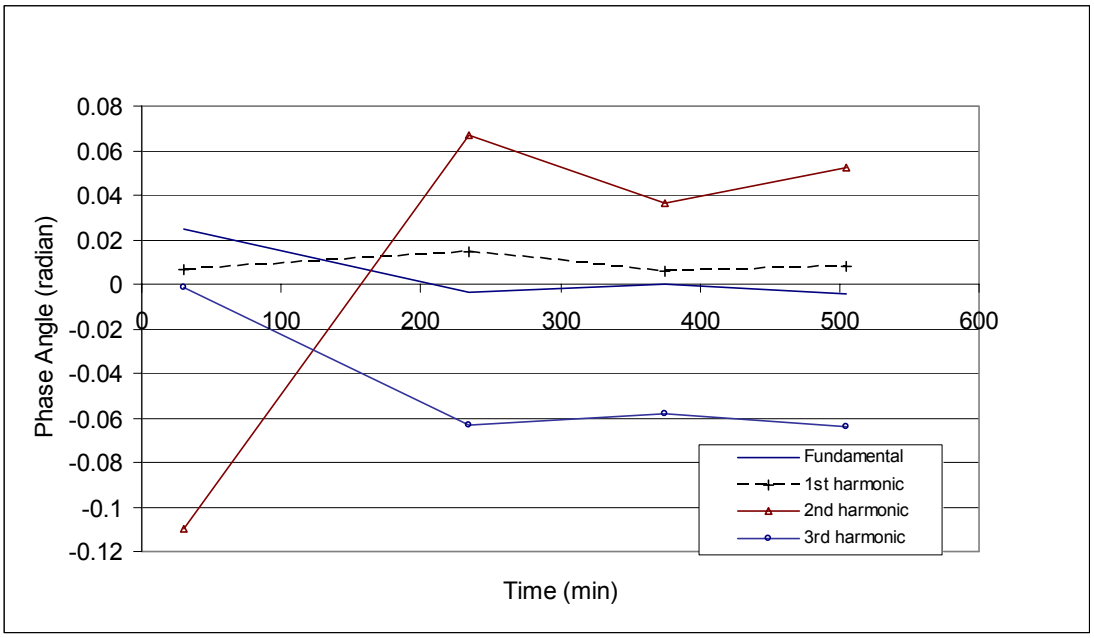

Figure 6.11 Phase shifts for fundamental and higher harmonics, DSTi05

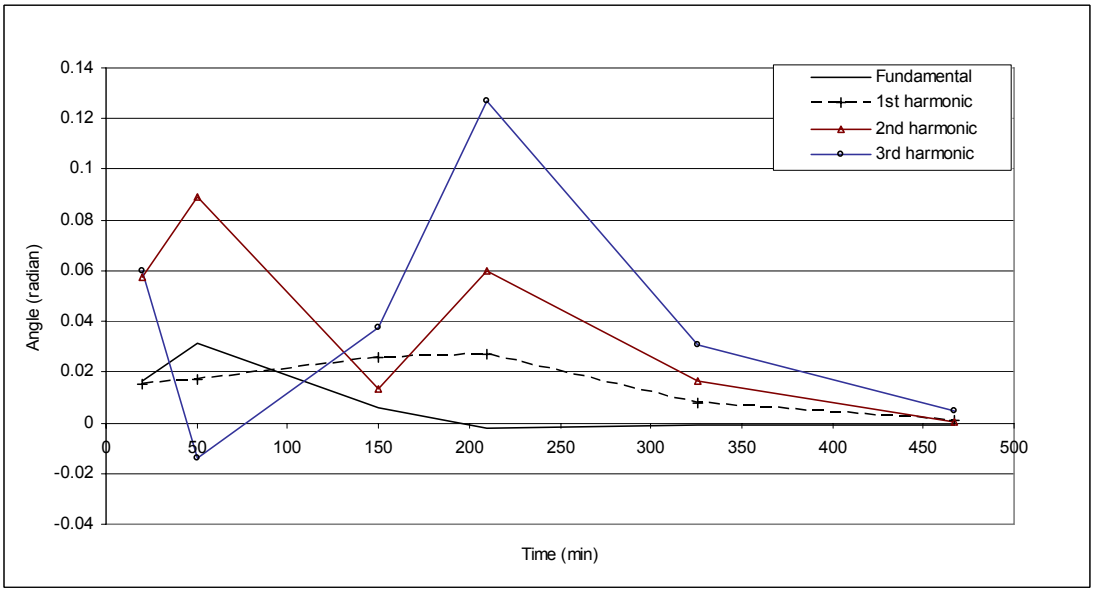

Figure 6.12 Phase shifts for fundamental and higher harmonics, DSTi06

Based on the local phase shifts, "possible" reflection points were calculated for each frequency. Calculation of reflection points is discussed in Chapter 4.1.d. The wave gage location is taken as the initial point for the calculations. Figures 6.13 and 6.14 show the reflection distance, X_R, and travel time, t, and possible reflection points on the equilibrium profiles for DSTi03 and DSTi04, respectively. The reflection point closest to the shoreline is assumed to be the reflection point. The shoreline is 29.78 ft and 29.22 ft from gage for DSTi03 and DSTi04 and possible reflection points are at 26.62 ft and 27.28 ft. This procedure was repeated over the duration of each test and the "evolution of reflection points" calculated. Figures 6.15 through 6.18 show the reflection distance relative to the instantaneous still water line (SWL) and to the equilibrium SWL for DSTi03 and DSTi04, respectively. The horizontal axis is given by number of waves, $n = t/T$. Figure 6.15 and Figure 6.17 show that reflection distances from the equilibrium shoreline start from negative value and increase as the shoreline builds until about 2900 waves. After 2900 waves the berm crest was established. After this, reflection point gradually decreased as beach reached equilibrium. The same behavior of fundamental frequency was observed in other tests. Calculated reflection distances for other tests are given in Appendix J.

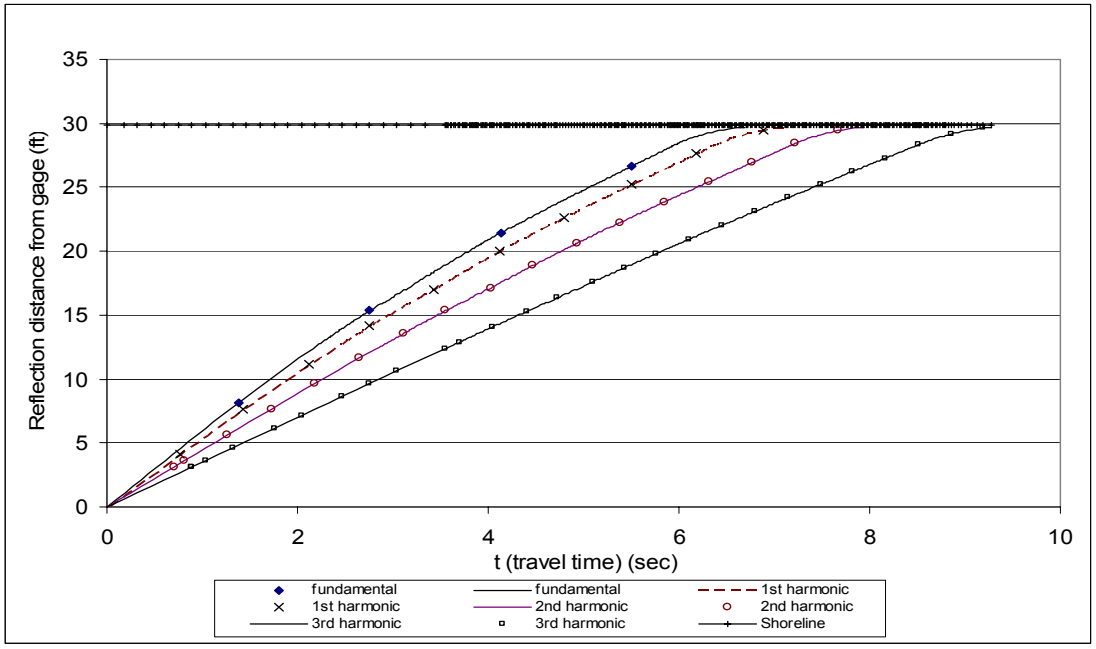

Figure 6.13 Reflection points for DSTi03 at equilibrium profile

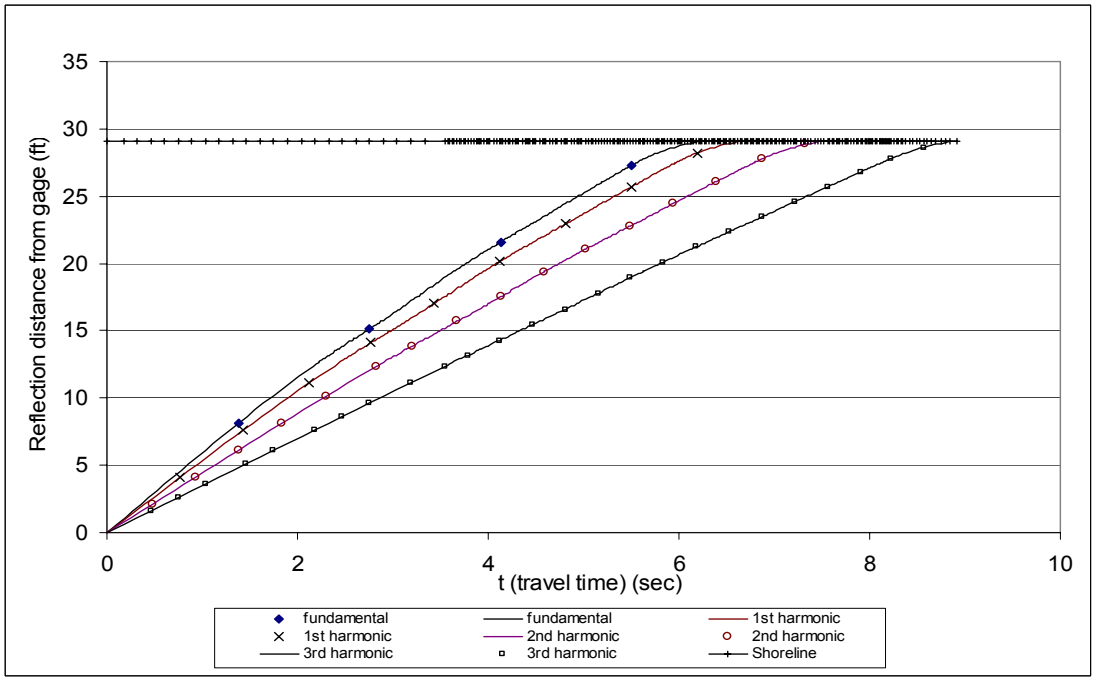

Figure 6.14 Reflection points for DTi04 at equilibrium profile

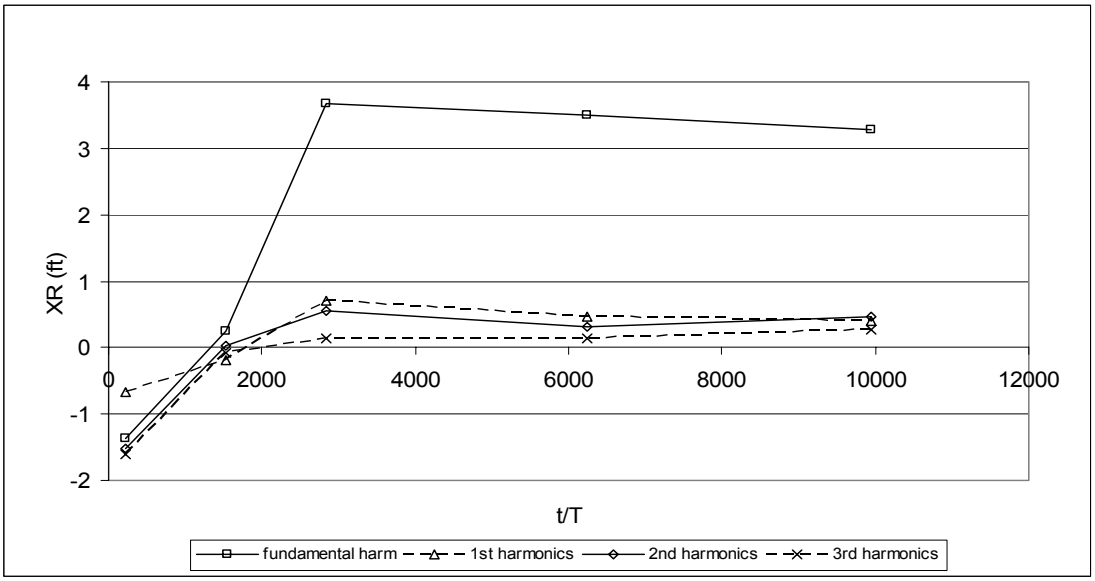

Figure 6.15 Reflection distance (X_R) from the equilibrium shoreline, DSTi03

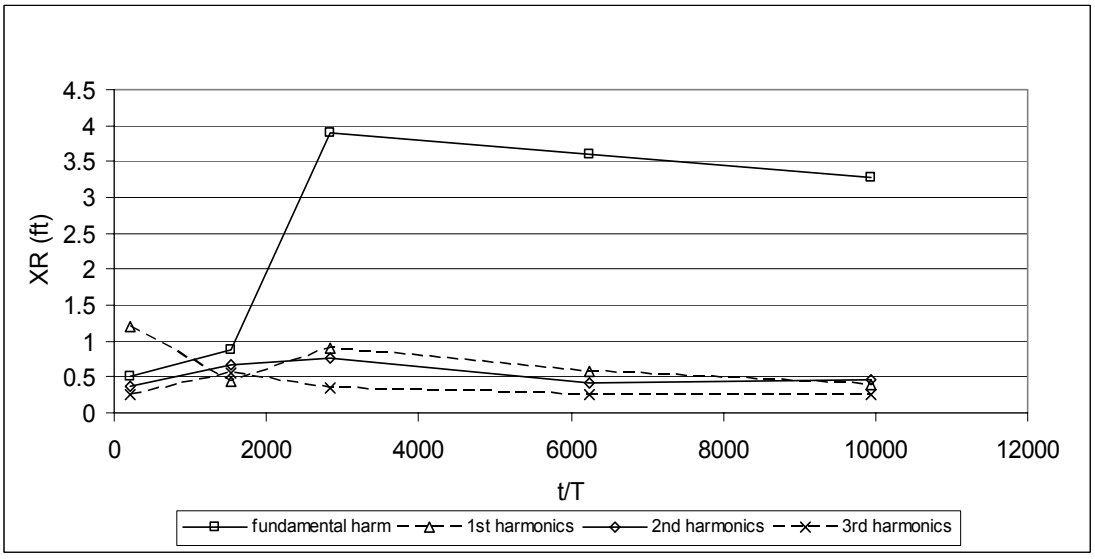

Figure 6.16 Reflection distance (X_R) from the instantaneous shoreline, DSTi03

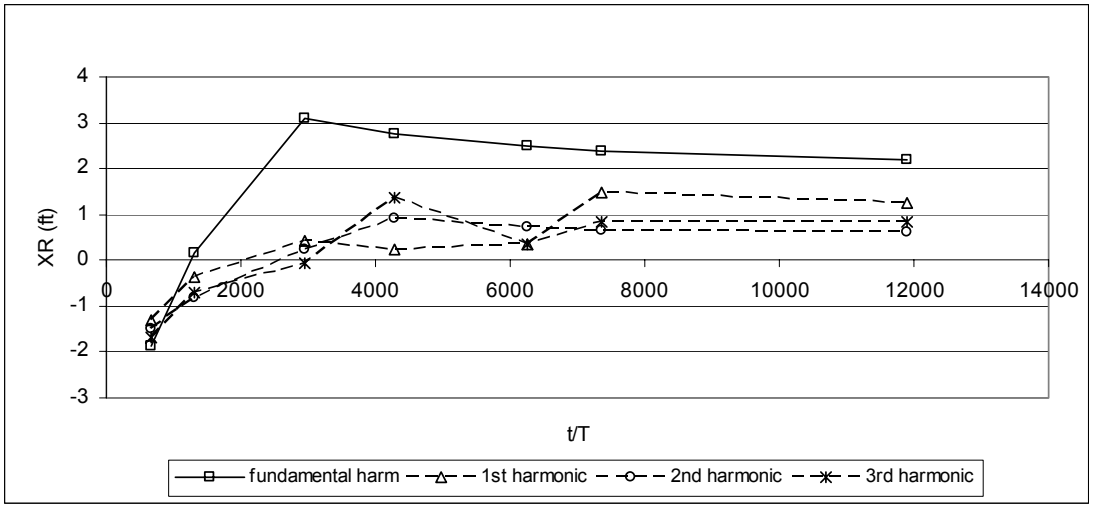

Figure 6.17 Reflection distance (X_R) from the equilibrium shoreline, DSTi04

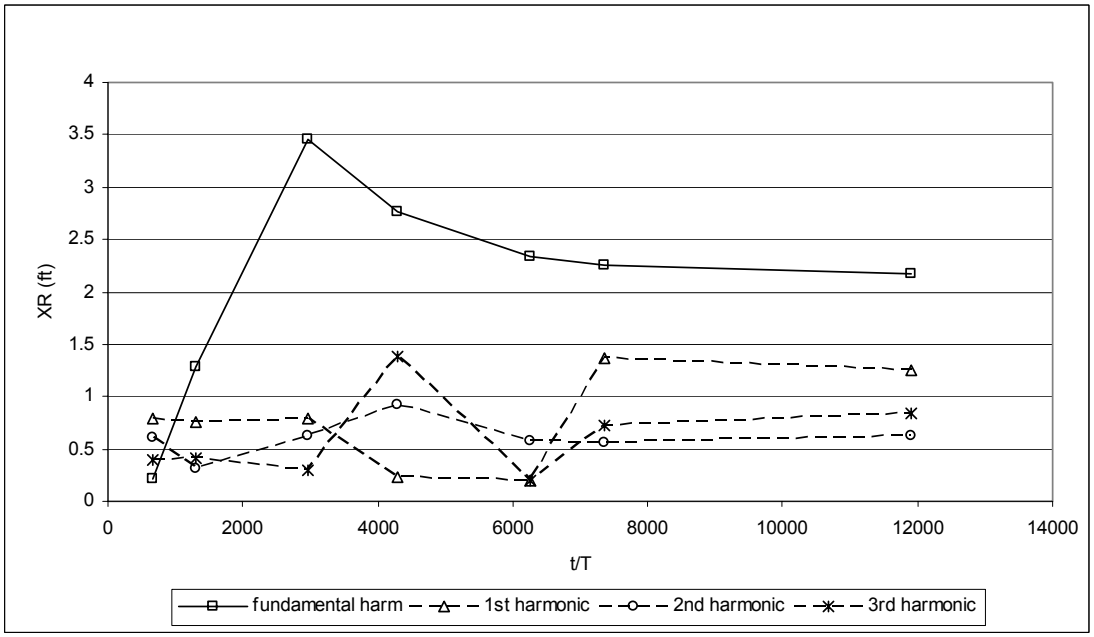

Figure 6.18 Reflection distance (X_R) from the instantaneous shoreline, DSTi04

Local phase difference between incident and reflected waves were used to calculate bottom velocities. The method is discussed in Chapter 5.5. Figure 6.19 and 6.20 show the calculated bottom velocities and the cosine of local phase difference at the start, middle and the end of DSTi03 and DSTi04. Reflection points occur when the cosine of the phase difference is -1 or 1. Bottom velocities toward shore were higher and away from shore lower. Bottom velocities under sinusoidal waves are the same under the wave trough and crest because of wave symmetry. Calculated bottom velocity envelop across the profile for sinusoidal waves under the crest and trough increased with respect to time toward the equilibrium.

Bottom velocities under cnoidal wave crests and troughs are different; onshore velocities are higher and of shorter duration. Offshore velocities are lower and of longer duration. Calculated bottom velocity envelop across the profile for cnoidal waves under the crest decreased with respect to time toward the equilibrium. At equilibrium, cnoidal wave bottom velocity under the trough changed sign and were directed onshore at crest of the bar (Figure 6.20, on the reflected bottom velocity of 544 min of test at 29.95 ft of the profile). Similar behavior was observed in DSTi02.

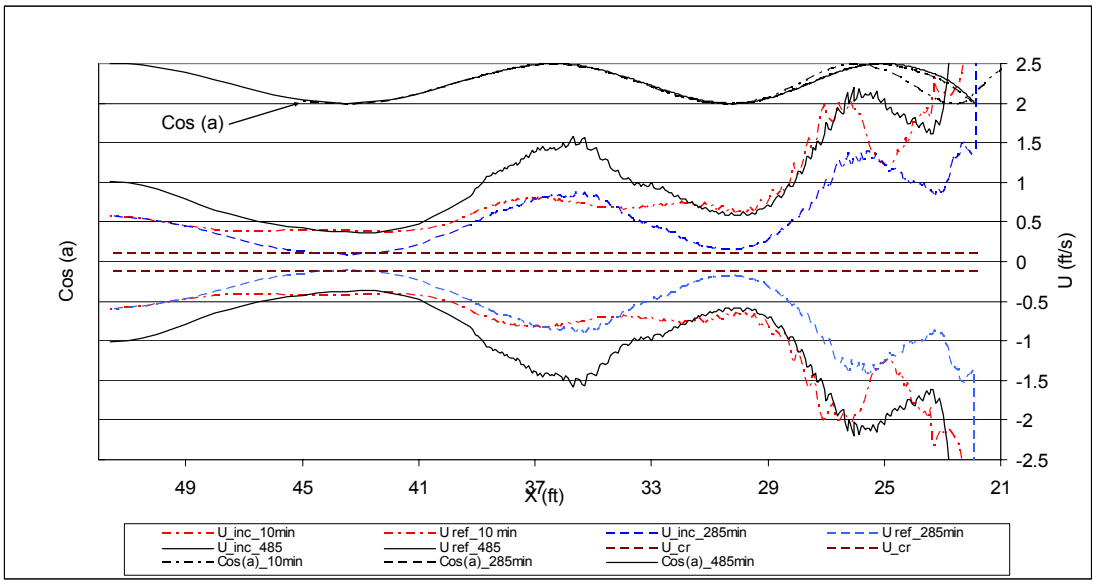

Figure 6.19 Calculated bottom velocities, DSTi03

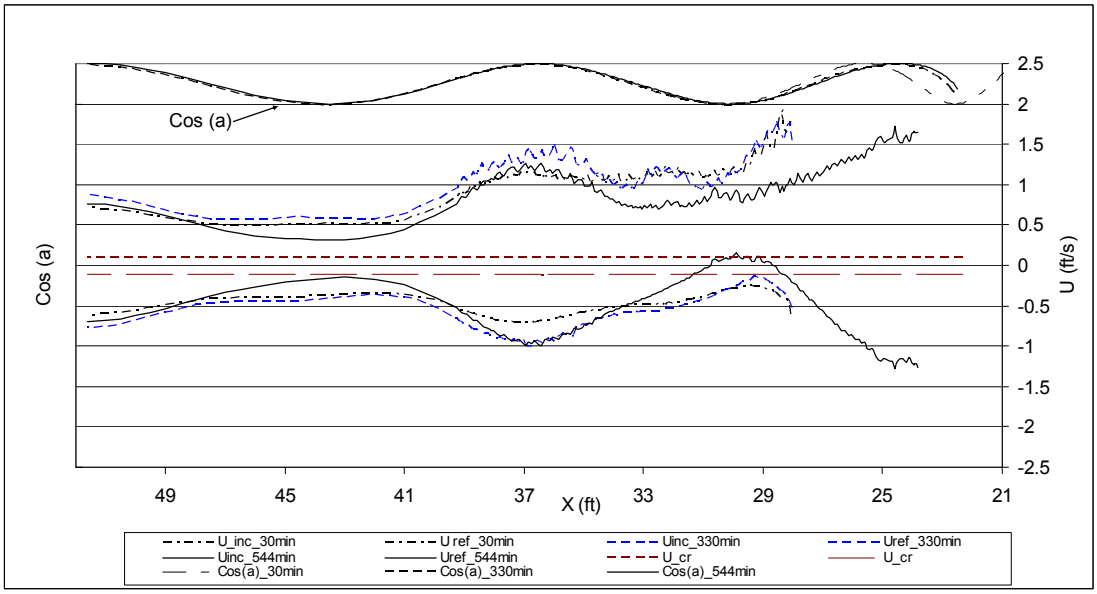

Figure 6.20 Calculated bottom velocities, DSTi04

CHAPTER 7. SUMMARY AND CONCLUSIONS

This dissertation focused on the evolution of accretional beach profiles under cnoidal and sinusoidal waves. Wave spectra for incident and reflected waves, reflection coefficients as the beach profile evolved, phase lags between incident and reflected waves, reflection points on the beach face derived from the phase relations, and calculated near-bottom velocities under cnoidal and sinusoidal waves were investigated.

The variation in reflection coefficient with time during profile evolution shows that equilibrium was attained differently for sinusoidal waves and cnoidal waves. The reflection coefficient reached a constant after the berm face slope was established. The berm slope developed early under sinusoidal waves and later under cnoidal waves. The reflection coefficient is a measure of how much energy is dissipated. High reflection implies minimum dissipation. Therefore, less energy is dissipated under sinusoidal waves than under cnoidal waves following establishment of the berm. Sinusoidal waves affected different part of the profile at different times. Evolution under sinusoidal waves was sequential. The onshore profile was first affected by establishment of the berm slope. Once the onshore accreted, waves worked the offshore portion of the profile. In contrast, cnoidal waves affected the whole beach profile simultaneously. The slope of the berm was complete at the end of the test. Cnoidal waves produce a “deeper” profile than do sinusoidal waves with a deeper trough between bars. The overall beach slope is steeper for cnoidal waves than for sinusoidal waves. See Figure 6.3.

Larson (1999) summarized the conditions that define an equilibrium profile. One condition is that waves dissipate minimum energy as they travel across an equilibrium profile. A second condition is that there is no net sediment transport. A third condition is that there is a balance between onshore transport due to wave asymmetry and offshore transport due to gravity. This is similar as the second condition. Reflection coefficients calculated herein show that less energy is dissipated across the profile as the profile approached equilibrium. Reflection coefficients for cnoidal waves increased with time to reach a constant value at equilibrium. The sinusoidal and cnoidal equilibrium profiles were different. Calculated bottom velocities for the waves used in this study showed that they increased as equilibrium was approached. Bottom velocities under crest and trough were higher under sinusoidal waves than that of cnoidal waves.

Times when standing waves were first observed during a test are given in Table 6.1. When standing waves occur the near bottom horizontal velocities are higher at the nodes and lower at the antinodes. This results in an accumulation of sediment beneath the antinodes to form a bar. Multiple bars were observed at equilibrium.

Multiple bars have also been observed on profiles in the field. Boczar-Karakiewicz and Davidson-Arnott (1987) explained multiple bars in terms of energy transfer from the fundamental wave frequency to the first harmonic due to shoaling. In the present study, reflected wave spectra showed energy transfer from the fundamental to the first harmonic for both sinusoidal and cnoidal waves. See Figures 4.6 and 4.8. Energy transfer was more pronounced in cnoidal waves resulting in deeper bar-troughs. Energy transfers were observed as the beach profile evolved. The first harmonic increases as the berm crest builds. Once the beach face is established, the energy in the fundamental increases.

An important finding of this study is that cnoidal waves better represent beach and wave interaction nearshore. By looking at spectra of incident and reflected waves, the energy transfer from the fundamental to higher harmonics and back again is observed as also observed in the field. One therefore concludes that cnoidal waves should be used in studies of beach profile evolution in the laboratory tests.

7.1. RECOMMENDATIONS FOR FUTURE RESEARCH

1. Additional tests with both erosionary and accretionary waves at different scales should be conducted to quantfy the reflection process for sinusoidal and cnoidal waves.
2. Measurements of cnoidal wave characteristics across a profile should be made to determine frequency shifts, energy losses and reflection coefficients.
3. Tests with random waves having the same energy as cnoidal waves should be conducted and the behavior of the reflection coefficient investigated for the various component frequencies.

Bibliography

Abramowitz, M., and I.A. Stegun (1968) Handbook of Mathematical Functions, Dover Publications, New York.

Ahrens J.P, and E.B. Hands (2000) A simple perspective on cross-shore sediment movement. Shore &Beach, Vol.68, No.4, pp. 3-14

Bendat, J.S., and A.G. Piersol, (1971) Random data: analysis and measurement procedures, John Wiley & Sons, Canada.

Buhr Hansen, J. (1980) Experimental investigation of periodic waves near breaking. Proc. 16th Coastal Engnrg. Conf., pp.261-277.

Dean R.G., and R.Dalrymple (2002) Coastal Processes with Engineering Applications, Cambridge University Press, United Kingdom.

Dean R.G. (1980) Notes for a Course on Spectral Analysis with Emphasis on Directional Wave Spectra, Course presented at the Coastal Engineering Research Center, Fort Belvoir, VA.

Dingemans, M.W. (1997) Water Wave Propagation over Uneven Bottoms, Part 2, World Scientific, Singapore.

Emery, W., and R. Thomson (2001) Data Analysis Methods in Physical Oceanography, 2nd edn. Elsevier, Netherlands.

Feir J. (1975) Notes on non-linear waves. Personal Communication.

Goda Y., and Y. Suzuki (1976) Estimation of Incident and Reflected Waves in Random Wave Experiments, 15th Coastal Engrg. Conf., Honolulu, Chap. 48, pp.828-845.

Golden Software, Inc. (1994) SURFER version 5.02, surface mapping system software, Golden, Colorado.

Goring, D.G. (1978) Tsunami: the propagation of long waves onto a shelf. PhD. Thesis, California Institute of Technology, Pasadena, CA.

Hardy, T.A., and N. C. Kraus (1987) A numerical model for shoaling and refraction of second-order cnoidal waves over an irregular bottom, Technical Report CERC-87-9, Coastal Engineering Research Center, U.S. Army Engineer Waterways Experiment Station, Vicksburg, MS.

Herbich, J.B., ed. (1999) Developments in Offshore Engineering, Gulf Publishing Company, Texas.

Herbich, J.B., ed. (1990) Handbook of Coastal and Ocean Engineering, Vol.1 Wave phenomena and Coastal Structures, Gulf Publishing, Texas.

HR Wallingford (1996) Flume wave generation system for Drexel University. Operating Manual, Howbery Park, Wallingford, UK.

Hughes, S.A. (1982) 'PCGODA', a computer program to separate incident and reflected waves. Personal Communication.

Hughes, S.A. (1993) Physical Models and Laboratory Techniques in Coastal Engineering, World Scientific, Singapore.

Ippen, A.T., ed. (1966) Estuary and Coastal Hydrodynamics, Mc-Graw-Hill, New York.

Isobe, M. (1985) Calculation and application of first order cnoidal wave theory, Coastal Engineering, Vol.9, pp. 309-325.

Komar, P.D. (1998) Beach Processes and Sedimentation, Prentice-Hall, New Jersey.

Korteweg, D.J., and de Vries, G. (1895) On the change of form of long waves advancing in a rectangular canal, and on a new type of long stationary waves, Philosophy magazine, Series 5, Vol. 39, pp. 422-443.

Kraus, N.C., and M. Larson (1988) Beach Profile Change Measured in the Tank for Large Waves 1956-1957, Technical Report CERC-88-6, Coastal Engineering Research Center, U.S. Army Engineer Waterways Experiment Station, Vicksburg, MS.

Kraus, N.C. and J.M. Smith (1994) SUPERTANK laboratory data collection project, Vol I, Technical Report CERC-94-3, Coastal Engineering Research Center, U.S. Army Engineer Waterways Experiment Station, Vicksburg, MS.

Laitone, E.V. (1960) The Second Approximation to Cnoidal and Solitary Waves, Journal of Fluid Mechanics, Vol.9, pp.430-444.

Larson, M., and N.C. Kraus (1989) SBEACH: Numerical Model for Simulating Storm-Induced Beach Change, Report 1, Empirical foundation and model development, Technical Report CERC-89-9, US Army Engineer Waterways Experiment Station, Vicksburg, MS.

Larson, M. (1988) Quantification of Beach Profile Change, Rept. 1008, Dept. of Water Resources, Eng. Univ. of Lund.

Larson, M. Kraus, N.C. and Wise, R.A., (1999) Equilibrium beach profile under breaking and non-breaking waves, Coastal Eng. 36(1), pp. 59-85.

Madsen, O.S., and W.D. Grant, (1976) Quantitative description of sediment transport by waves, Proc. 15th Coastal Engng. Conf., Honolulu, Vol.2, pp.1093-1112.

Mansard, E.P.D., Funke, E.R., (1980) The measurement of incident and reflected spectra using a least square method, Proc. 17th Coastal Eng. Conf., Reston, VA. pp.154-172.

Massel, S.R. (1996) Ocean Surface Waves, Their Physics and Predictions, World Scientific, Singapore.

Morden, D.B., and Richey, E., and Christensen, D.R. (1976) Decomposition of co-existing random wave energy, Proc. 15th Coastal Eng. Conf., Honolulu, Chap. 49, pp.846-865.

Raudkivi, A.J. (1990) Loose Boundary Hydraulics, 3rd ed. Pergamon Press, Oxford, Great Britain.

Santamarina, J.C., and D. Fratta (1998) Introduction to discrete signals and inverse problems in civil engineering, ASCE, Virginia.

Sarpkaya, T., and M. Isaacson (1981) Mechanics of wave forces on offshore structures, Van Nostrand Reinhold Company, New York.

Saville, T. (1957) Scale effects in two dimensional beach studies. Transactions from the 7th General Meeting of the International Association of Hydraulic Research. Vol.1, pp. A3-1-A3-10.

Silvester, R., and J.R.C. Hsu (1997) Coastal Stabilization, World Scientific, Singapore.

Sleath, J.F. (1984) Sea bed mechanics, John Wiley & Sons, Canada.

Stewart R. (2002) Introduction to Physical Oceanography, Texas A&M University.

Suh, K.D. and W.S. Park (2001) Separation of incident and reflected waves in wave current flumes, Coastal Engineering Vol. 43 pp.149-159.

Svendsen, I.A. and J. Buhr Hansen (1976) Deformation up to breaking of periodic waves on a beach, Proc. 15th Coastal Engrg. Conf., Honolulu, Chap. 27, pp.477-496.

Svendsen, I.A., and O. Brink Kjaer (1972) Shoaling of cnoidal waves. Proc. 13th Coastal Engrg. Conf., Vancouver, Chap.18, pp.365-384.

Svendsen, I.A., (1984) Wave heights and set-up in a surf zone. Coastal Engineering, Vol.8, pp. 303-329.

U.S. Army Corps of Engineers (1984) Shore Protection Manual, Coastal Engineering Research Center, U.S. Army Corps of Engineers.

Wiegel, R.L. (1964) Oceanographical Engineering, Prentice Hall, New Jersey.

Appendix A. Notation

Symbol	Description
A	Dimensional shape parameter
C_g	Group velocity
C_R	Reflection coefficient
D	Wave energy dissipation per unit volume
D_{eq}	Equilibrium energy dissipation per unit volume
$E(m)$	Second complete elliptic integral
E_f	Energy flux
E_p	Potential energy per unit wave length
E_k	Kinetic energy per unit wave length
H_u	Frequency response function
H	Wave height
H_0	Deepwater wave height
H_i	Incident wave height
H_r	Reflected wave height
$K(m)$	First complete elliptic integral
K	Transport rate coefficient
L_0	Deepwater wave length
T	Wave period
T_i	Cumulative travel time
U	Ursell number = HL^2/h^3
X_R	Possible reflection point from shoreline

a_c	Distance from still water surface to the crest
a_t	Distances from still water surface to the trough
a_I	Incident wave amplitudes
a_R	Reflected wave amplitudes
c	Phase celerity
cn	Jacobian elliptic cosine function
c_n	Amplitude spectrum
g	Acceleration of gravity
h	Still water depth
k	Wave number = $2\pi/L$
l_o	Distance from the wave gage to the possible reflection point
m	Elliptic modulus
q	Sediment transport rate
u_c^b	Bottom velocity under the crest of a wave
u_t^b	Bottom velocity under the trough of a wave
w	Sediment fall velocity
x	Horizontal distance
y_t	Height of the wave trough above the horizontal bottom
y_c	Height of the wave crest above the bottom
σ	Angular frequency = $2\pi/T$
ε_I	Phase angles of the incident waves
ε_R	Phase angles of the reflected waves
ε	Transport rate coefficient for the slope-dependent term
ρ	Density of the water

κ	Breaker index
$\eta(x,t)$	Water surface profile
ξ	Paddle displacement
φ	Phase angle
Δl	Distance between the two adjacent wave gages

Appendix B. Numerical Evaluation of Elliptic Functions

The method of numerical evaluation of elliptic functions presented here is adapted from Goring (1978). The first step in computing any of elliptic function is to set up the Arithmetic/Geometric Mean (AGM) table for the elliptic modulus, m.

$a_0 = 1$	$b_0 = \sqrt{m'}$	$c_0 = \sqrt{1-m'}$
$a_1 = \frac{1}{2}(a_0 + b_0)$	$b_1 = \sqrt{a_0 b_0}$	$c_1 = \frac{1}{2}(a_0 - b_0)$
$a_2 = \frac{1}{2}(a_1 + b_1)$	$b_2 = \sqrt{a_1 b_1}$	$c_2 = \frac{1}{2}(a_1 - b_1)$
---	---	---
---	---	---
$a_N = \frac{1}{2}(a_{N-1} + b_{N-1})$	$b_N = \sqrt{a_{N-1} b_{N-1}}$	$c_N = \frac{1}{2}(a_{N-1} - b_{N-1})$

Stop at the N^{th} step, where $a_N = b_N$ (i.e. $c_N = 0$) to the accuracy desired. (typically, $c_6 < 10^{-5}$.)

From the AGM, the elliptic functions are calculated as follows:

1. First complete Elliptic Integral K.

$$K = \pi/(2a_N)$$

2. Second Complete Elliptic Integral E.

$$E = K\{1 - \frac{1}{2}(c_0^2 + 2c_1^2 + 2^2 c_2^2 + ... + 2^N c_n^2)\}$$

3. Jacobian Elliptic Function, cn(w).

a) Find $\phi_N = 2^N a_N w$ in radians.

b) Compute successively $\phi_{N-1}, \phi_{N-2}, ... \phi_1, \phi_0$ from the recursive relation:

$$\sin(2\phi_{n-1} - \phi_n) = \frac{c_n}{a_n} \sin\phi_n$$

c) Evaluate cn(w)= $\cos\phi_0$.

4. Inverse Jacobian Elliptic Functions w = cn^{-1}(P).

a) Find ϕ_0 from:

$$\cos\phi_0 = \text{cn(w)}$$

b) Compute successively $\phi_1, \phi_2, ... \phi_N$ from the recursive relation:

$$\tan(\phi_{n+1} - \phi_n) = \frac{b_n}{a_n} \tan\phi_n$$

c) Evaluate:

$$\text{cn}^{-1}(\text{P}) = \phi_N / 2^N a_N$$

The recursive relation is ambiguous by multiples of π. However w converges to the exact value from below so the correct ϕ_n can be found by evaluating w at each step using:

$$w(\phi_n) \geq w(\phi_{n-1})$$

5. Second Incomplete Elliptic Integral E(w).

$$E(w) = \frac{E}{K} w + c_1 \sin\phi_1 + c_2 \sin\phi_2 + ... + c_N \sin\phi_N \quad ,$$

where ϕ_n are those calculated from the recursive relations above.

Appendix C. Computer Program to Calculate Cnoidal Waves

```
/*This program calculates the first and second complete elliptic integrals (K(m) and E(m)
respectively) for a given m value and cn values and free surface of a cnoidal wave of direct
solution of KdV eq*/
 /*Equations used here are based on the Gorin's Thesis (1978) and from the book "Water
wave propagation by Martin Dingeman*/  /*Written by Mehmet Hinis*/

#include<stdio.h>
#include<math.h>
FILE *fp,*fr;
float pi= 3.141592;
double m,m1,m2; float H,h,T,C,L,g,E,K,T_cal,ac,at;
float ellFunc(double m); void bulkhead(int num) ;
double cn[1001],eta[1001],theta[1001],Ein[1001],ksi[1001],phi[7],q2;
float a[7],b[7],c[7],c1[7],t,dt; char str[15];
main()
{
if ((fp=fopen("Cnoidal.txt","a+"))==NULL)
{printf("\n***Error opening file***\n");
 }
printf ("\n\nPlease enter wave height, H = ");
scanf ("%f",&H);
printf ("\nPlease enter water depht, h = ");
scanf ("%f",&h);
printf ("\nPlease enter gravitational accelaration, g = ");
scanf ("%f",&g);
printf("\nPlease enter the desired value of T = ");
scanf("%f",&T);
m=0.5;m2=0.5;T_cal=0;
while(fabs(T_cal-T)>0.00001&&m<1)
      {
T_cal=ellFunc(m);
if (fabs(T_cal-T)<0.01)
           break;

/*Blind shooting for value of m*/
if (T_cal<T)
           {
m2=m;
m=0.5*(m+1.0);
           }
else if (T_cal>T)
{m=0.5*(m+m2);}
      }
printf("\nL = %f, \nC = %f,\nT_cal = %f,\nm = %g\nm1=%g",L,C,T_cal,m,m1);
float freqDisp;freqDisp=T_cal*sqrt(g/h);
printf("\nfreqDisper = %f",freqDisp);
printf("\tFrequency Dispersion should be bigger than 7");
```

```
float Urs; Urs=H*L*L/(h*h*h);
printf("\nUrsell number is = %f", Urs);

/*Calculation of surface profiles*//*ac and at are the crest and trough surfaces*/
at=(H/m-H*E/(m*K))+h-H;
printf("\nat= %f  K=%f   E=%f    ",at,K,E);

/* Calculation of CN and eta  */
int n;theta[0]=0;
fprintf(fp,"\nH = %f, h = %f,T = %f ",H,h,T);
fprintf(fp,"\nL = %f, C = %f,T_cal = %f,m = %g   m1=%g",L,C,T_cal,m,m1);
fprintf(fp,"\nat= %f  K=%f   E=%f    ",at,K,E);
fprintf(fp,"\n cn              eta               ksi");
printf("\nEnter the name of the file do you want to produce ");
scanf("%s",&str);
printf("\nyou have entered %s",str);
if ((fr=fopen(str,"w+"))==NULL)
{printf("\n***Error opening file***\n");
 }
printf("\nHow many waves do you want to calculate?");
int num; scanf("%d",&num);
printf("\nWhat should be the time step in calculation of the Bulkhead?");
scanf("%f",&dt);
float T1,T2,T3,T4; T1=T/dt;T2=T1/2;T3=1.5*T1;T4=15/dt;
for(t=T2;t<T3;t++)
    {
phi[6]=64*a[6]*2*K*dt*t/T;
for (n=6;n>0;n=n-1)
{
q2=(c[n]/a[n])*sin(phi[n]) ;
phi[n-1]=0.5*(asin(q2)+phi[n]);
}
cn[t]=cos(phi[0]);
eta[t]=at-h+H*pow(cn[t],2);
Ein[t]=(E/K)*theta[t]+c[1]*sin(phi[1])+c[2]*sin(phi[2])+c[3]*sin(phi[3])+c[4]*sin(phi[4])+c
[5]*sin(phi[5])+c[6]*sin(phi[6]);
theta[t+1]=theta[t]-(2*K*h*t/T+(at-H*m1/m)*theta[t]+(H/m)*Ein[t])/(at+H*pow(cn[t],2));
ksi[t]=(L/(2*K*h))*((at-h)*theta[t]+(H/m)*(Ein[t]-m1*theta[t]));
fprintf(fp,"\n%f         %f         %f",cn[t],eta[t],ksi[t]);
          }
/*This part calculates bulkhead for the number of waves*/
int i; for(t=0;t<T4;t++)
{
fprintf(fr,"\n0");
}
for(i=0;i<num;i++)
{
for(t=T2;t<T3;t++)
{
fprintf(fr,"\n%.3f",ksi[t]);
}
```

```
}
fclose(fp); fclose(fr);
return 0;
}
float ellFunc(double m)
 {
/*Calculation of AGM parameter*/
m1=1-m; a[0]=1;b[0]=sqrt(m1) ;c[0]=sqrt(m); int n;
for (n=1;n<7;n++)
{  a[n]=0.5*(a[n-1]+b[n-1]);
b[n]=sqrt(a[n-1]*b[n-1]);
c[n]=0.5*(a[n-1]-b[n-1]);
}
K=pi/(2*a[6]);
E=K*(1-
0.5*(pow(c[0],2)+2*pow(c[1],2)+4*pow(c[2],2)+8*pow(c[3],2)+16*pow(c[4],2)+32*pow(c[
5],2)));
/* Calculation of Period T *//*Equations used for this calculation are given below :*/
/* Wave length   :L=sqrt((16/3*h^3/H)*m)*Km */
/* Wave celerity :C=(1+(H/h)*(2/m-3*E/(m*K)))*sqrt(g*h)  */
/* Wave period   :T_cal=L/c    */
L=sqrt((16/3)*h*h*h*(m)/H)*K;
C=(1+H/(m*h)-H/(2*h)-3*E*H/(2*m*K*h))*sqrt(g*h) ; T_cal=L/C;
 return T_cal;
}
```

Appendix D. Permeability Tests

Two permeability tests were performed after DSTi04 reached equilibrium. A cylindrical pipe was placed on the beach and filled with water and falling head in time was recorded. Figure L.1 and L.2 give the result of falling head of water with respect to time at beach face 21 ft and behind the berm at 17 ft., test 1 and test 2, respectively. Permeability is calculated by,

$$k = \frac{aL}{At}\ln(\frac{h_0}{h_t}) \tag{D.1}$$

where, k = permeability, a =area of pipe, A = Area of specimen, L = length of specimen, t = elapsed time of test, h_0 = head at the beginning, h_t = head at the end.

Permeability for test 1 is found k_1 = 0.14 cm/s and for test2 is k_2= 0.113 cm/s. This result suggest that sand behind the berm has more opening (air) than sand on the beach face.

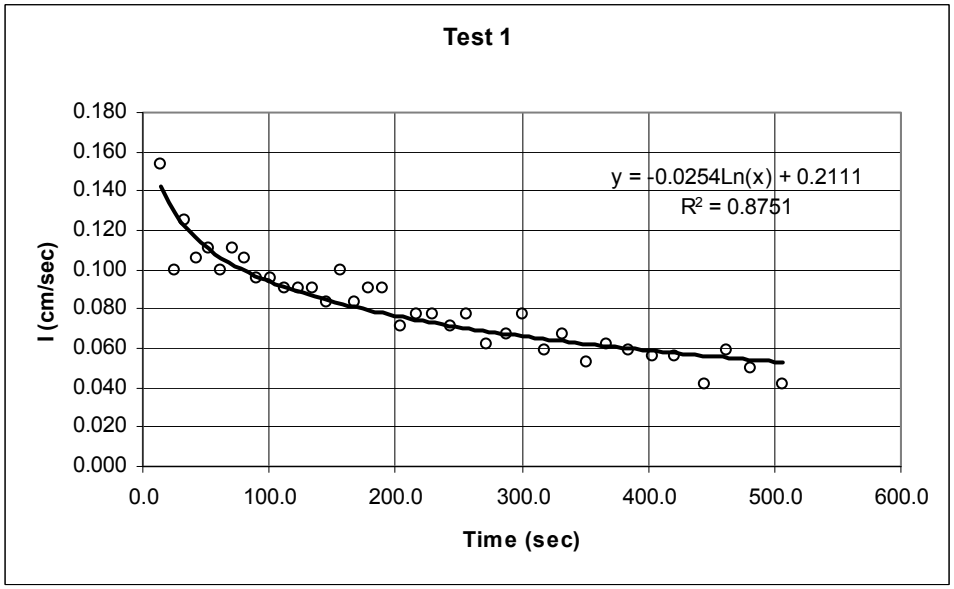

Figure D.1 Permeability test performed at beach face at 21 ft, partially saturated sand

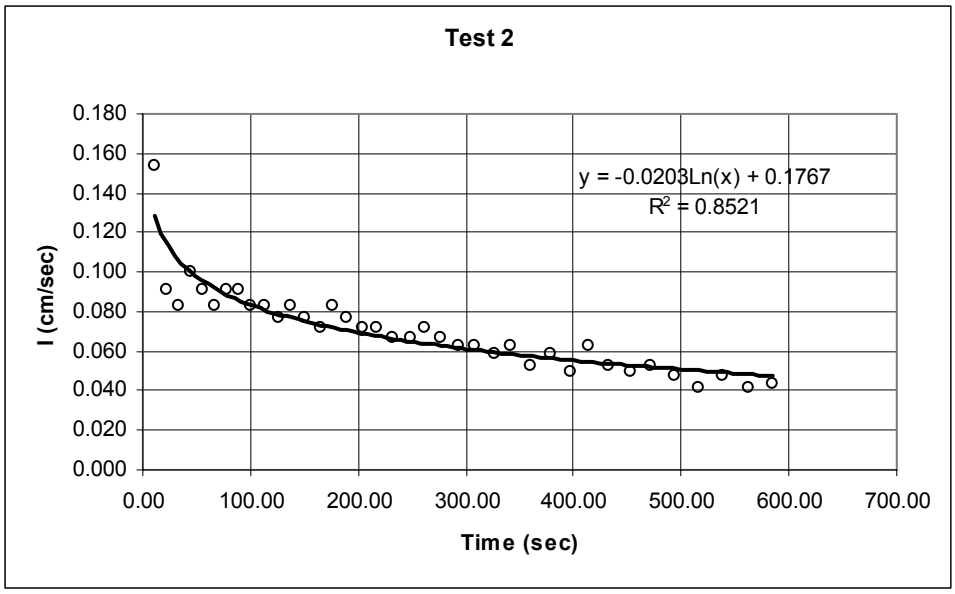

Figure D.2 Permeability test performed at behind the berm at 17 ft, unsaturated sand

Appendix E. Energy Spectra of Incident and Reflected waves

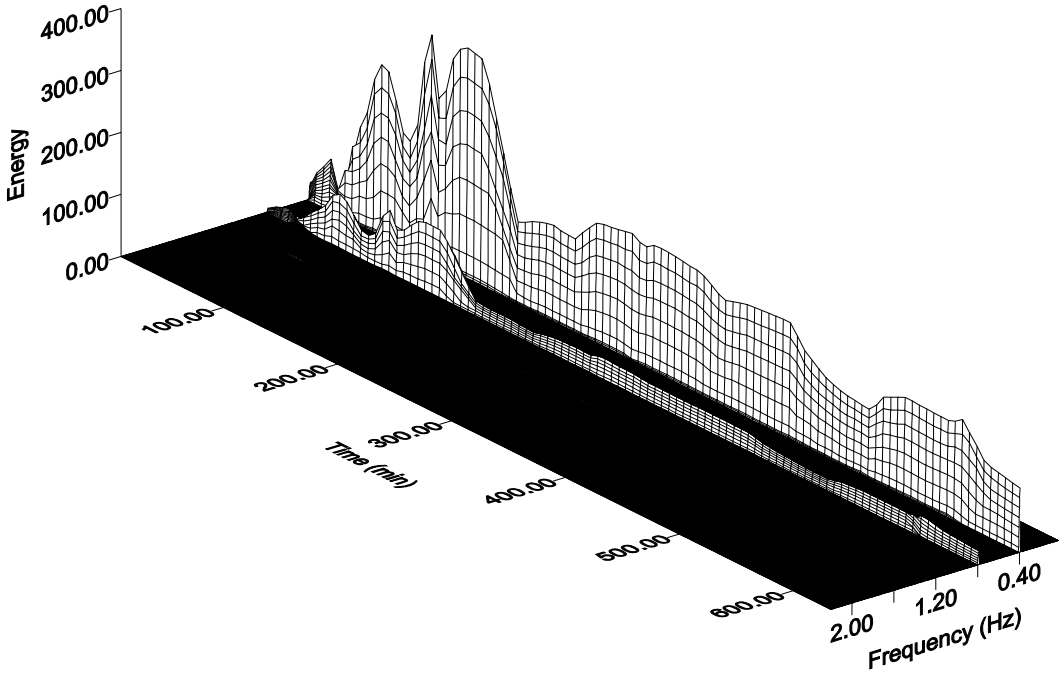

Figure E.1 DSTI01 Incident wave spectra

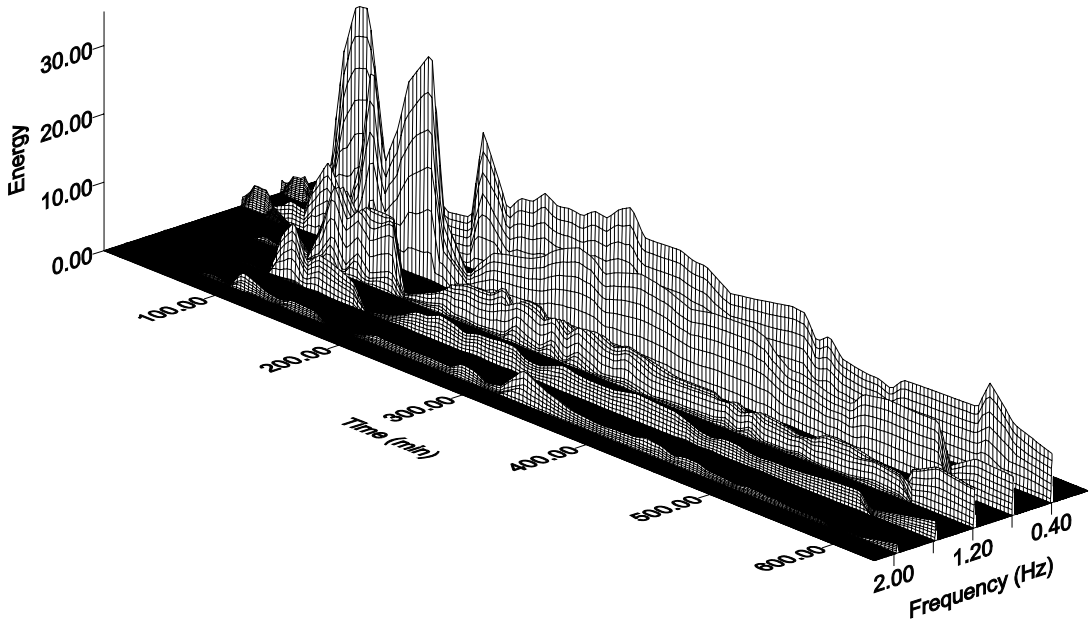

Figure E.2 DSTI01 Reflected wave spectra

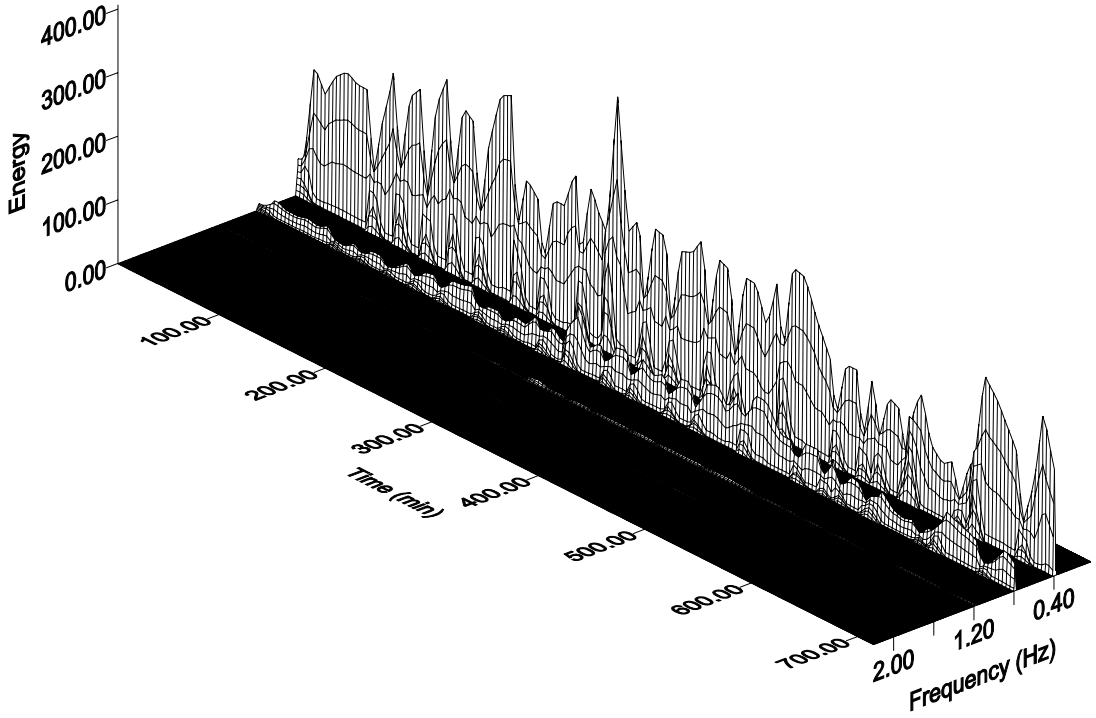

Figure E.3 DSTI02 Incident wave spectra

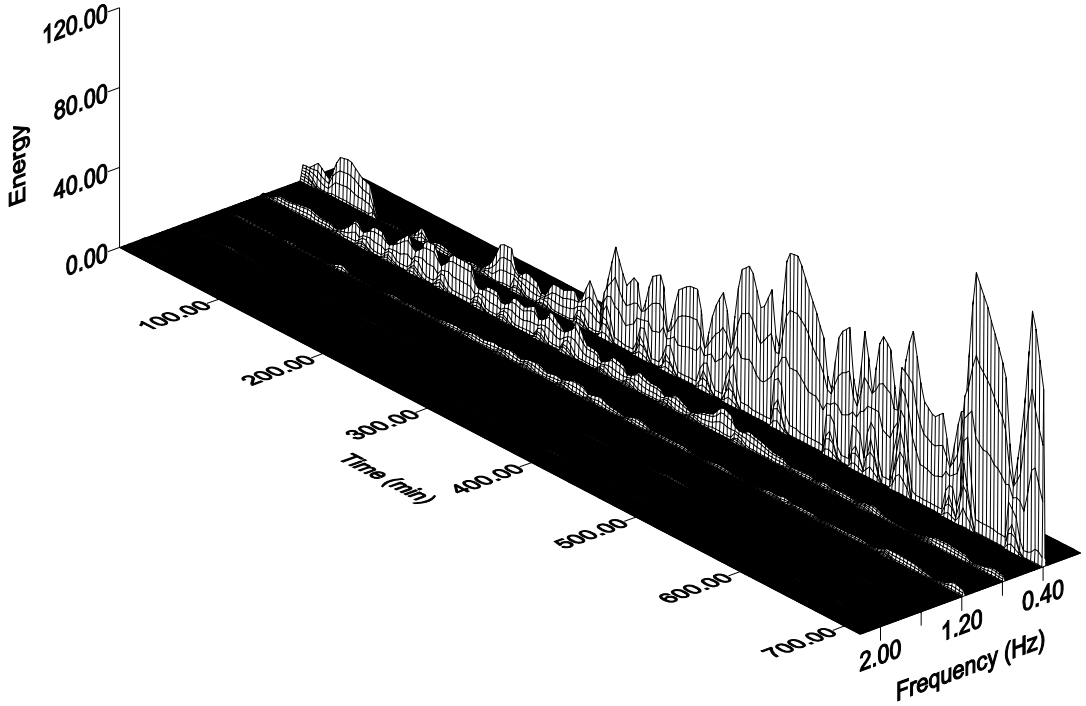

Figure E.4 DSTI02 Reflected wave spectra

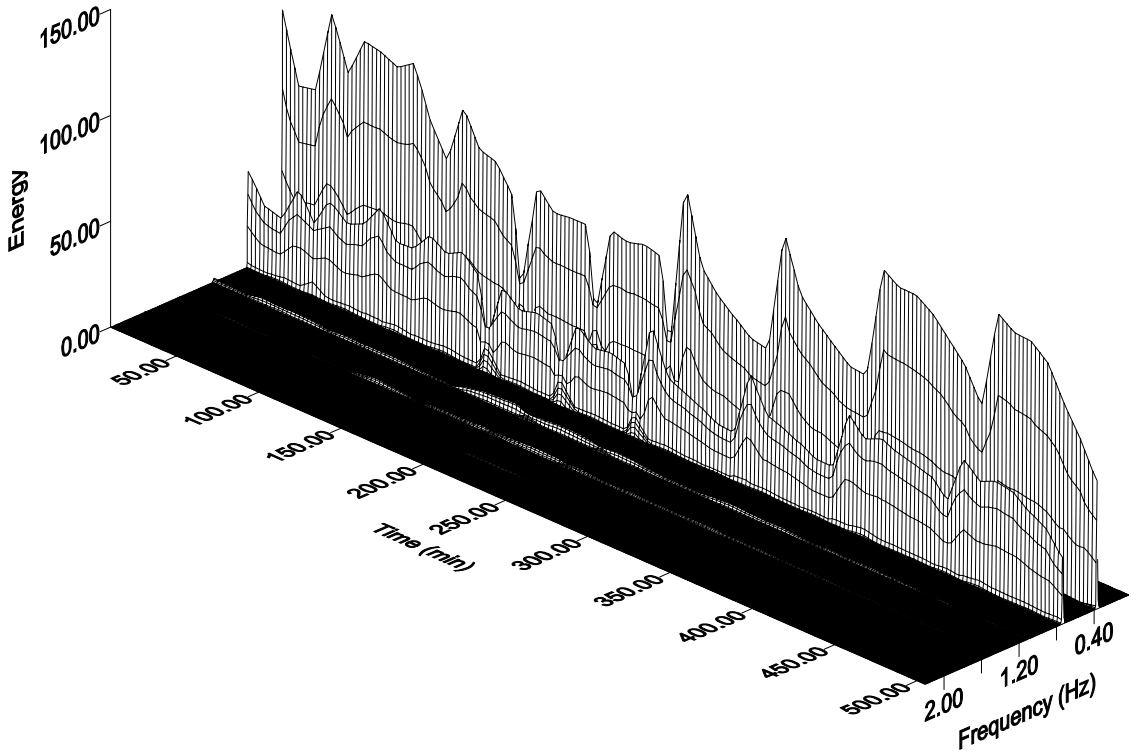

Figure E.5 DSTI03 Incident wave spectra

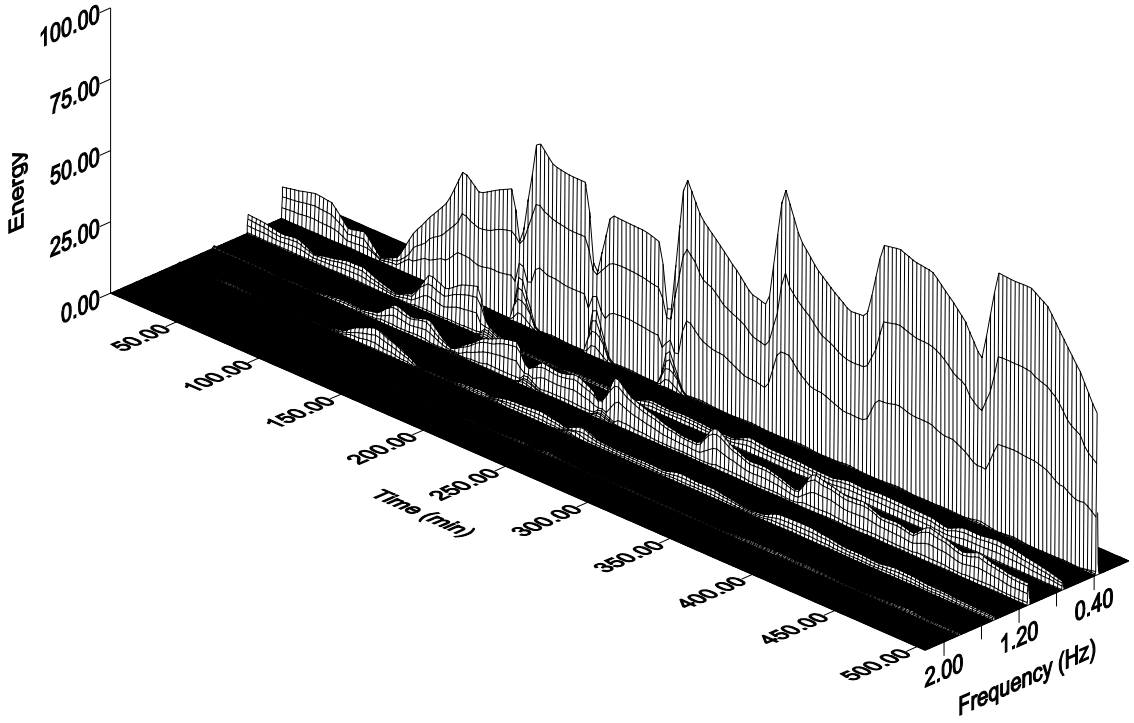

Figure E.6 DSTI03 Reflected wave spectra

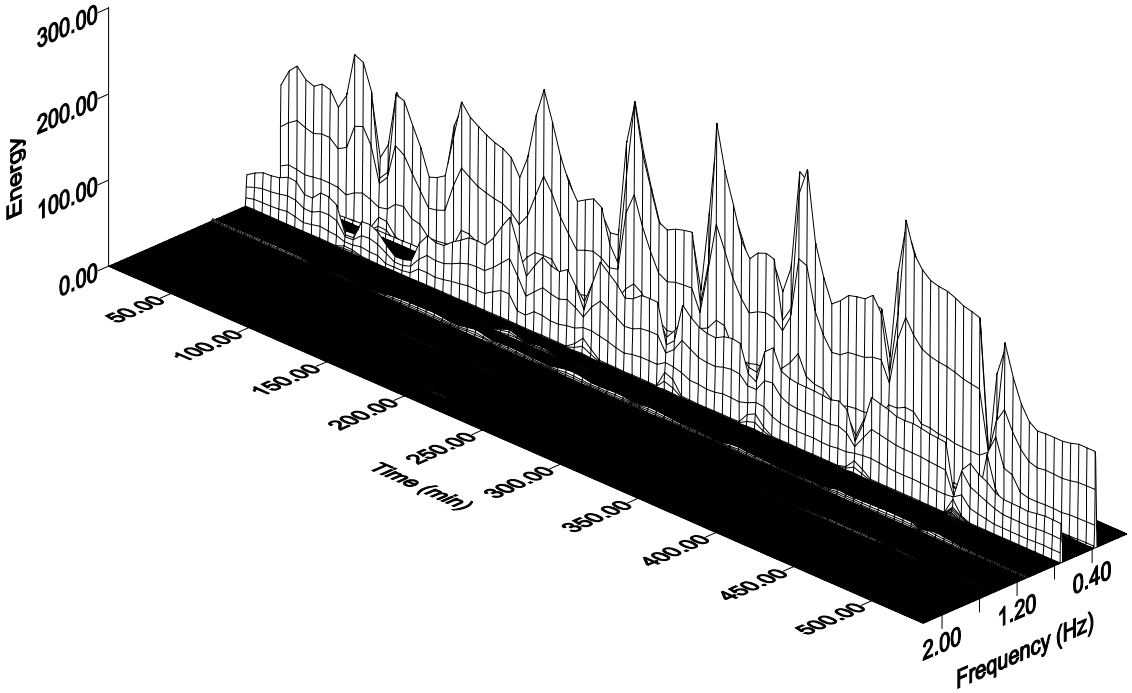

Figure E.7 DSTI04 Incident wave spectra

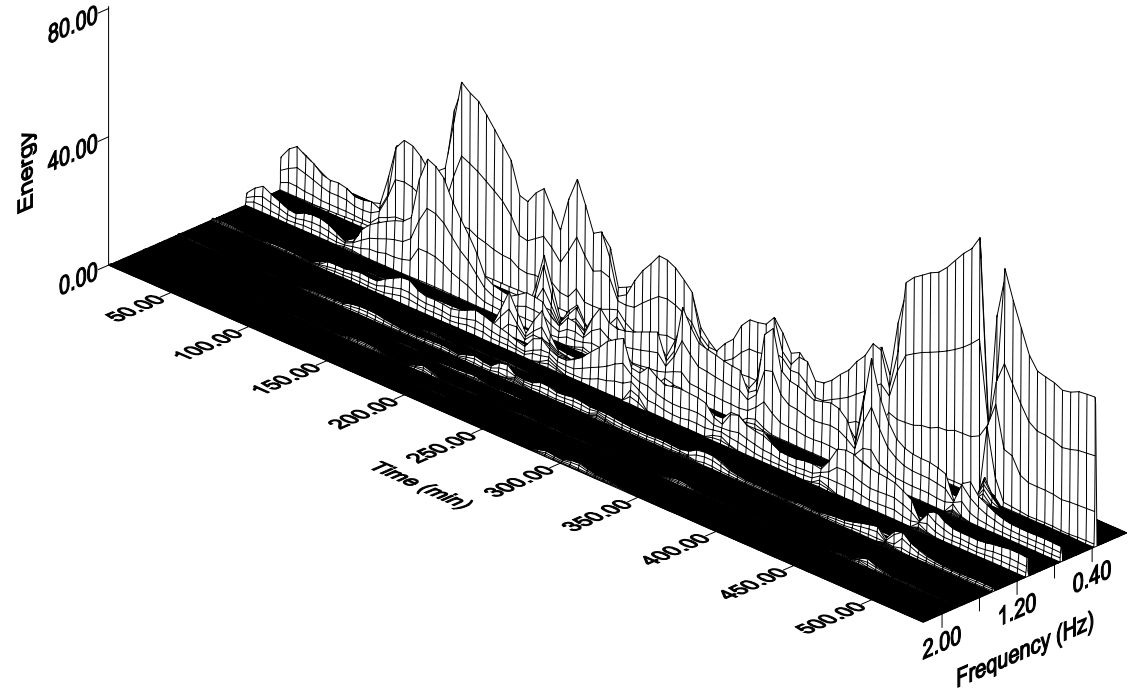

Figure E.8 DSTI04 Reflected wave spectra

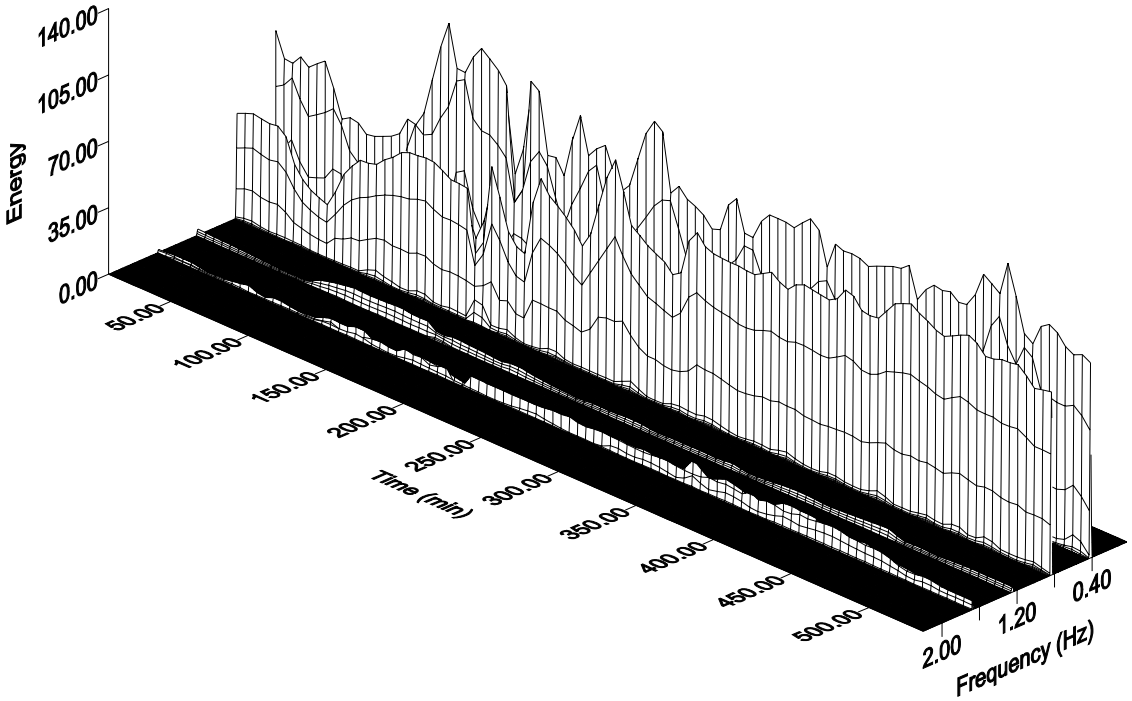

Figure E.9 DSTI05 Incident wave spectra

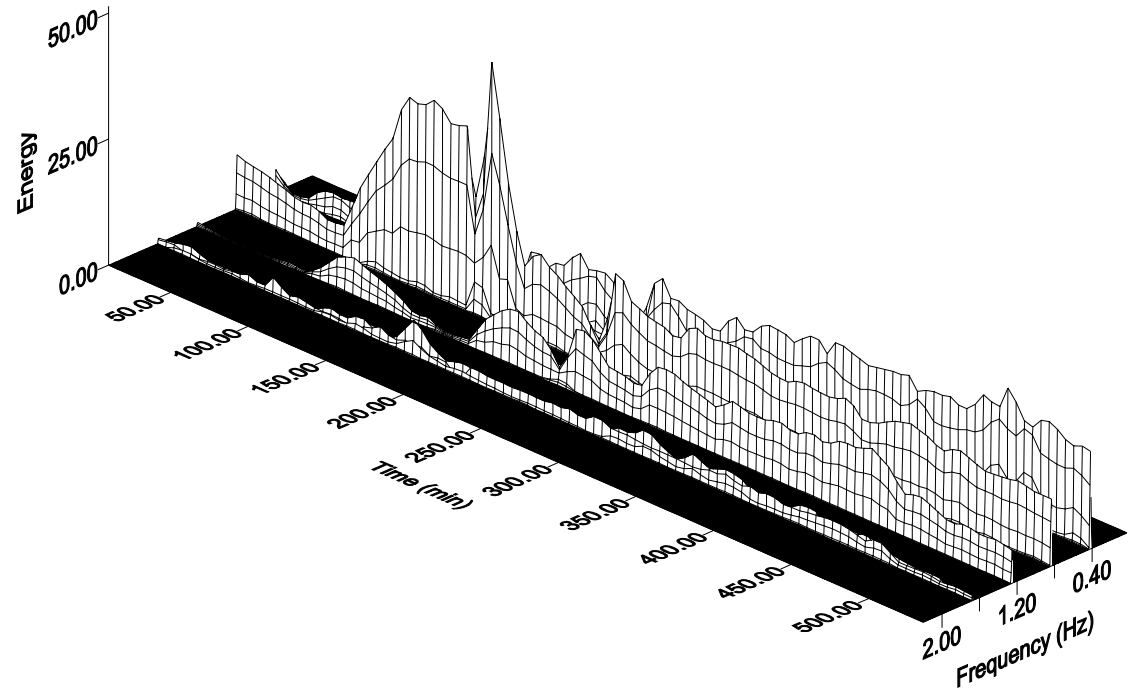

Figure E.10 DSTI05 Reflected wave spectra

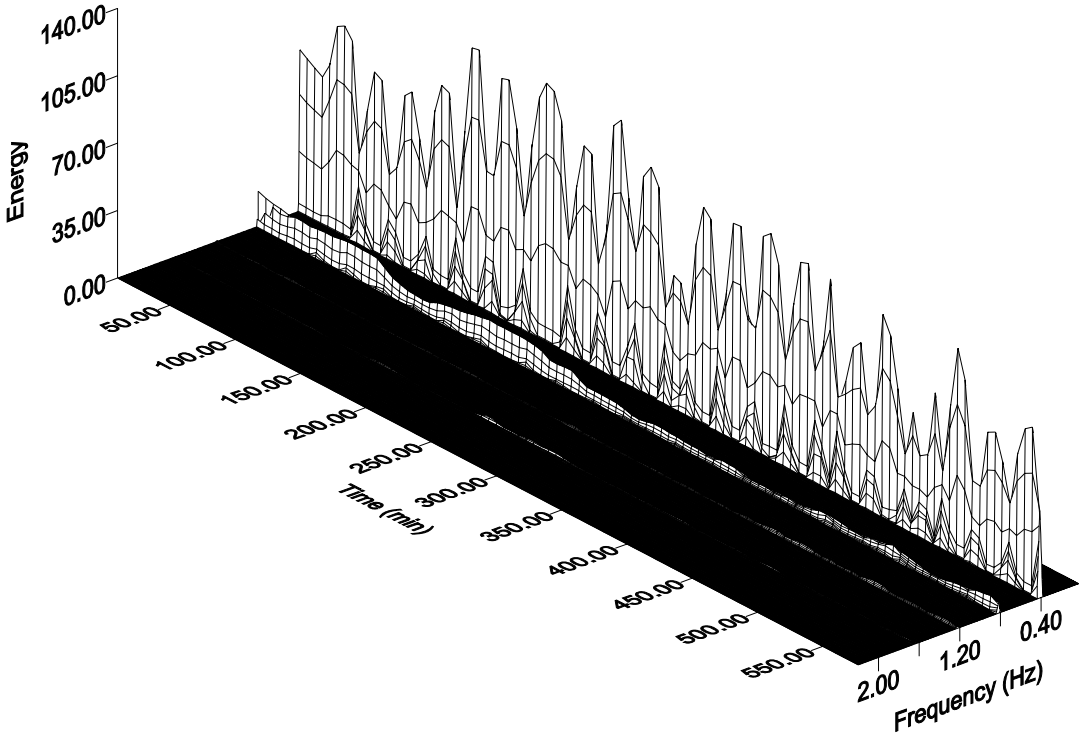

Figure E.11 DSTI06 Incident wave spectra

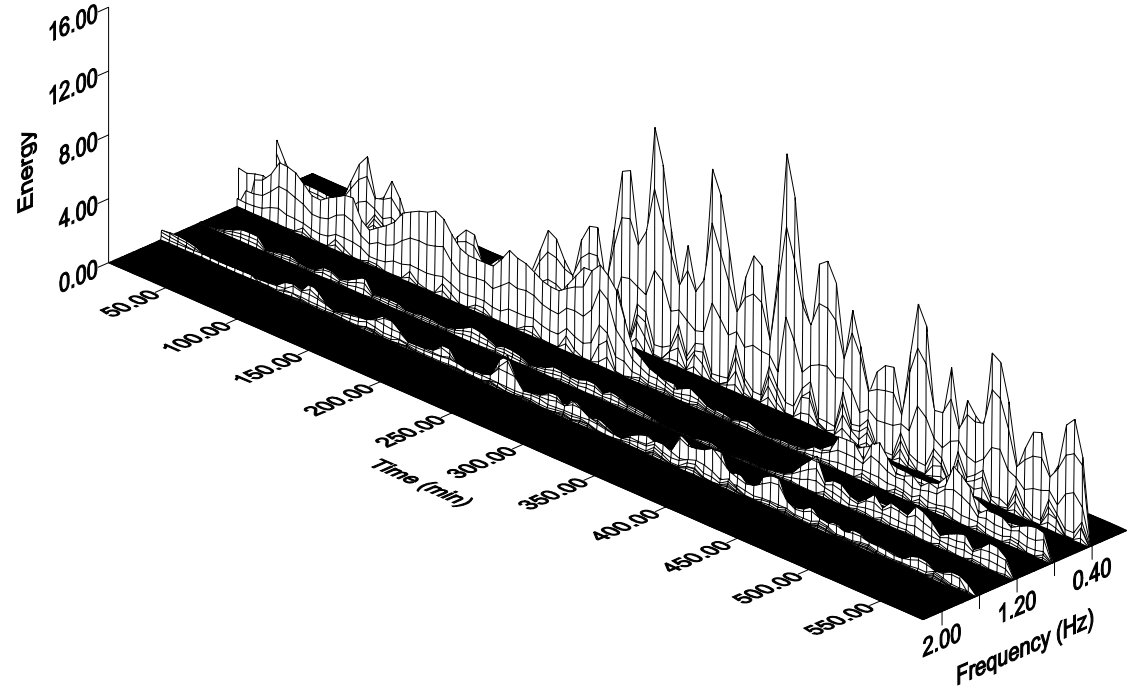

Figure E.12 DSTI06 Reflected wave spectra

Appendix F. Reflection Coefficient of Higher Harmonics

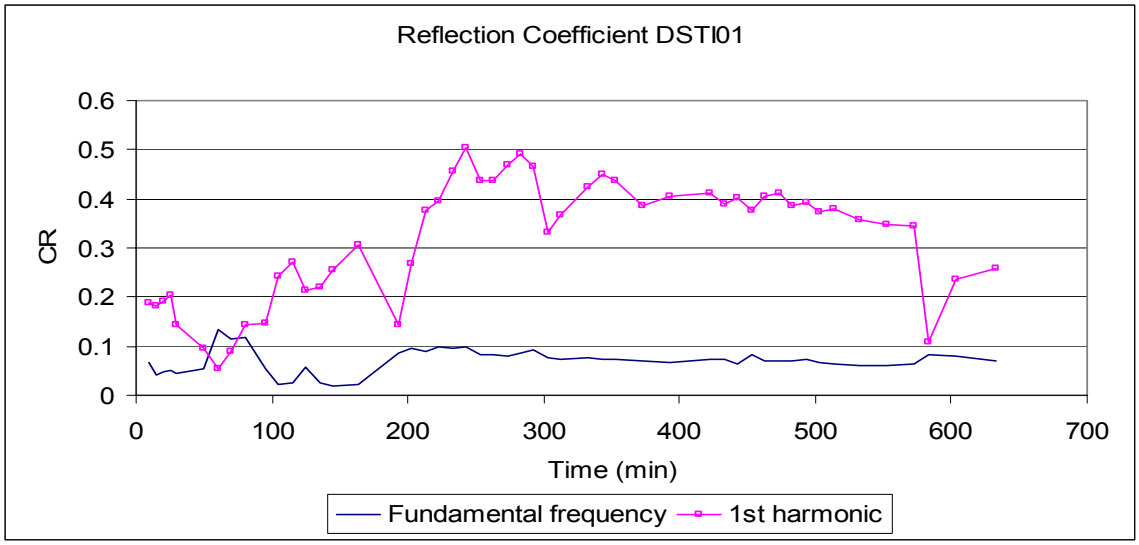

Figure F.1 Reflection coefficient of DSTI01

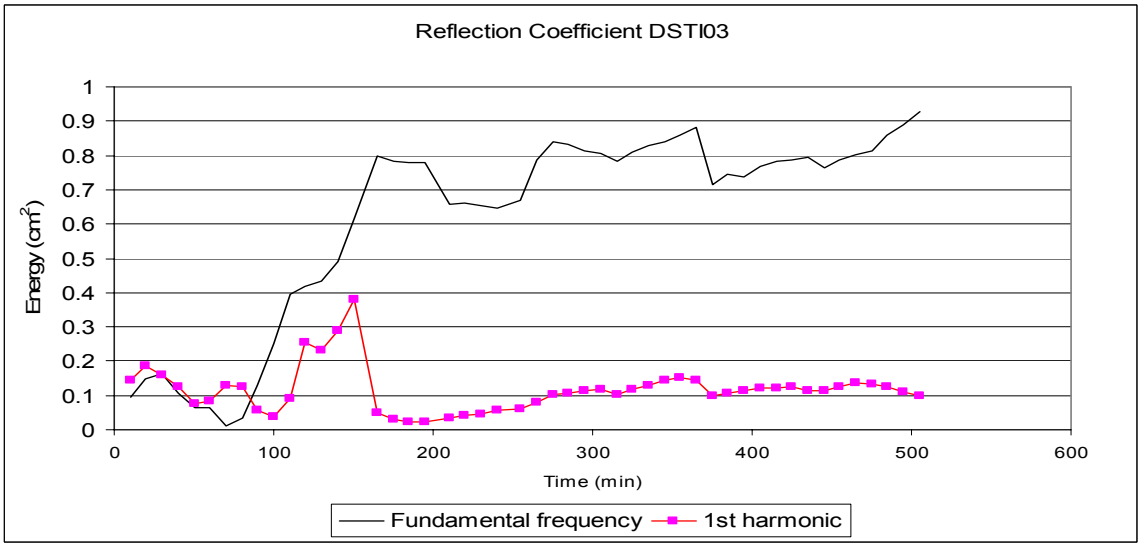

Figure F.2 Reflection coefficient of DSTI03

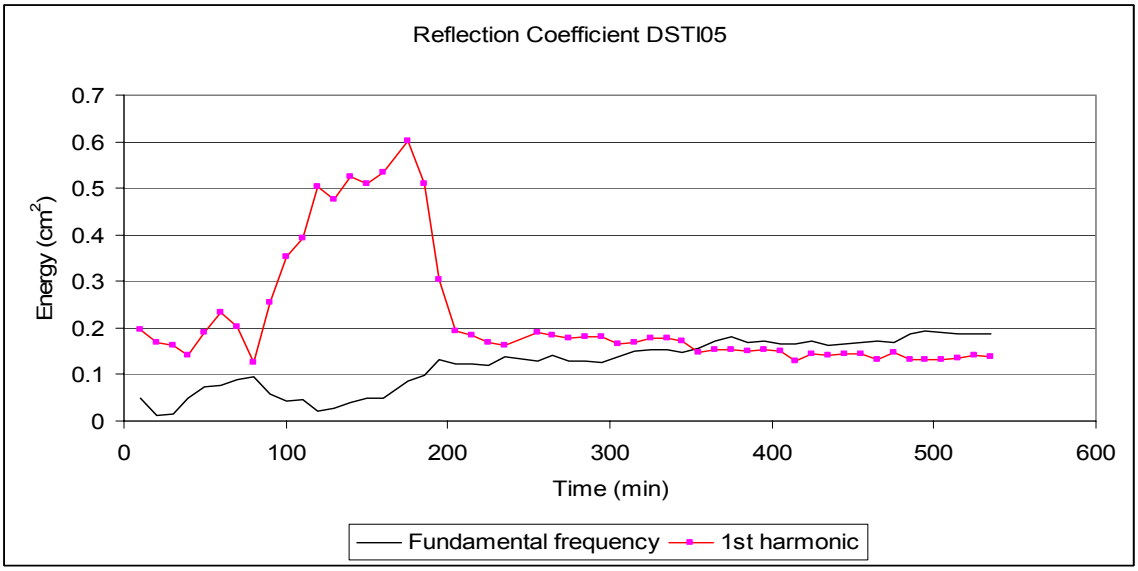

Figure F.3 Reflection coefficient of DSTI05

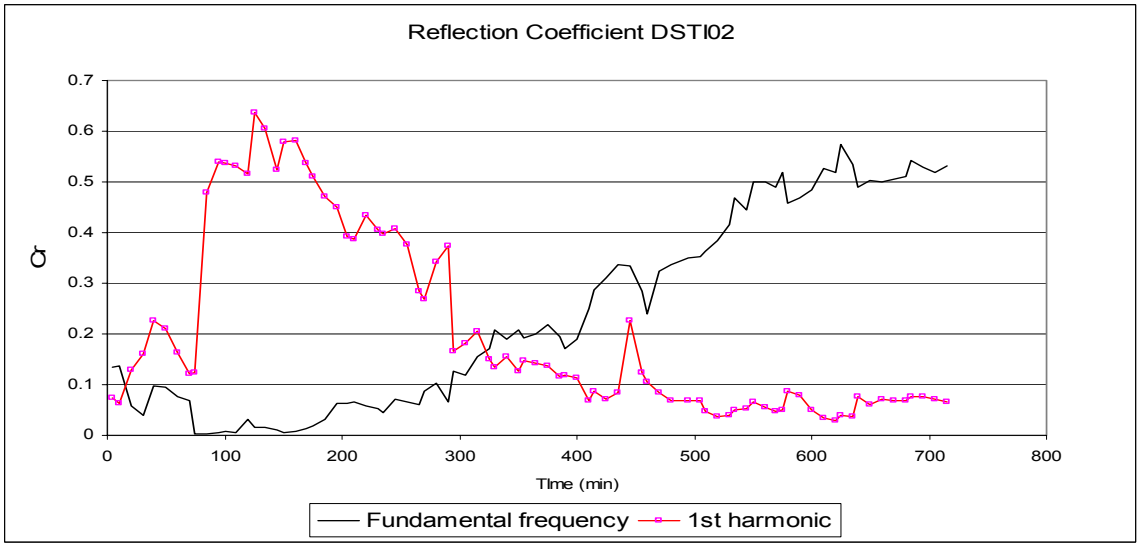

Figure F.4 Reflection coefficient of DSTI02

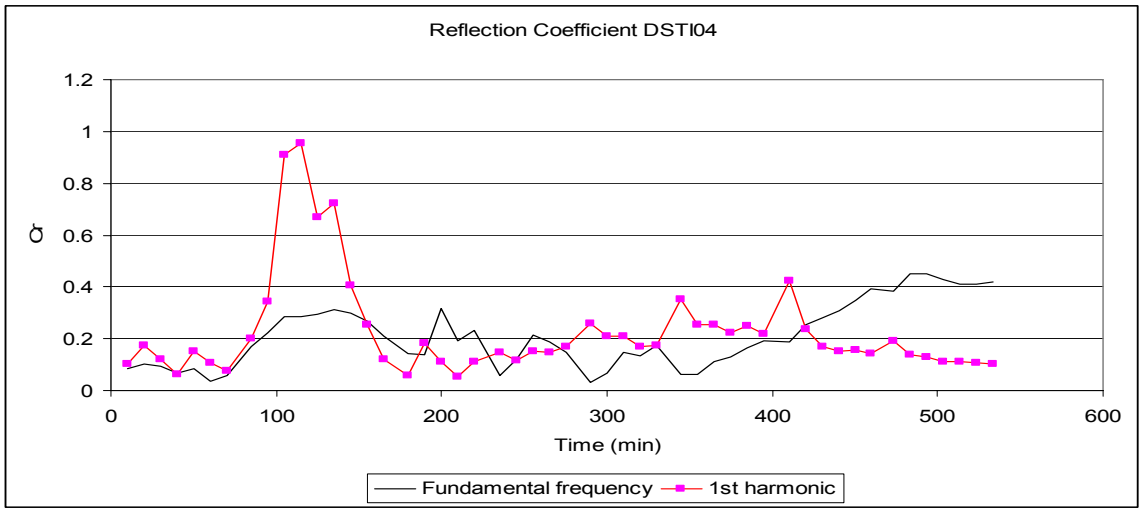

Figure F.5 Reflection coefficient of DSTI04

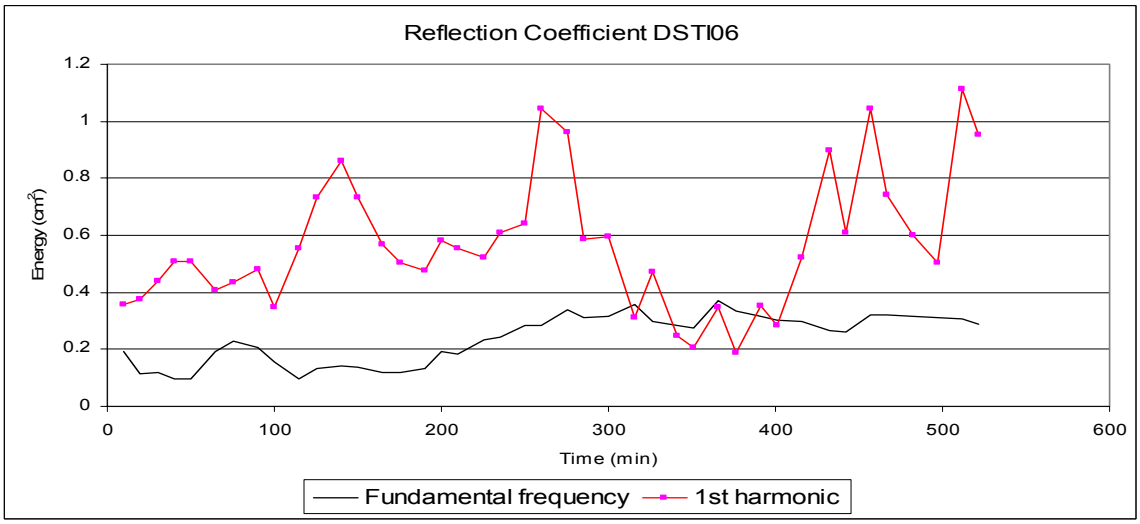

Figure F.6 Reflection coefficient of DSTI06

Appendix G. Calculated Bottom Velocities

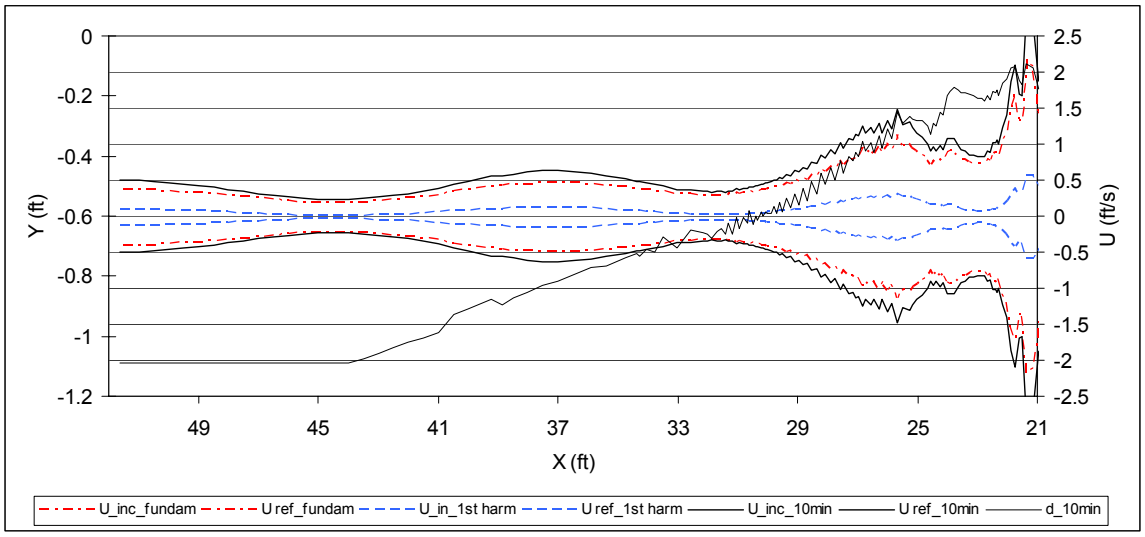

Figure G.1 Calculated Bottom velocities for DSTi01 at t = 10 min

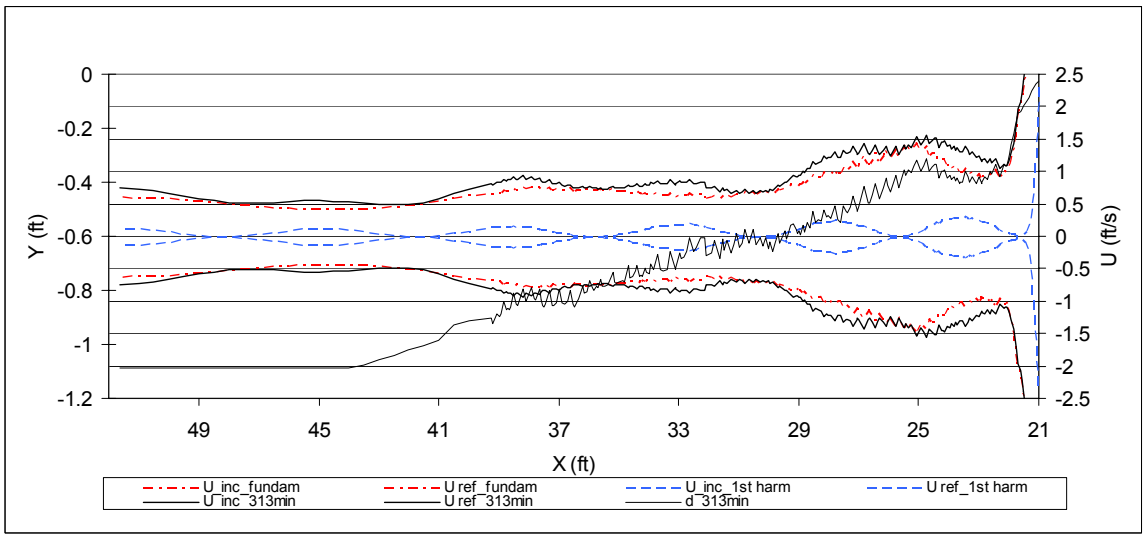

Figure G.2 Calculated Bottom velocities for DSTi01 at t = 313 min

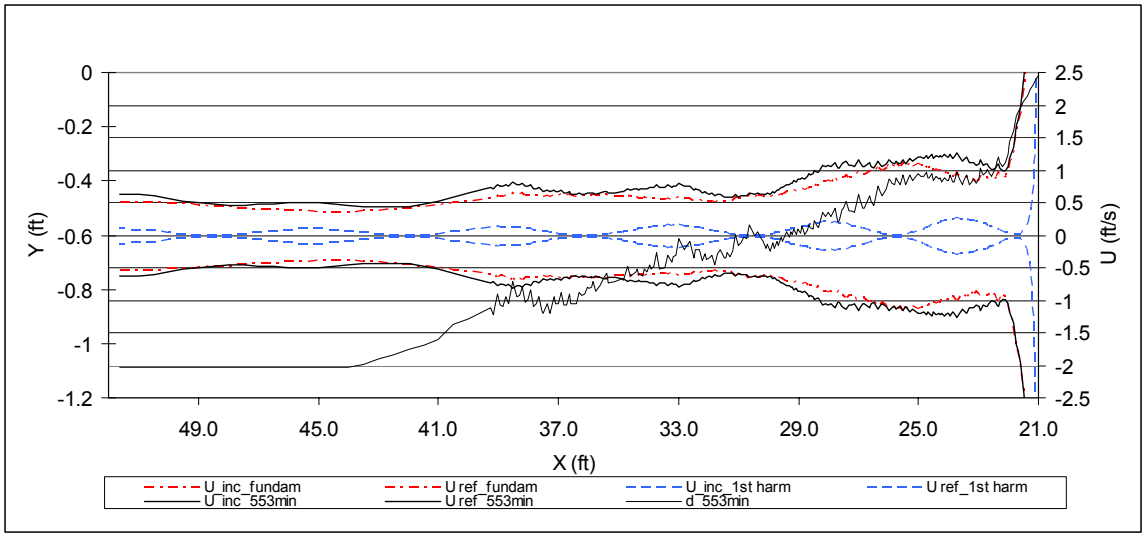

Figure G.3 Calculated Bottom velocities for DSTi01 at t = 533 min

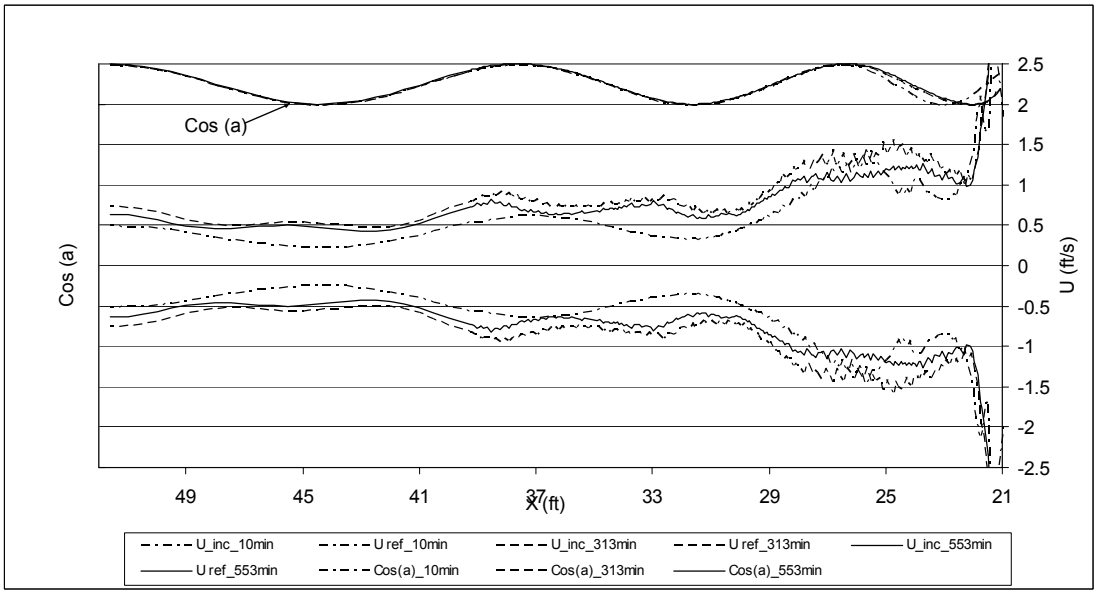

Figure G.4 Calculated bottom velocities and cosine of phase angles, DSTi01

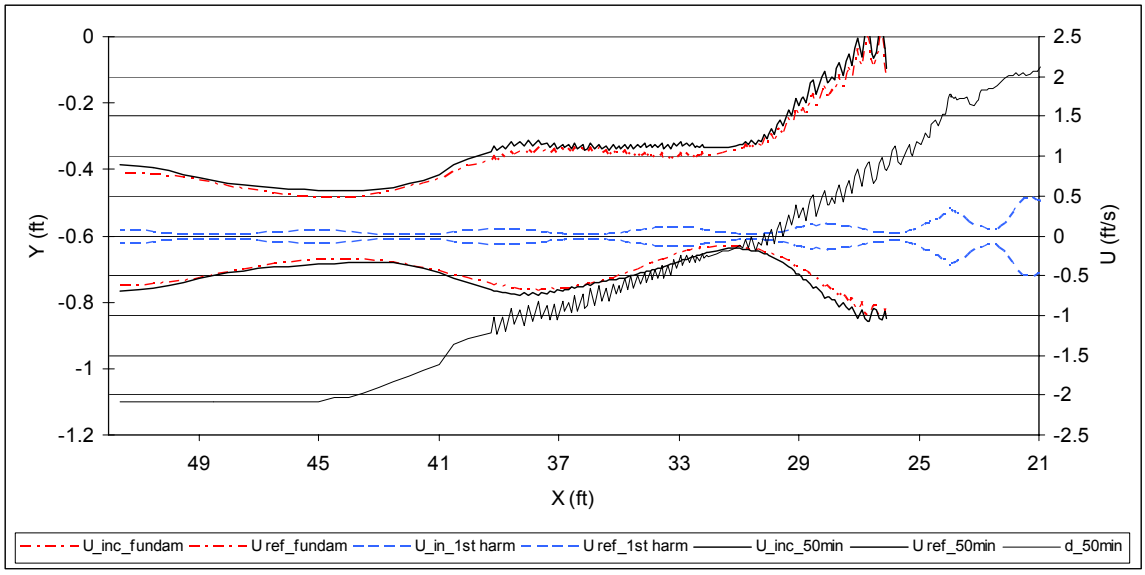

Figure G.5 Calculated Bottom velocities for DSTi02 at t = 50 min

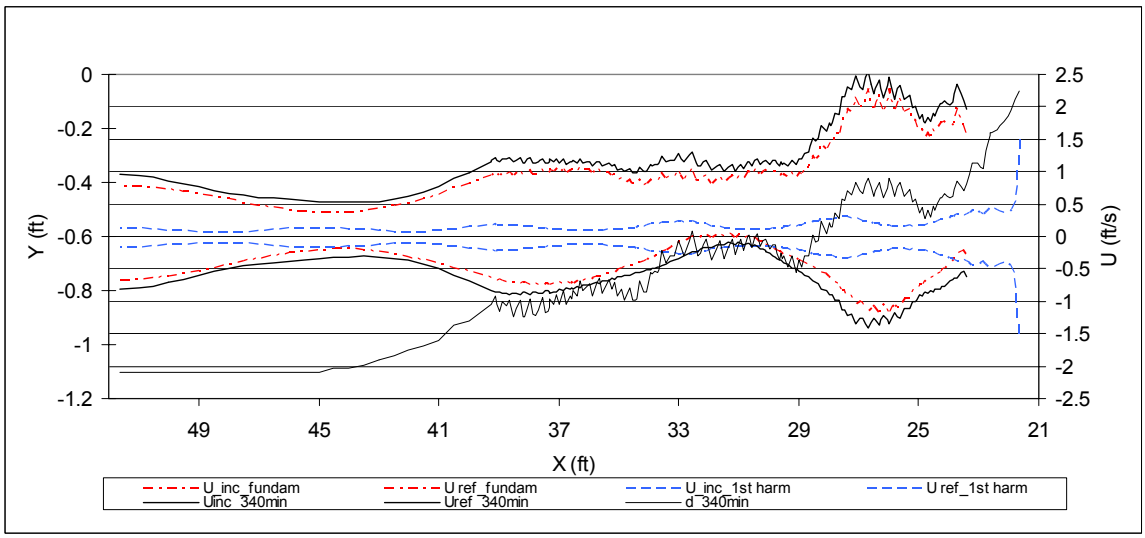

Figure G.6 Calculated Bottom velocities for DSTi02 at t = 340 min

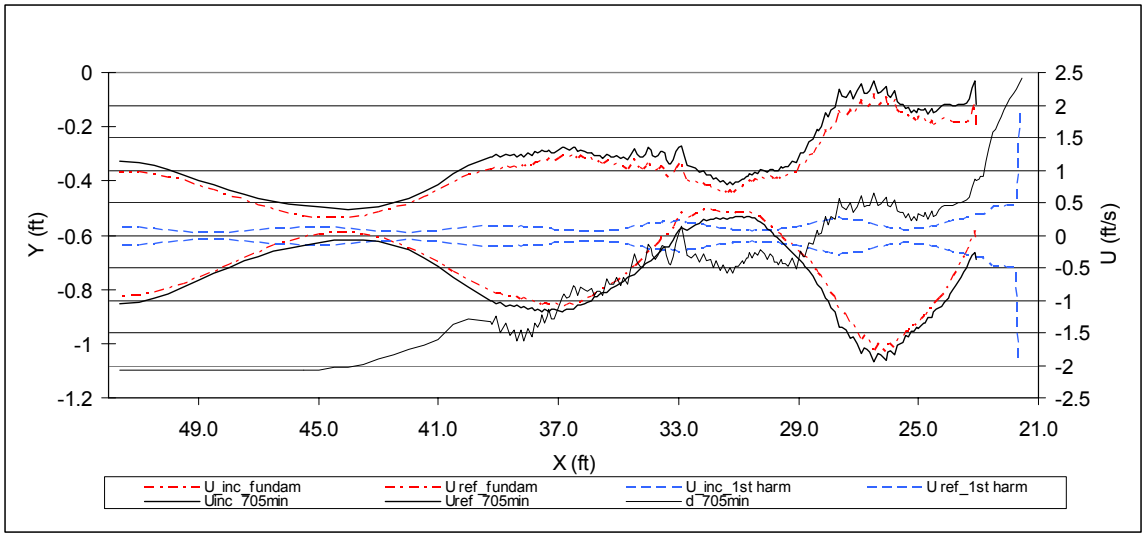

Figure G.7 Calculated Bottom velocities for DSTi02 at t = 705 min

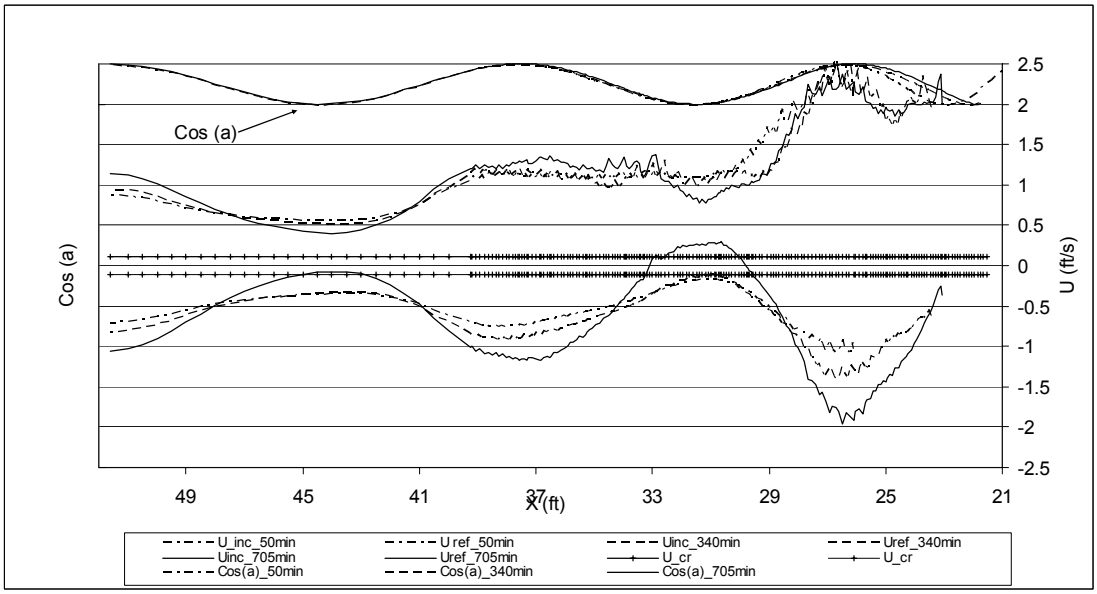

Figure G.8 Calculated bottom velocities and cosine of phase angles, DSTi02

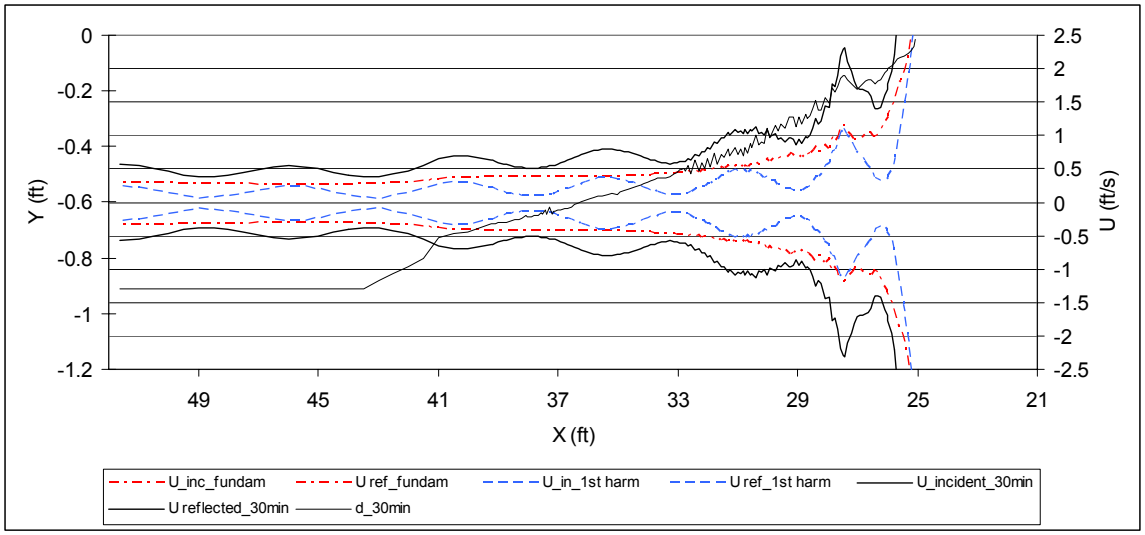

Figure G.9 Calculated Bottom velocities for DSTi05 at t = 30 min

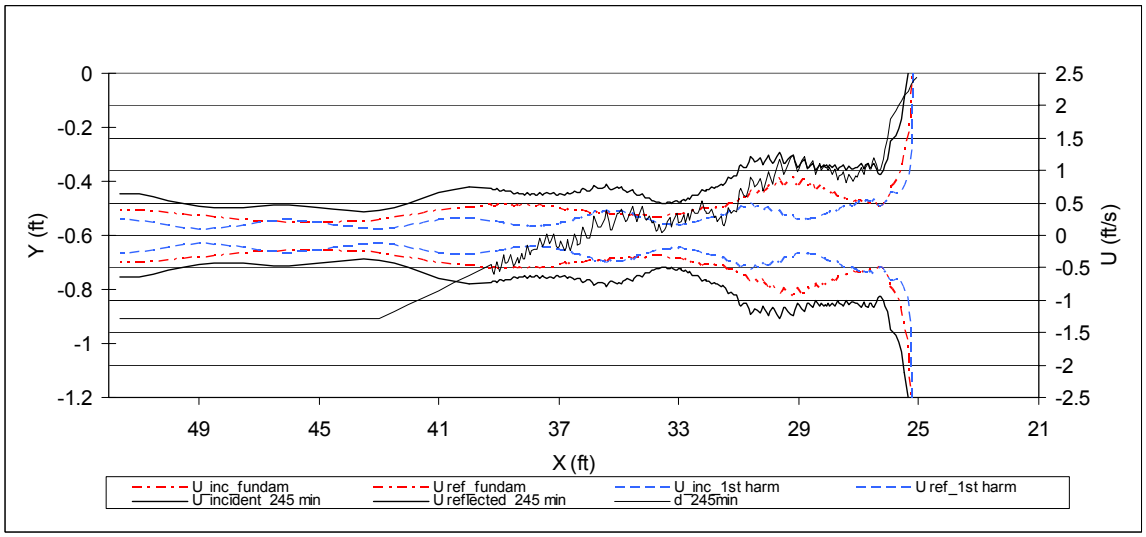

Figure G.10 Calculated Bottom velocities for DSTi05 at t = 245 min

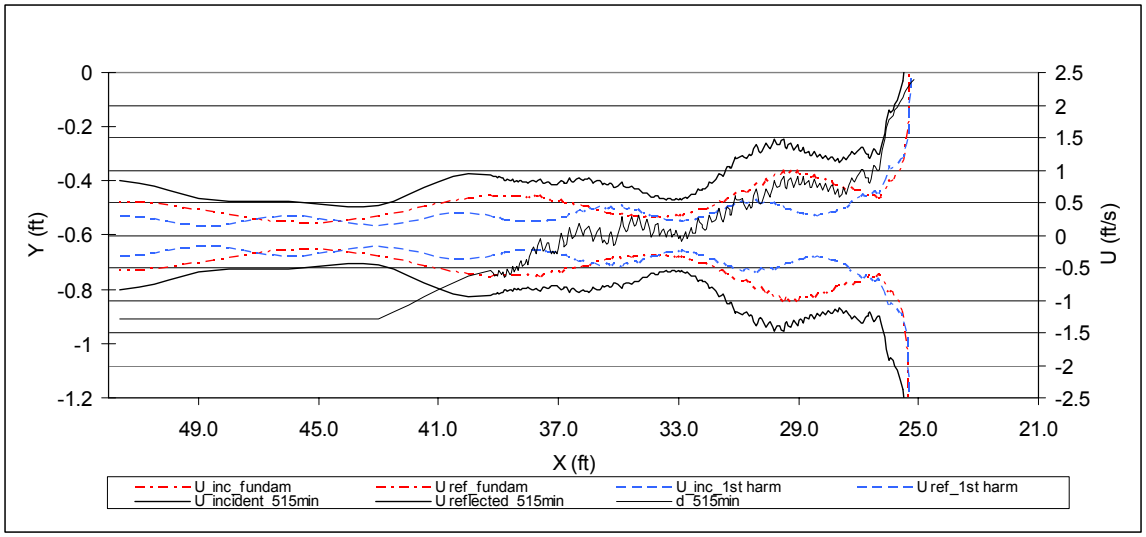

Figure G.11 Calculated Bottom velocities for DSTi05 at t = 515 min

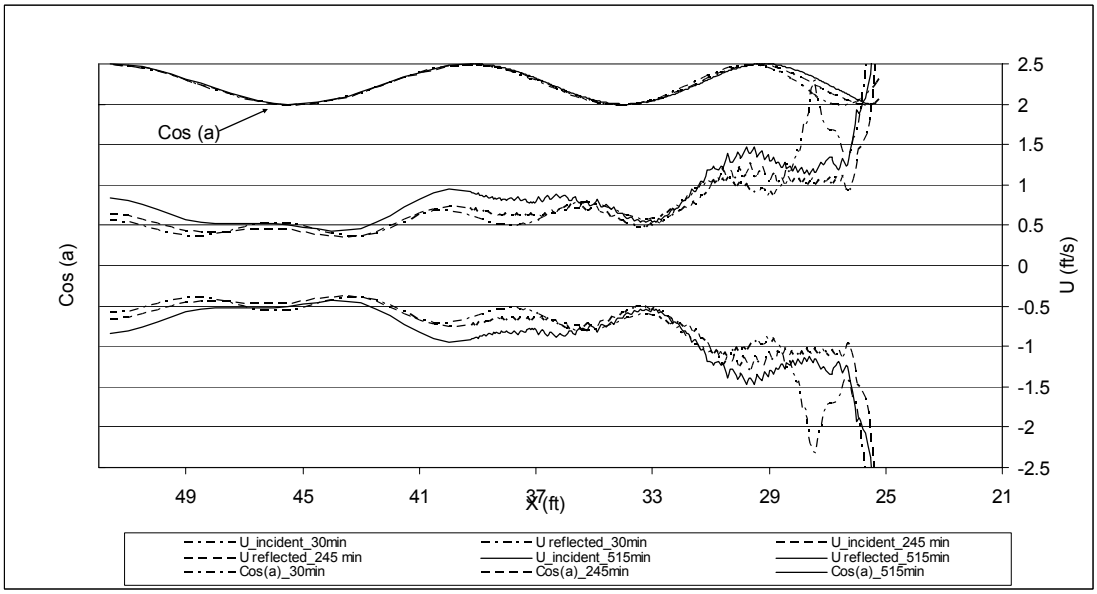

Figure G.12 Calculated bottom velocities and cosine of phase angles, DSTi05

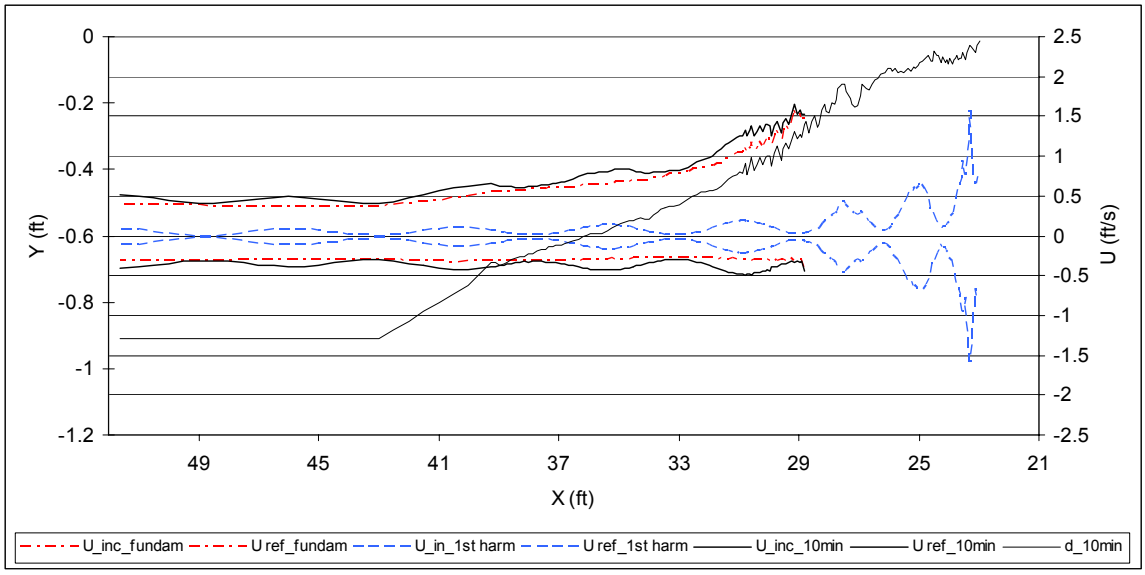

Figure G.13 Calculated Bottom velocities for DSTi06 at t = 10 min

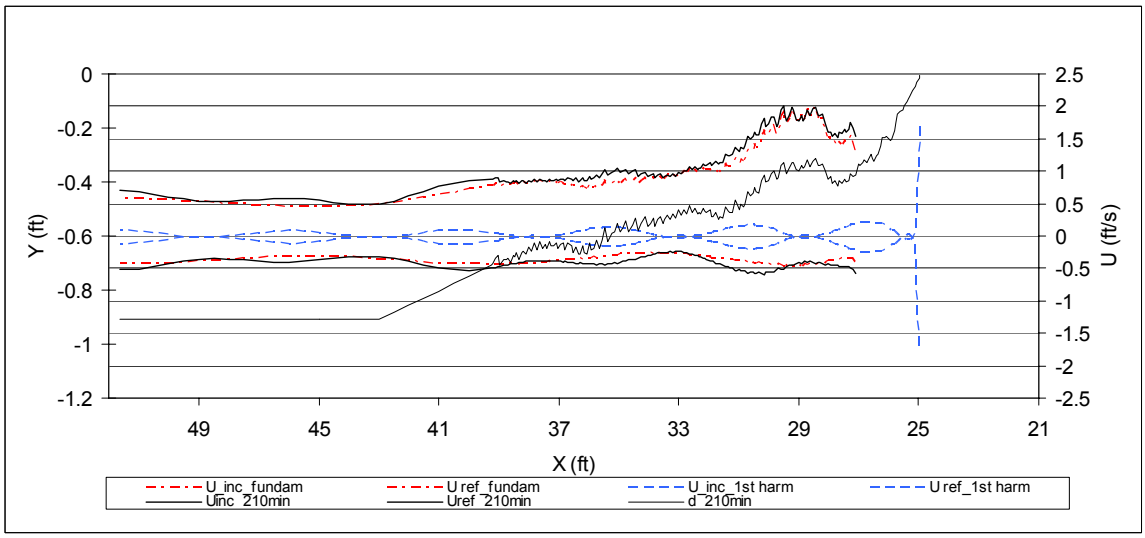

Figure G.14 Calculated Bottom velocities for DSTi06 at t = 210 min

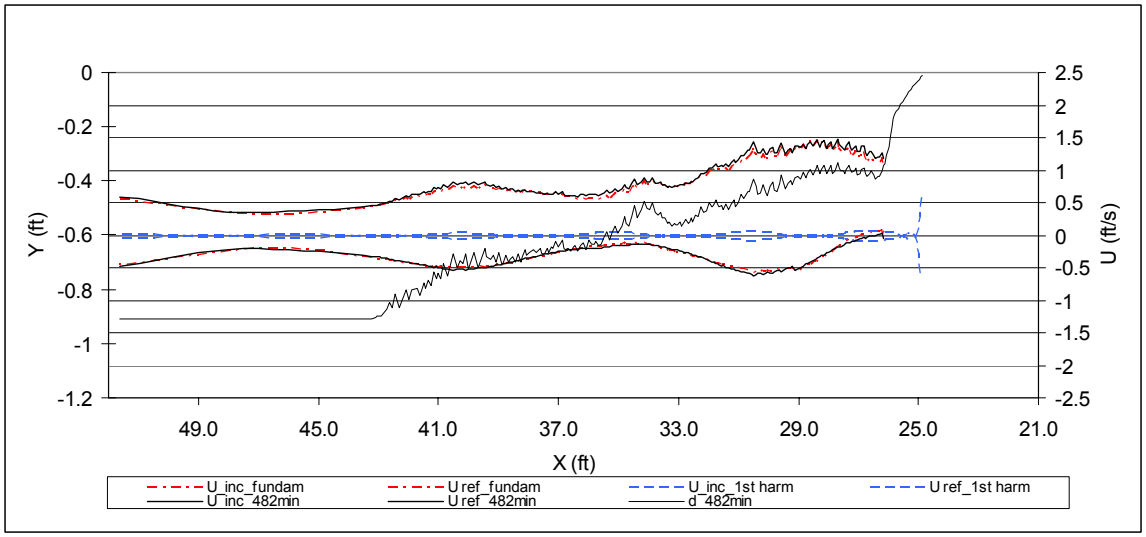

Figure G.15 Calculated Bottom velocities for DSTi06 at t = 482 min

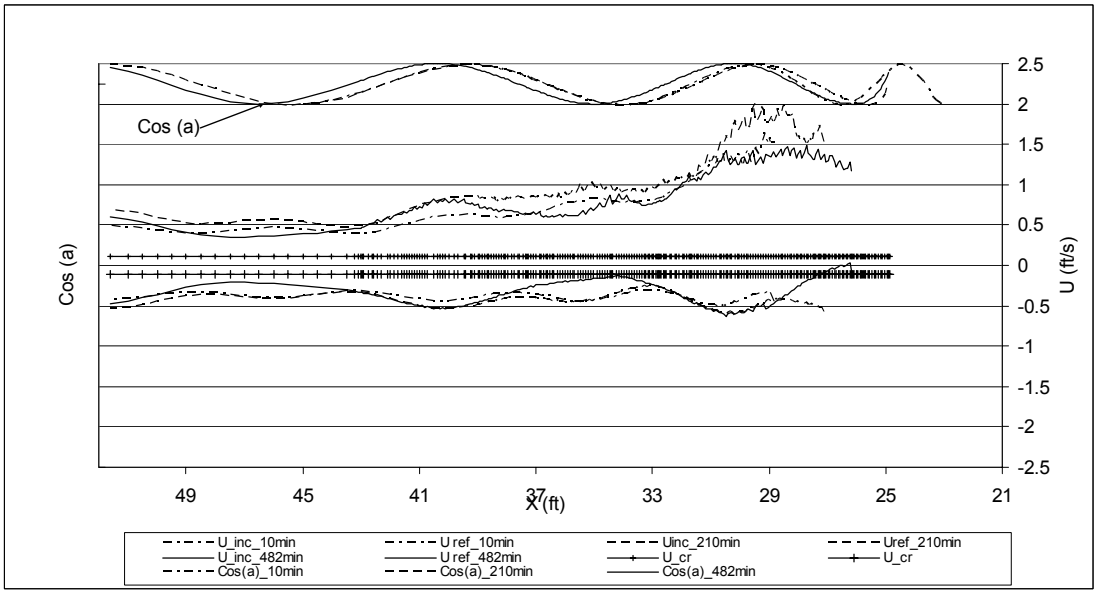

Figure G.16 Calculated bottom velocities and cosine of phase angles, DSTi06

Appendix H. Ripples

Ripple formation was observed and they were measured carefully. Ripples are formed in shallow water by wave oscillation. Sleath (1984) classified ripples based on their shape. His classification is shown in Figure H.1. Sleath called the ripples with sinuous shape and symmetrical in cross section and elongated in the direction of the crest as two dimensional vortex ripples. 2-D vortex ripples and rolling ripples are termed “regular ripples”. Ripples with asymmetrical shape and crests are not continuous in longitudinal axis are called three dimensional vortex ripples in Figure H.1. They are referred to as “irregular ripples” in this study. Examples of ripple shapes are shown in Figures H.2 and H.3 in photographs taken during DSTi06. They show regular and irregular ripples, respectively.

Ripples were formed shortly after the start of each test. Ripple development started initially at different parts of the profile. Regular ripples formed offshore (approximately beyond 30 ft on the profile) and irregular ripples formed onshore first. As the profile evolved, irregular ripples become regular ripples. For DSTi03 and DSTi04, irregular ripples formed partially on the profile at the first 20 minutes. After 30 minutes the profile was covered by irregular ripples onshore and by regular ripples beyond 30 ft. For DSTi05 and DSTi06, ripples were observed only on the sides of the profiles after 30 minutes of tests, but they formed in the middle line of the profile as tests continued. Profile was covered by ripples after 80 minutes for DSTi01 and DSTi02 test. Ripples changed their forms by duration of the tests according to profile changes. For example, DSTi04 (cnoidal wave test) at 30 minutes, ripples were observed all along the profile starting from 21.4 ft to the end of profile 39.3 ft. They were irregular ripples

on the onshore part of the profile. On the offshore part (beyond 32.3 ft seaward of the profile), they became regular ripples. As runs continued and the beach profile continued to evolve, regular ripples migrated onshore.

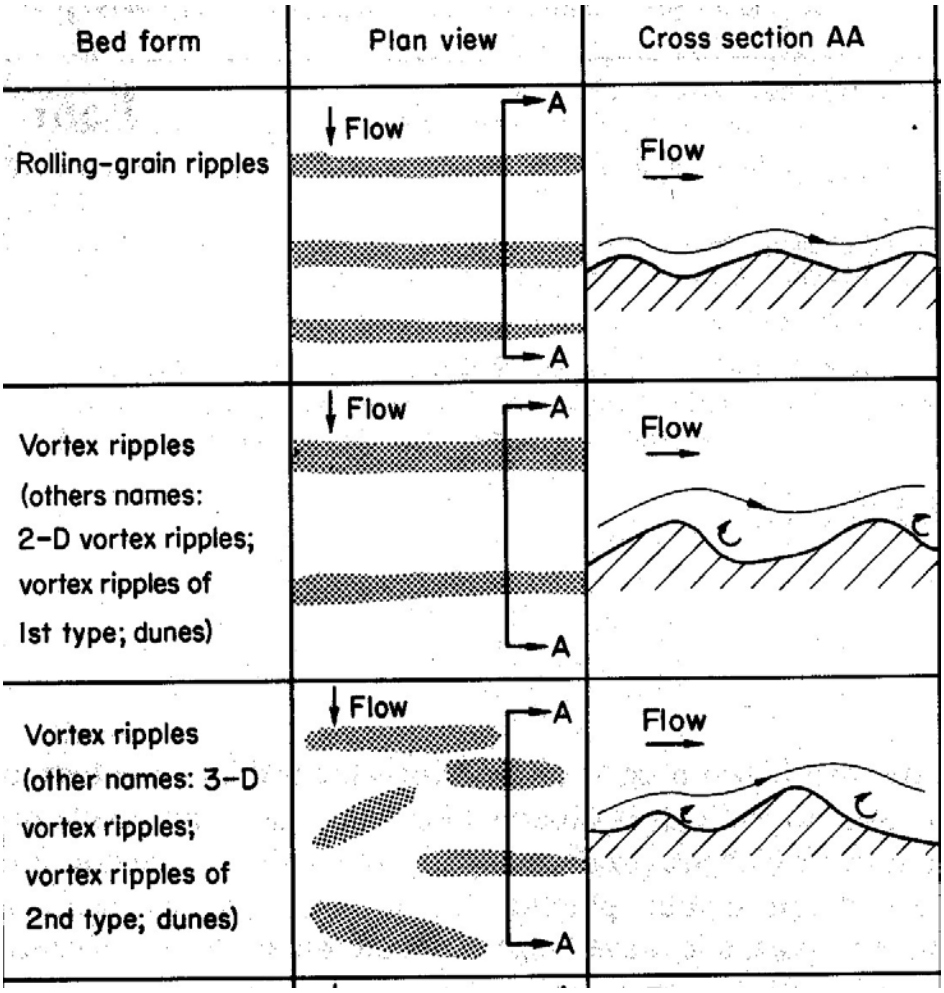

Figure H.1 Classifications of Ripples (Sleath, 1984)

Figure H.2 Regular ripples (DSTi06)

Figure H.3 Irregular ripples (DSTi06)

Appendix I. Beach Profile Evolution

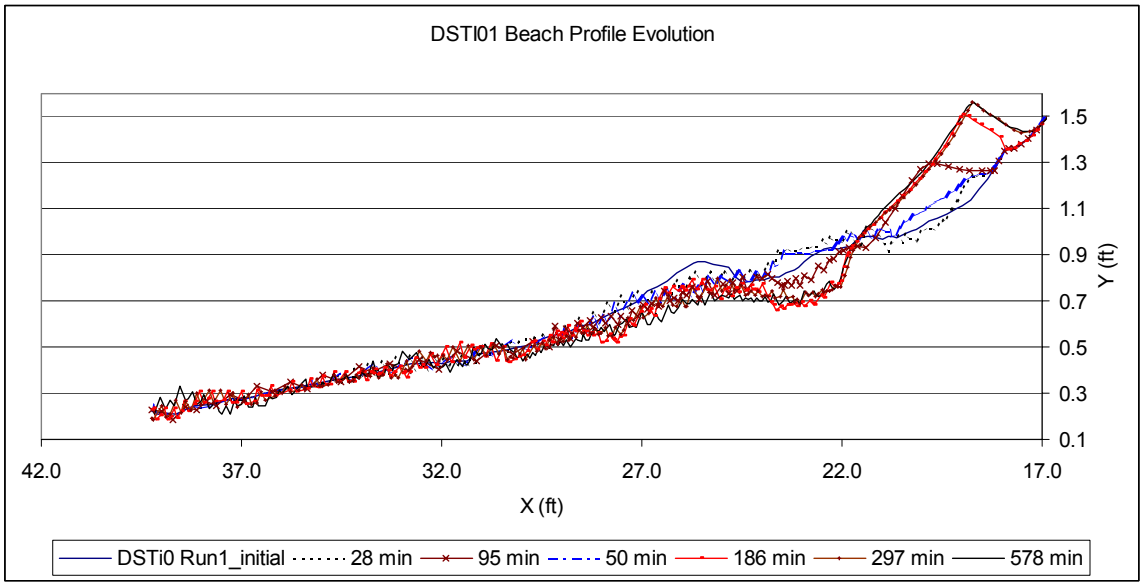

Figure I.1 DSTI01 Beach Profile Evolution

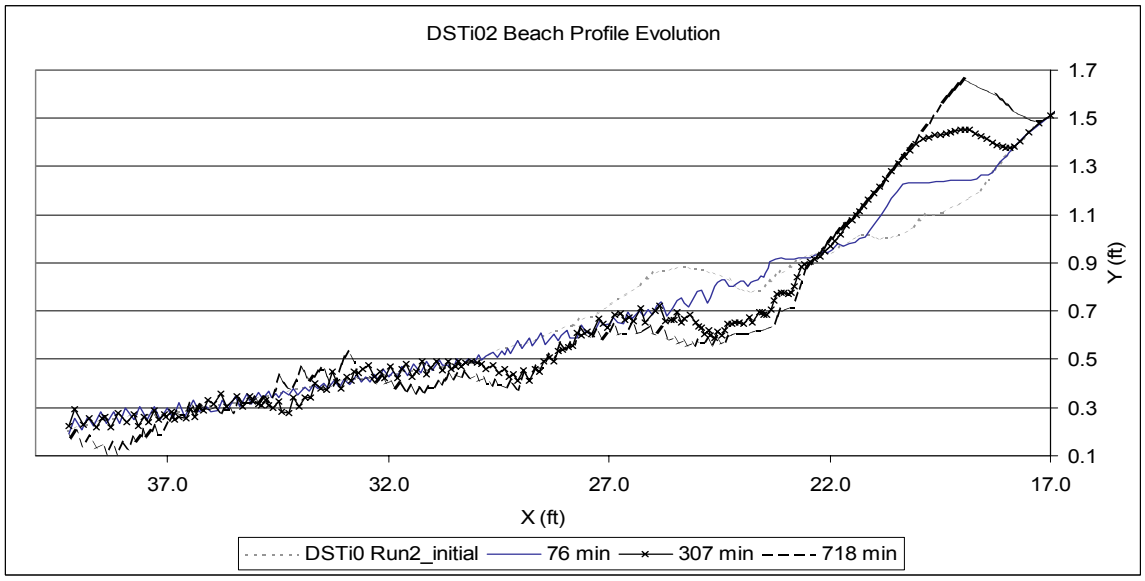

Figure I.2 DSTI02 Beach Profile Evolution

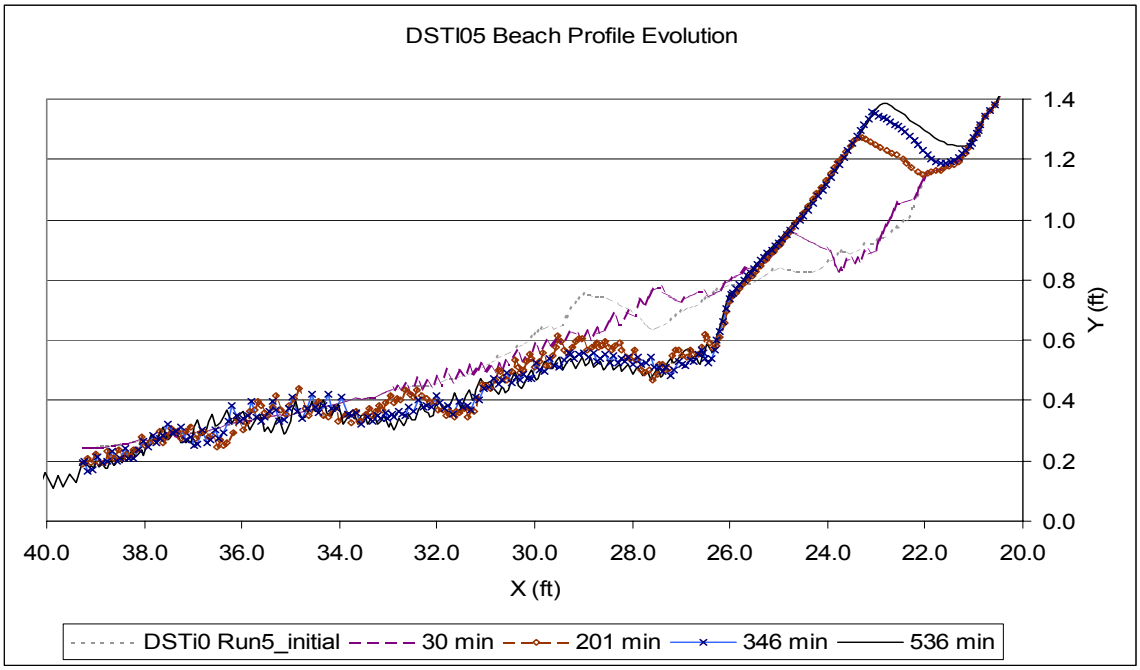

Figure I.3 DSTI05 Beach Profile Evolution

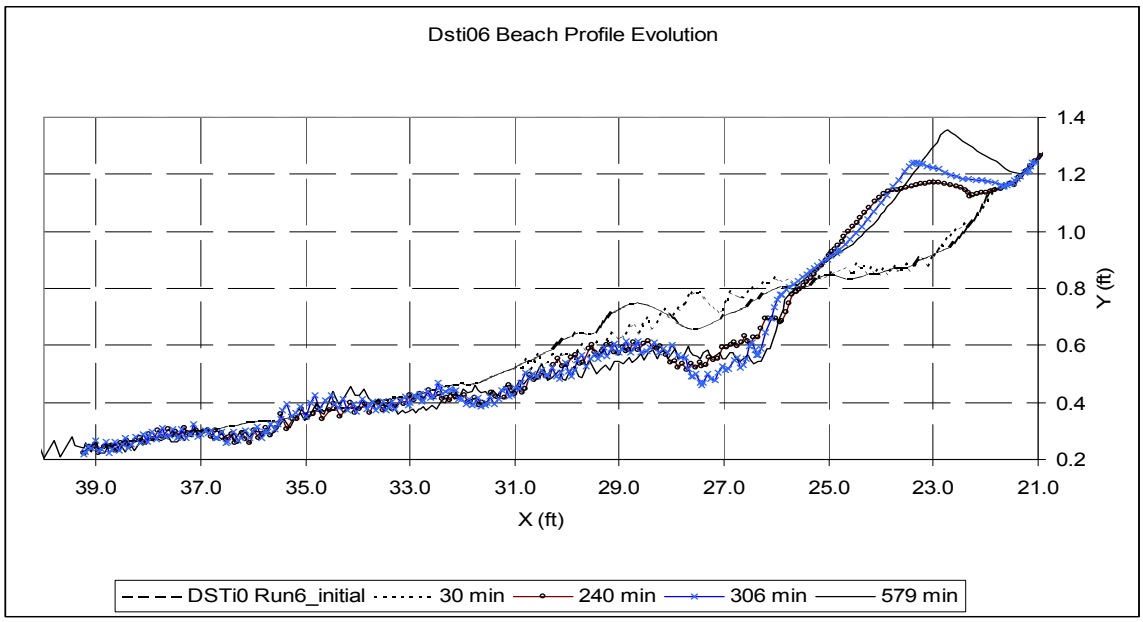

Figure I.4 DSTI06 Beach Profile Evolution

Appendix J. Phase Shifts

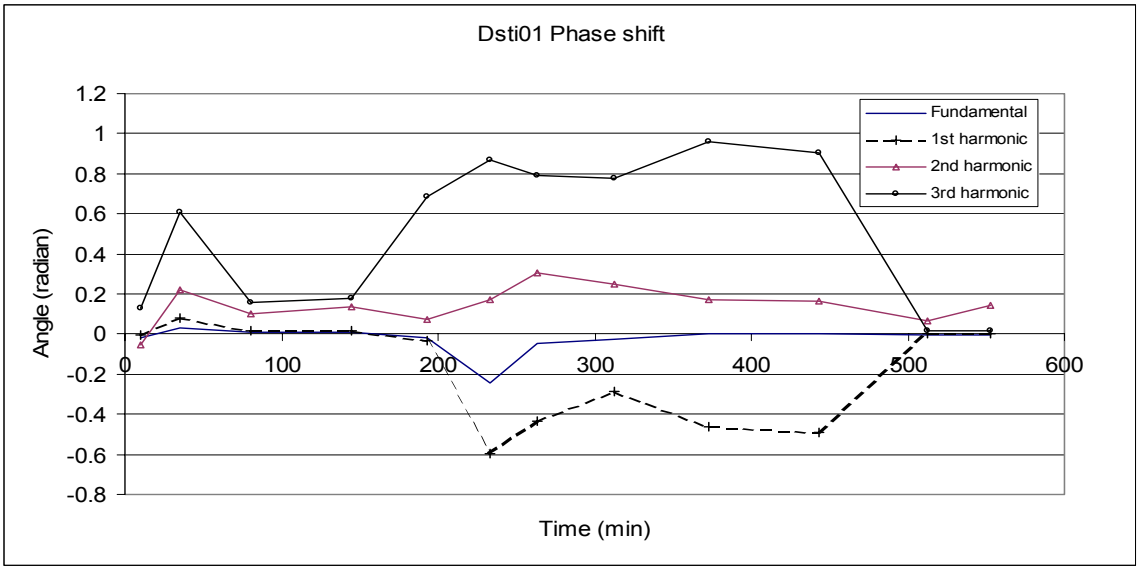

Figure J.1 Phase shift for DSTI01

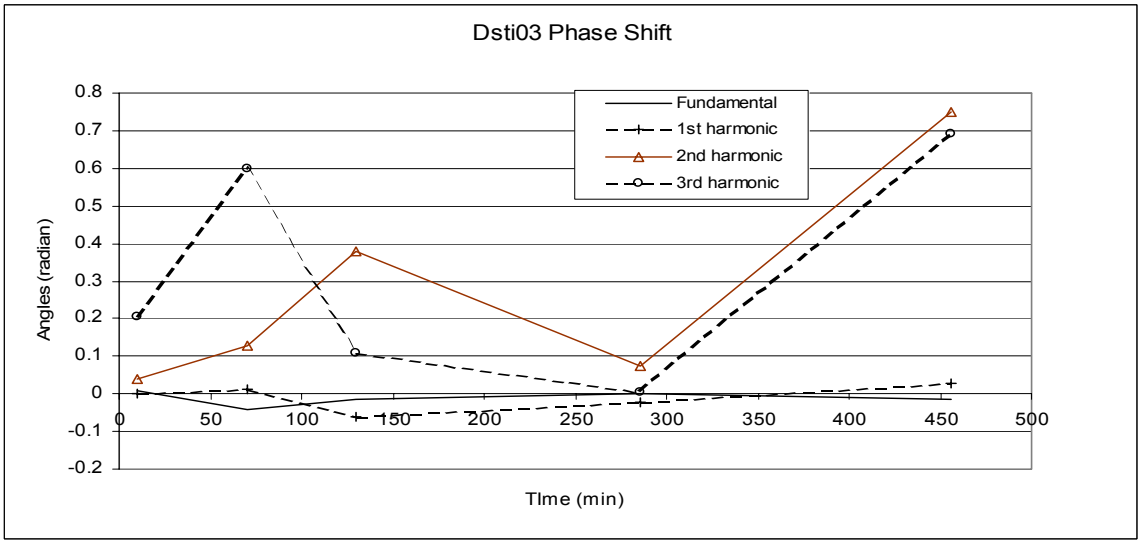

Figure J.2 Phase shift for DSTI03

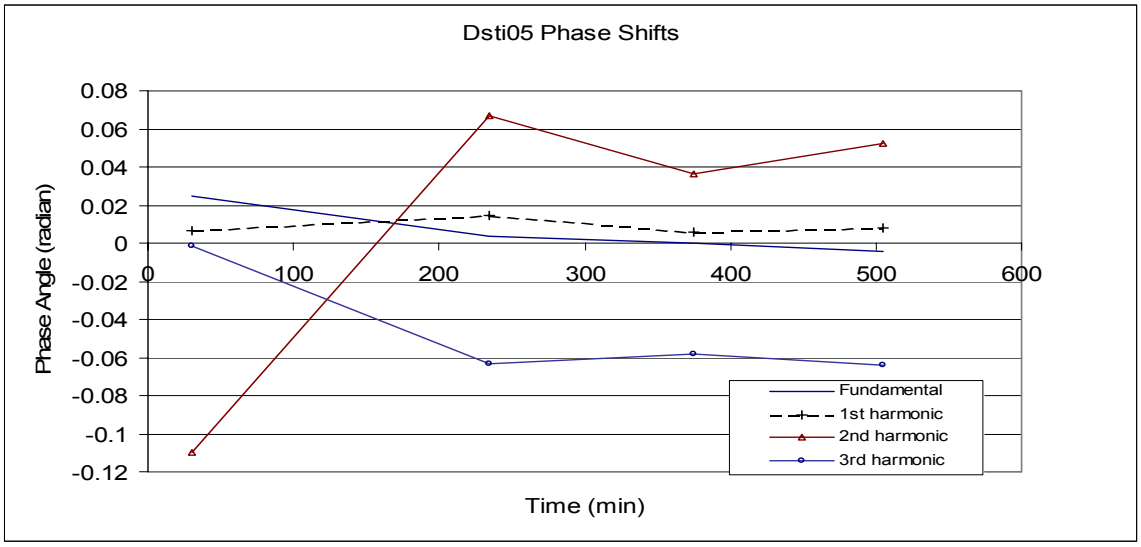

Figure J.3 Phase shift for DSTI05

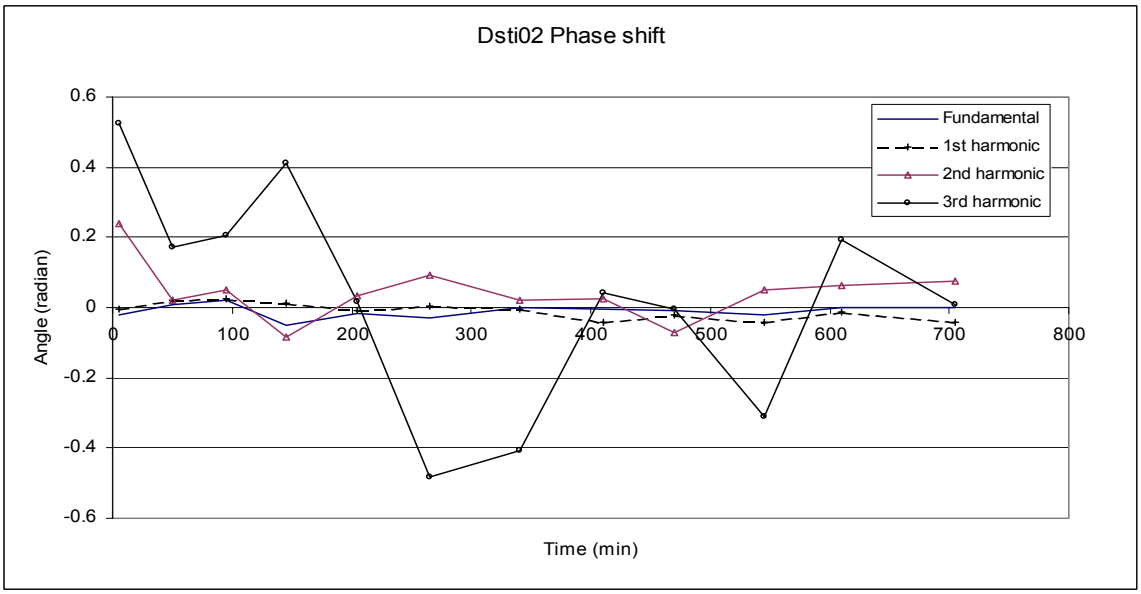

Figure J.4 Phase shift for DSTI02

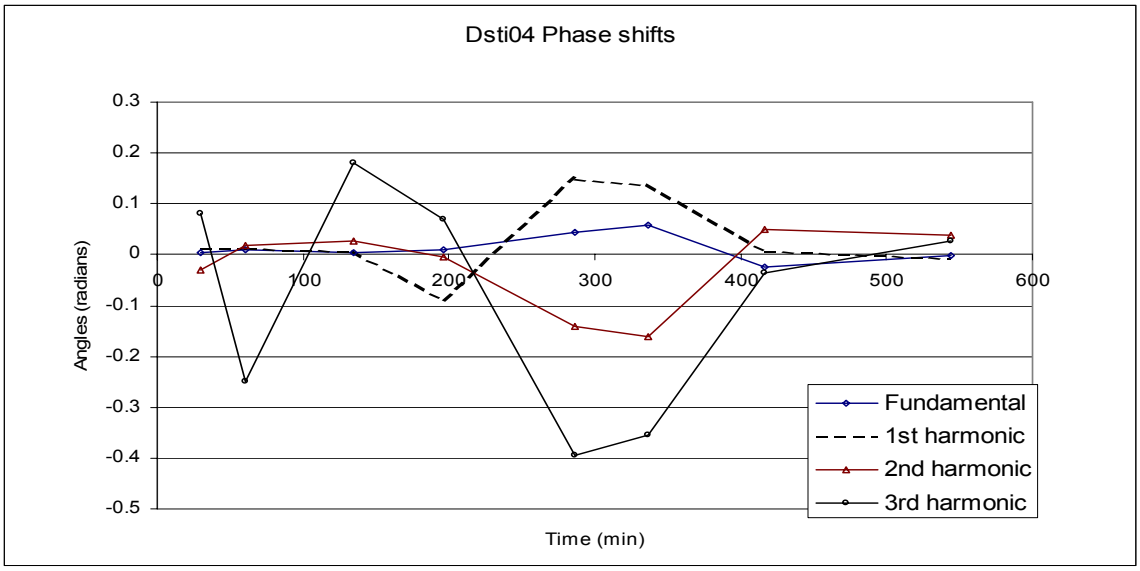

Figure J.5 Phase shift for DSTI04

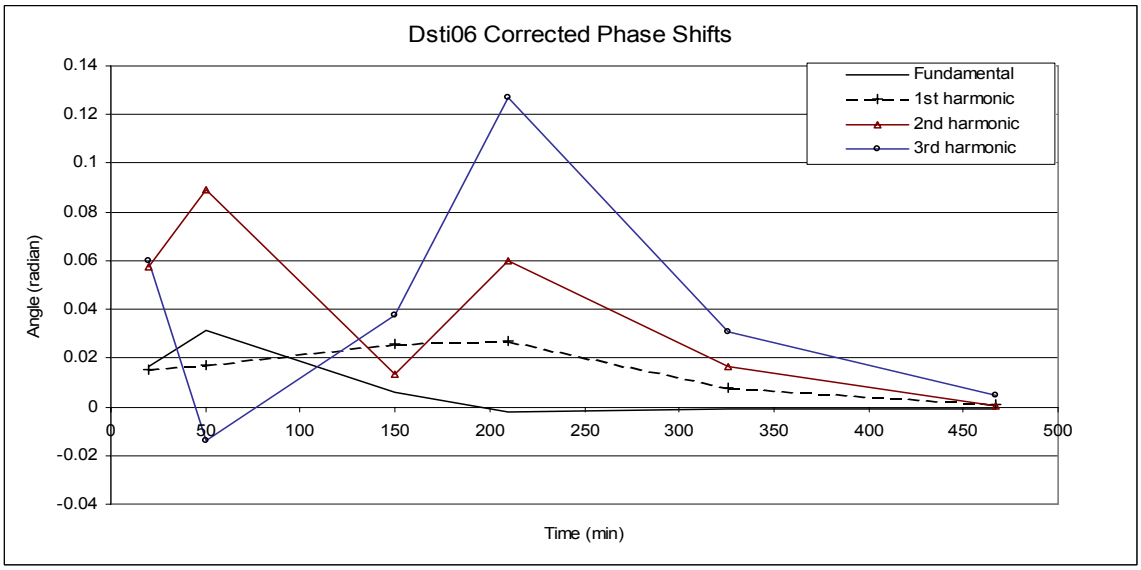

Figure J.6 Phase shift for DSTI06

Appendix K. Reflection Distances

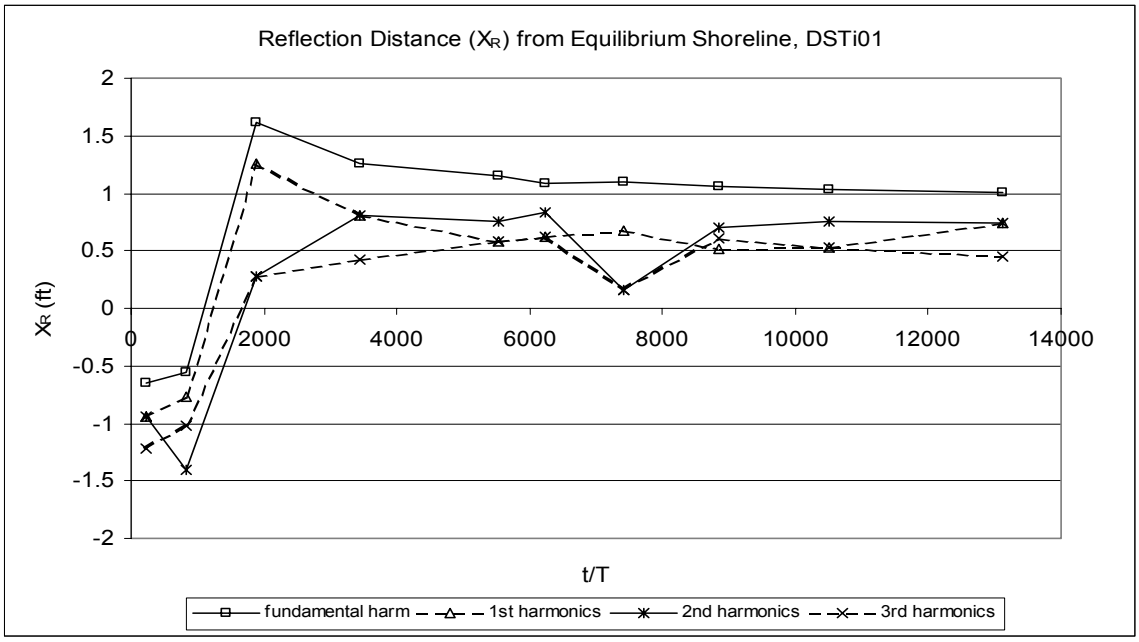

Figure K.1 Reflection distance from equilibrium shoreline for DSTI01

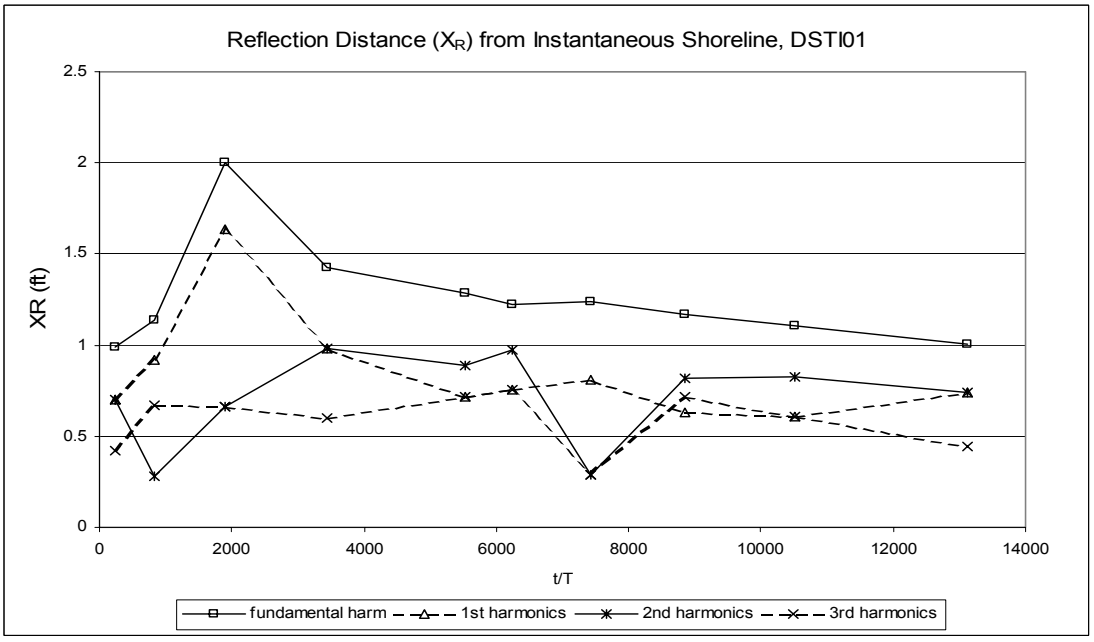

Figure K.2 Reflection distance from instantaneous shoreline for DSTI01

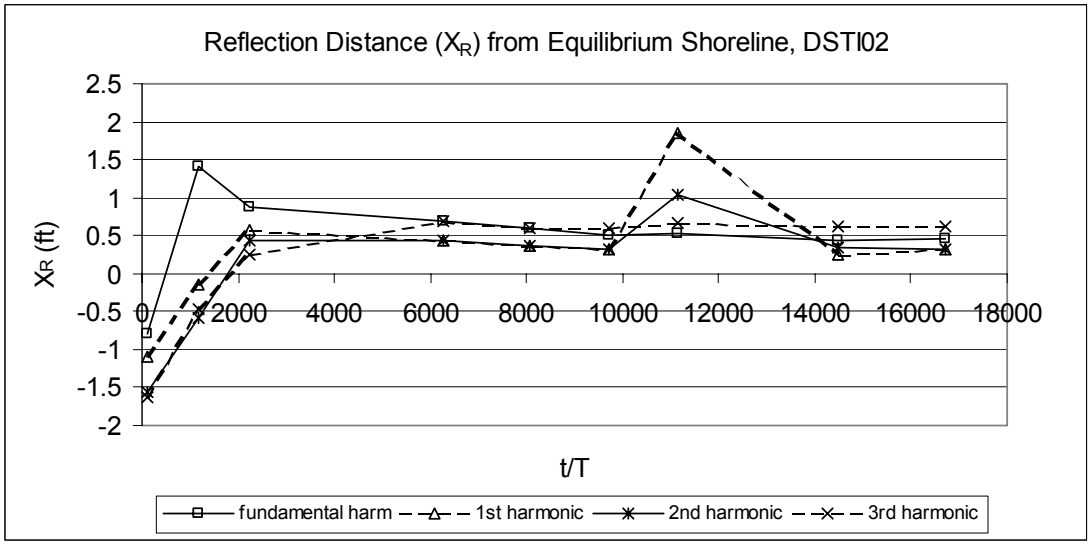

Figure K.3 Reflection distance from equilibrium shoreline for DSTI02

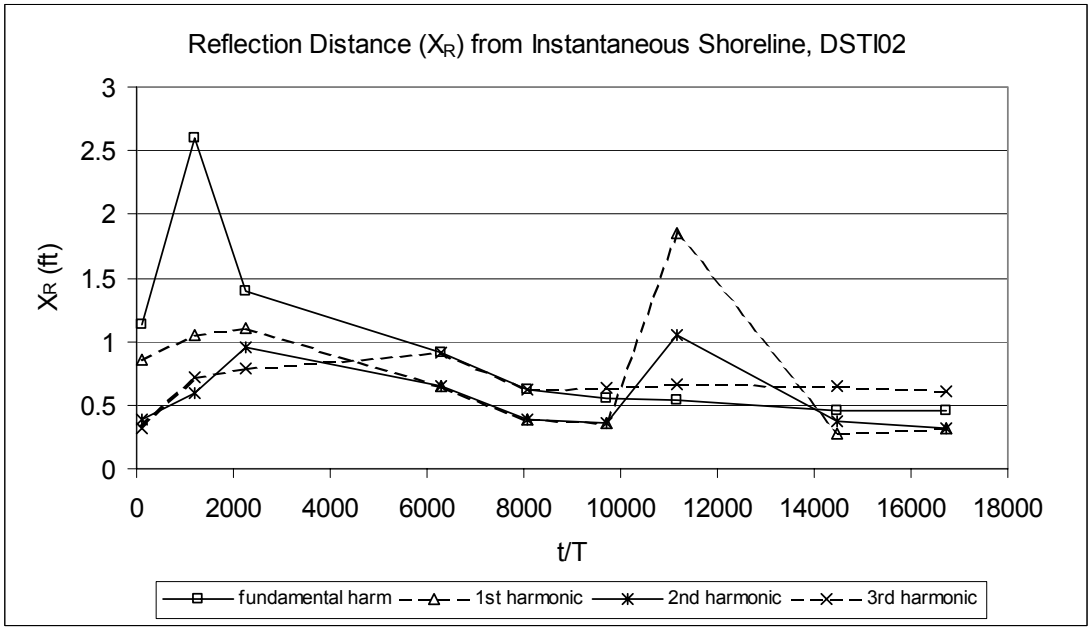

Figure K.4 Reflection distance from instantaneous shoreline for DSTI02

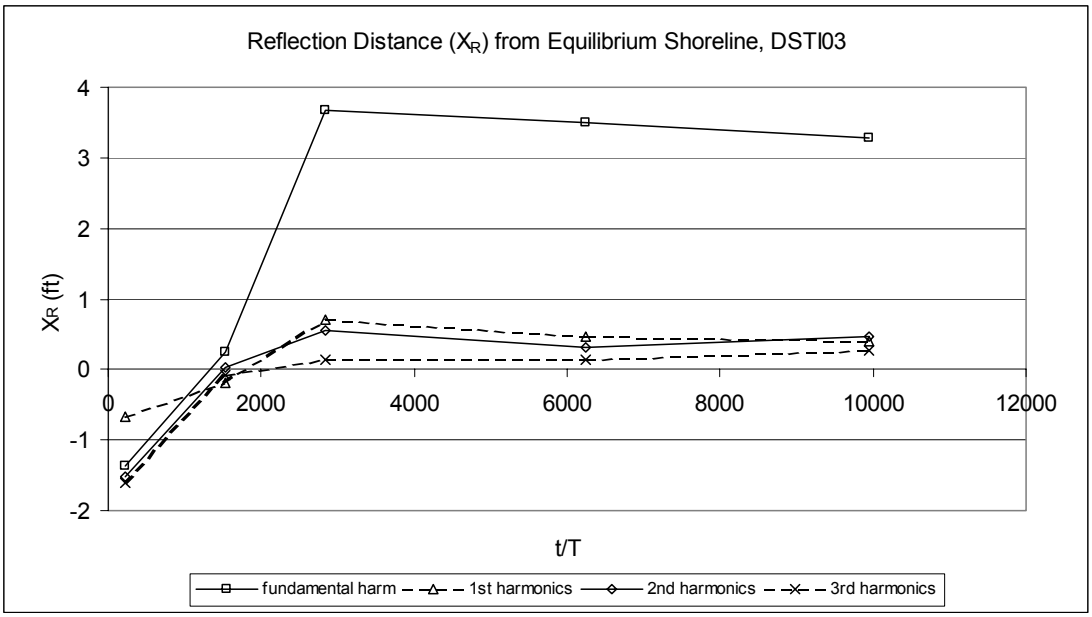

Figure K.5 Reflection distance from equilibrium shoreline for DSTI03

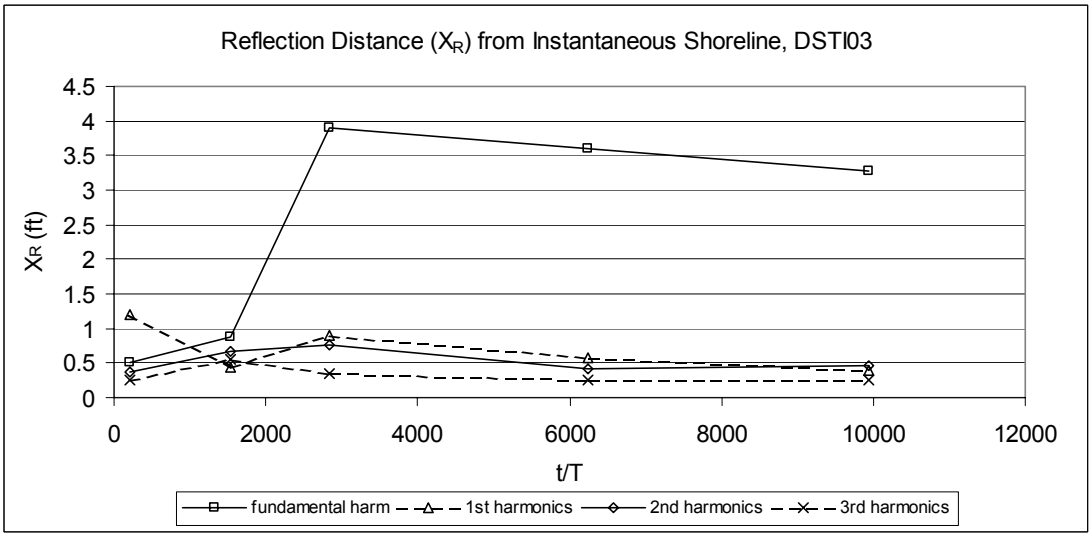

Figure K.6 Reflection distance from instantaneous shoreline for DSTI03

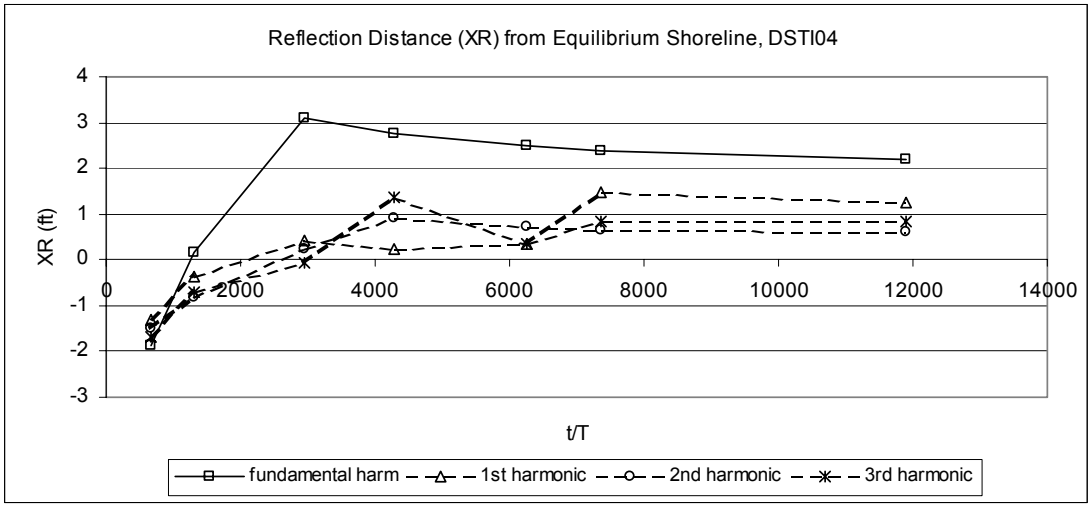

Figure K.7 Reflection distance from equilibrium shoreline for DSTI04

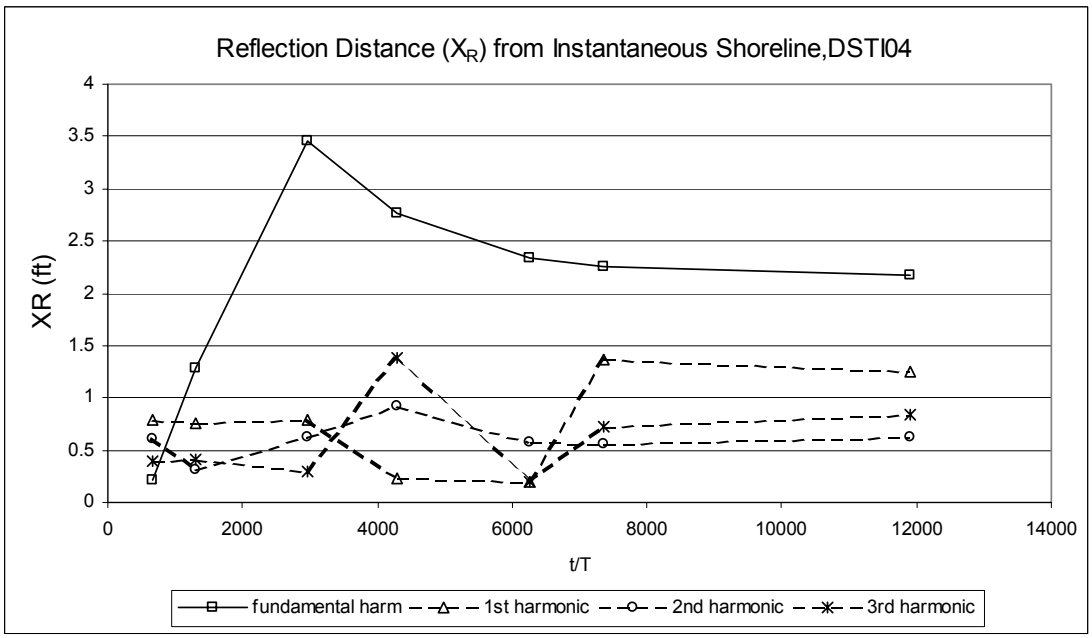

Figure K.8 Reflection distance from instantaneous shoreline for DSTI04

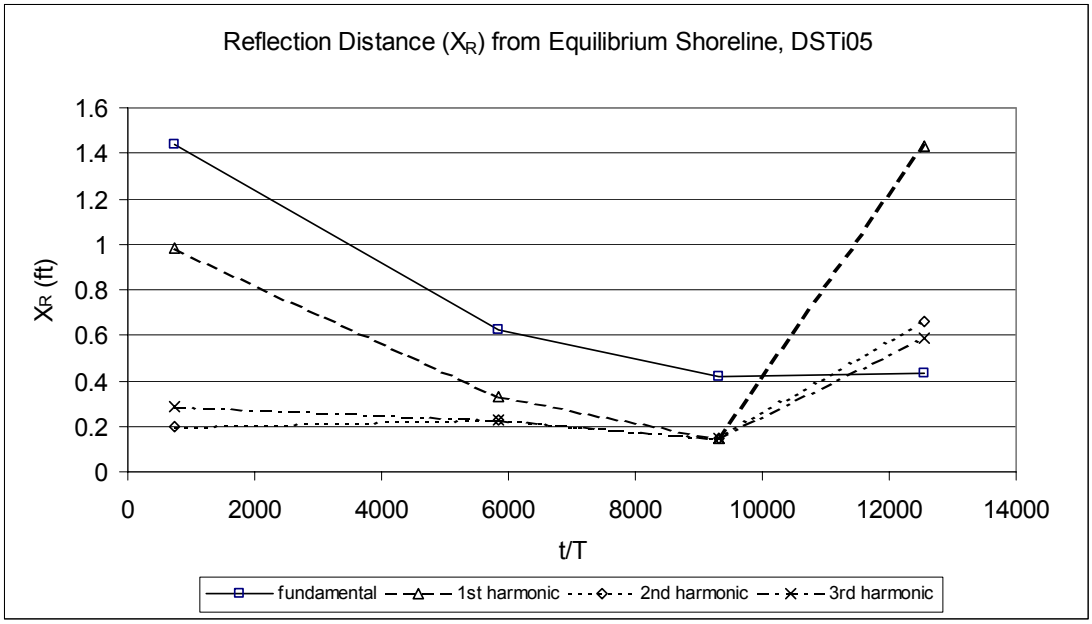

Figure K.9 Reflection distance from equilibrium shoreline for DSTI05

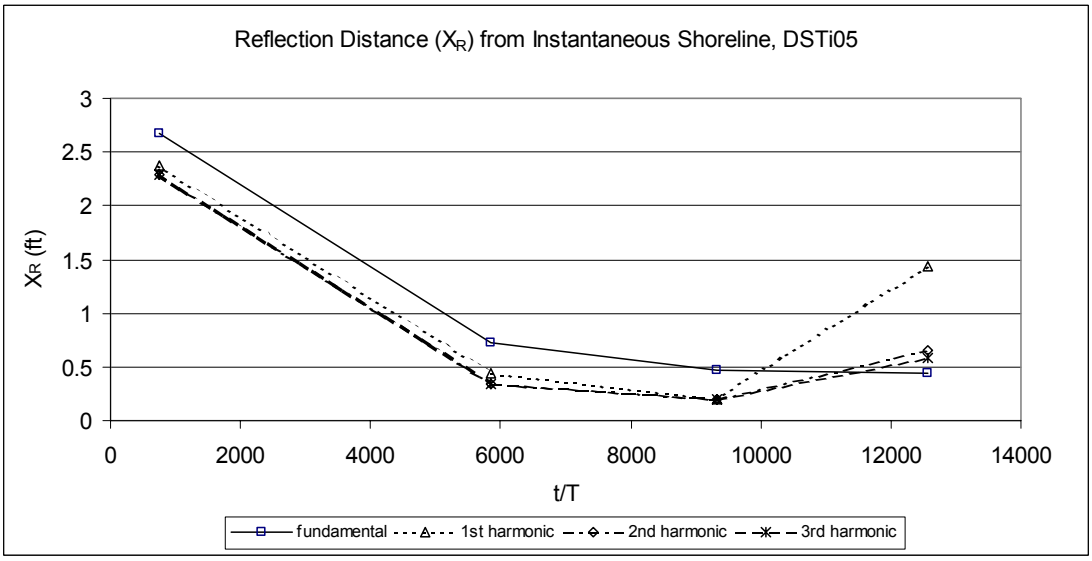

Figure K.10 Reflection distance from instantaneous shoreline for DSTI05

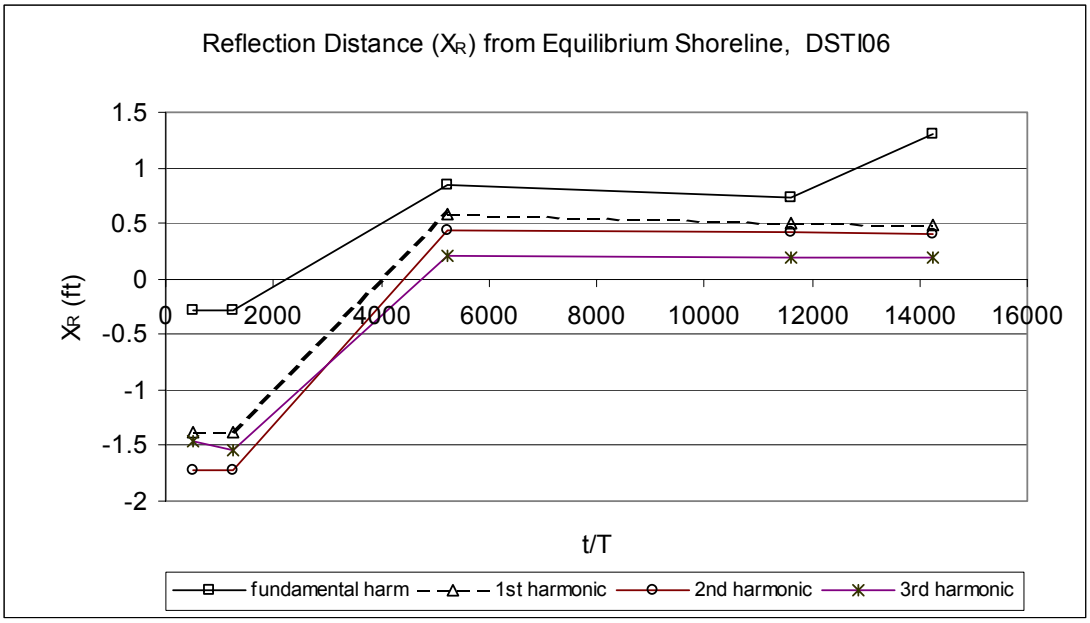

Figure K.11 Reflection distance from equilibrium shoreline for DSTI06

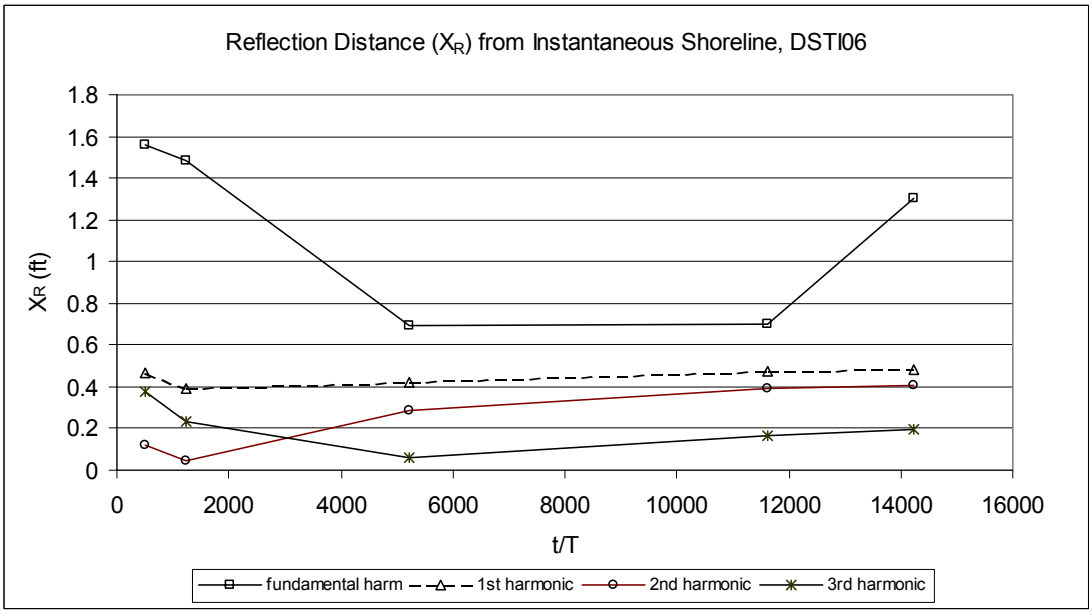

Figure K.12 Reflection distance from instantaneous shoreline for DSTI06

VITA

Mehmet Ali Hinis

EDUCATION

- Ph.D. Civil Engineering (2003), Drexel University.
- M.Sc. Civil Engineering (1997), Drexel University.
- B.Sc. Civil Engineering (1993), Selcuk University.

ACADEMIC EXPERIENCE

- Adjunct Assistant Professor (Summer 2002). Civil and Architectural Engineering Department, Drexel University. Taught Hydraulics.
- Teaching Assistant (1999-2002) Civil and Architectural Engineering Department, Drexel University. Assistant to Hydraulics and Hydrology classes, laboratory instructor for Hydraulics.
- Teaching Assistant (1993-1994) Civil Engineering Department, Nigde University.

HONORS

- Full Scholarship for graduate study in the USA (1995), National Education of Republic of Turkey.

PUBLICATIONS

- "Procedures for calculating dune growth rate" Master thesis. (1997), Drexel University.